HTPEM Fuel Cell Impedance

Mechanistic Modelling and Experimental Characterisation

Vang, Jakob Rabjerg

Publication date:
2014

Document Version
Accepted author manuscript, peer reviewed version

HTPEM fuel cell impedance

- Mechanistic modelling and experimental characterisation

Jakob Rabjerg Vang

Dissertation submitted to the Faculty of Engineering and Science
in partial fulfilment of the requirements for the degree of

Philosophiae Doctor (Ph.D.)

Aalborg University
Department of Energy Technology
Aalborg, Denmark

Thesis submitted:	14th October, 2014
Ph.D. Supervisor:	Professor Søren Knudsen Kær, Aalborg University
Assistant Ph.D. Supervisor:	Associate Professor Søren Juhl Andreasen, Aalborg University
Ph.D. Committee:	Professor Göran Lindberg, Royal Institute of Technology, Sweden Professor Jens Oluf Jensen, Technical University of Denmark Associate Professor Carsten Bojesen, Aalborg University
Ph.D. Series:	Faculty of Engineering and Science, Aalborg University
ISBN:	978-87-92846-47-1

Published by:
Department of Energy Technology
Pontoppidanstræde 101
DK - 9220 Aalborg East

Printed in Denmark by UniPrint, 2015

Title: HTPEM fuel cell impedance - Characterisation and mechanistic modelling

Ph.D. Student: Jakob Rabjerg Vang

Supervisor: Søren Knudsen Kær

Co-supervisor: Søren Juhl Andreasen

Paper 1: Andreasen SJ, Vang JR, Kær SK. High temperature PEM fuel cell performance characterisation with CO and CO2 using electrochemical impedance spectroscopy. Int J Hydrogen Energy. Elsevier Ltd; 2011;36(16):9815–30.

Paper 2: Vang JR, Andreasen SJ, Kær SK. A Transient Fuel Cell Model to Simulate HTPEM Fuel Cell Impedance Spectra. J Fuel Cell Sci Technol. 2012;9(2):021005–1 – 021005–9.

Paper 3: Vang JR, Andreasen SJ, Simon Araya S, Kær SK. Comparative study of the break in process of post doped and sol–gel high temperature proton exchange membrane fuel cells. Int J Hydrogen Energy 2014;39:14959–68.

Poster 1: Vang JR, Mamlouk M, Scott K, Kær SK. Determining HTPEM electrode parameters using a mechanistic impedance model. CARISMA 2012, 2012

This thesis has been submitted for assessment in partial fulfilment of the Ph.D. degree. The thesis is based on the submitted or published scientific papers which are listed above. Parts of the papers are used directly or indirectly in the extended summary of the thesis. As part of the assessment, co-author statements have been made available to the assessment committee and are also available at the Faculty.

Abstract

As part of the process to create a fossil free Denmark by 2050, there is a need for the development of new energy technologies with higher efficiencies than the current technologies. Fuel cells, that can generate electricity at higher efficiencies than conventional combustion engines, can potentially play an important role in the energy system of the future. One of the fuel cell technologies, that receives much attention from the Danish scientific community is high temperature proton exchange membrane (HTPEM) fuel cells based on polybenzimidazole (PBI) with phosphoric acid as proton conductor. This type of fuel cells operate at higher temperature than comparable fuel cell types and they distinguish themselves by high CO tolerance. Platinum based catalysts have their efficiency reduced by CO and the effect is more pronounced at low temperature.

This Ph.D. Thesis investigates this type of fuel cells through experimental studies and mathematical modelling. These studies all revolve around the electrochemical impedance spectroscopy (EIS) characterisation method. EIS is performed by applying a sinusoidal current or voltage signal to the fuel cell and calculating the impedance from the response. This is repeated over the frequency range covering the processes of interest. A representation of the impedance across this frequency range is called an impedance spectrum.

The first experimental investigation treats the effects of adding CO and CO_2 to the hydrogen which is fed to the cell. Since the effects on the steady state performance is well documented, the focus is on the effect on the impedance spectrum. It is concluded that the entire impedance spectrum is affected by even small amounts of CO. This questions parts of the way that HTPEM impedance spectra are often interpreted in the literature.

The second experimental investigation applies EIS to the investigation of the break-in process of two sub-types of HTPEM fuel cells. One type is the Celtec®-P from BASF which utilises a membrane based on the sol-gel process. The other type is the Dapozol® 77 from Danish Power Systems® which is based on a membrane that has been doped with phosphoric acid after casting. The two types show different development of voltage and impedance with time. The sol-gel based cells take the longest to reach a stable development rate. For both types, the results indicate that break-in times for HTPEM fuel cells can be significantly shortened

with respect to the guide lines from BASF.

The main focus of this project is on mechanistic modelling of the interplay of polarisation curves and impedance spectra for HTPEM fuel cells. The aim is to develop a model that can extract information about critical electrode parameters from these two types of measurements. Such a model can potentially be applied to the analysis of degradation phenomena or the effects of different electrode designs. To this end a 1+1D model, taking into account the dynamics of gas transport and electrode kinetics on the cathode side, has been developed. The model takes into account the interplay between the concentration of phosphoric acid in the catalyst layer and the solubility and diffusivity of oxygen, the exchange current density, and the proton conductivity.

Fitting the model to a dataset consisting of polarisation curves and impedance spectra is attempted under different assumptions. These assumptions affect the resulting fitting parameters and the fit quality to varying degree. It is concluded that the requirement of simultaneous fitting of both polarisation curves and impedance spectra makes it much harder to achieve agreement between the model and the data. This can, however be interpreted as a strength, since it makes identification of erroneous assumptions and parameter combinations which can otherwise appear credible if only the polarisation curves are considered.

The ability of the model to reproduce the data outside the fitted area is investigated. Here it is concluded that the effects of the current density is acceptably reproduced but the temperature dependence is problematic. The reason for the unrealistic temperature dependence is assumed to be twofold. In part, the models of the ohmic losses in the fuel cell are too simplistic and, besides, the balance between the diffusion losses in the gas phase and the acid phase is deemed unrealistic. A number of possible improvements to the model to correct these shortcomings are suggested.

In spite of the shortcomings of the model, the results achieved through this project demonstrate the strengths inherent in this modelling philosophy. To the extent it is possible to improve the agreement between the model and the data across operating points, it is deemed feasible for the model to eventually achieve the initial aim.

Dansk Resumé

Som led i processen mod at skabe et fossilfrit Danmark i 2050 er der behov for udvikling af nye energiteknologier med højere virkningsgrader end de nuværende. Brændselsceller, der kan generere elektricitet ved at konvertere brint eller reformerede kulbrinter med højere virkningsgrader end konventionelle forbrændingsmotorer, kan potentielt komme til at spille en vigtig rolle i fremtidens energisystem. En af de brændselscelleteknologier, der får meget opmærksomhed i det danske forskningsmiljø er højtemperaturprotonudvekslingsmembranbrændselsceller (HTPEM-brændselsceller) baseret på polybenzimidazole (PBI) med fosforsyre som protonleder. Denne type brændselsceller opererer ved højere temperaturer end sammenlignelige brændselscelletyper og kendetegnes ved højere tolerance overfor CO. Platinbaserede katalysatorers effektivitet reduceres af CO, og effekten er kraftigere ved lavere temperature.

Denne ph.d.-afhandling behandler denne type brændselsceller gennem eksperimentelle studier og matematisk modellering. Disse undersøgelser har alle karakteriseringsmetoden elektrokemisk impedansspektroskopi (EIS) som omdrejningspunkt. EIS udføres ved at påtrykke brændselscellen et sinusformet spændings- eller strømsignal og beregne impedansen ud fra responsen. Dette gentages over et frekvensområde, som dækker de processer, som man er interesseret i at karakterisere. En repræsentation af impedansen over dette frekvensområde kaldes et impedansspektrum.

Den første eksperimentelle undersøgelse omhandler effekterne af tilsætning af CO og CO_2 til brinten, som tilføres cellen. Da effekten på ydelsen i ligevægtstilstand er velbeskrevet er fokus på effekten på de målte impedansspektre. Det konstateres, at hele impedansspektret påvirkes at tilsætning af selv små mængder CO. Dette sætter spørgsmålstegn ved dele af den måde, som HTPEM-impedansspektre ofte tolkes på i litteraturen.

Anden eksperimentelle undersøgelse anvender EIS til at undersøge indkøringsforløbet for to undertyper af HTPEM-brændselsceller. Den ene type er Celtec®-P fra BASF, der anvender en membran baseret på sol-gel-processen. Den anden type er Dapozol® 77 fra Danish Power Systems®, der baserer sig på en membran, der er tilført fosforsyre efter støbning. De to typer celler udviser forskellig udvikling i spænding og impedans over tid. De sol-gel-baserede celler tager længst tid

om at opnå en stabil udvikling. I begge typers tilfælde tyder resultaterne på, at indkøringstider for HTPEM-brændselsceller kan forkortes væsentligt i forhold til BASFs retningslinjer.

Projektets hovedfokus ligger på mekanistisk modellering af samspillet mellem polariseringskurver og impedansspektre for HTPEM-brændselsceller. Målet er, at udvikle en model, som fra disse to typer målinger kan uddrage information om kritiske elektrodeparametre. En sådan model vil potentielt kunne anvendes til analyse af degraderingsfænomener eller effekter af forskellige elektrodedesigns. Til dette formål er der udviklet en 1+1D-model der tager højde for dynamikken i gastransport og elektrodekinetik på katodesiden. Modellen tager højde for samspillet mellem koncentrationen af forsforsyren i katalysatorlaget og opløselighed og diffusivitet af ilt, hvilestrømmen for de elektrokemiske reaktioner samt protonledningsevnen.

Modellen søges tilpasset et datasæt bestående af polariseringskurver og impedansspektre under forskellige antagelser. Disse antagelser påvirker de resulterende tilpasningsparametre og tilpasningskvaliteten i varierende grad. Det konstateres, at kravet om samtidig tilpasning til både polariseringskurver og impedansspektre gør det betydeligt sværere at få modellen til at passe med data. Dette kan imidlertid udlægges som en styrke, idet det derved bliver nemmere at identificere fejlagtige antagelser og parameterkombinationer, der ellers kan give et troværdigt indtryk, hvis kun polariseringskurverne tages med i betragtningen.

Modellens evne til at gengive data udenfor det tilpassede område afsøges. Her konstateres det, at effekten at strømtætheden kan gengives acceptabelt, men temperaturafhængigheden er problematisk. Årsagen til den uhensigtsmæssige temperaturafhængighed vurderes at være todelt. Dels er modellerne for de ohmske tab for simple, og desuden vurderes det, at balancen mellem diffusionstab i gasfasen og syrefasen ikke er realistisk. Der foreslås en række mulige forbedringer af modellen til at rette op på disse mangler.

Uagtet modellens mangler demonstrerer de resultater, der er opnået gennem dette projekt, de styrker, som ligger i denne modelleringsfilosofi. I det omfang det er muligt at forbedre overensstemmelsen mellem model og data på tværs af arbejdspunkter, anses det for sandsynligt, at modellen kan opnå det indledende målsætning.

Acknowledgement

It seems that I finally got to the end of my Ph.D. studies. Apparently there is light at the end of the tunnel even if the tunnel itself is dark, maze-like, and booby-trapped. I would like to extend my hand in gratitude to a number of people who enabled me to get through in approximately one piece.

First of all, I would like to thank my supervisors, Søren Knudsen Kær and Søren Juhl Andreasen for letting me explore the routes that I found exciting, giving me good feedback, taking their time to listen to my ramblings, and occasionally keeping my perfectionism in check.

Another round of thanks go to Jan Christiansen and the rest of the lab staff for their assistance with my experiments and their patience with the problems my mistakes caused.

I would also like to thank my colleagues at the Department of Energy Technology for many good times. A special thanks to my office mates, present and former, for many talks of both professional and private character. I learned a lot from you guys. A special thank you to Fan for help with the Greenlight set-up and to Samuel and Sobi for their useful last minute corrections for the thesis.

Thanks go to Keith Scott for giving me the opportunity to do my study abroad in his group at Newcastle University. A special thank you to Mohamed Mamlouk for brilliant supervision during my stay. To my flatmates and temporary colleagues in Newcastle, thank you for receiving me so well.

The EUDP programme is gratefully acknowledged for providing funding for this project through the Commercial Breakthrough of Advanced Fuel Cells (COBRA) project.

Thanks also go to the people at Serenergy and Danish Power Systems for supplying the MEAs used in my experiments.

Finally, I would like thank my friends and family for their invaluable support and for always being there to lean on, when I had the sense to do the leaning.

Nomenclature

AEM	Anion Exchange Membrane
APU	Auxiliary Power Unit
ORR	Oxygen Reduction Reaction
CHP	Combined Heat and Power
CPE	Cosntant Phase Element
CV	Cyclic Voltametry
DMFC	Direct Methanol Fuel Cell
EIS	Electrochemical Impedance Spectroscopy
ESA	Electrochemical Surface Area
HF	High Frequency
HTPEM	High Temperature Proton Exchange Membrane
IF	Intemediate Frequency
LF	Low Frequency
LTPEM	Low Temperature Proton Exchange Membrane
MeOH	Methanol
MFC	Mass Flow Controller
PAFC	Phosphoric Acid Fuel Cell
PA	Phosphoric Acid
PBI	Polybenzimidazole
ppm	Parts per million

TPB	Triple Phase Boundary
YSZ	Yttria Stabilised Zirconia

Contents

Chapter 1

Introduction

This chapter introduces the overall aim of the work presented in this project. The different tools employed in the work are briefly described and an outline of the contents of the thesis is given.

1.1 Ph.D. Project objectives

High temperature proton exchange membrane (HTPEM) fuel cells based on phosphoric acid (PA) doped polybenzimidazole (PBI) have been around for almost two decades. Since the discovery by Wainright et al. [1], much work has been done on developing and improving the technology to the present state. This work has been carried out in many different ways by as many different means, but the goal has always been the same. Every piece of research in this field has been carried out to drive the technology towards maturity by improving performance or life time, cutting costs, or increasing the understanding of the processes occurring during operation.

The aim of the work presented in this dissertation is to achieve the latter. The key component in this effort is the electrochemical impedance spectroscopy (EIS) characterisation method. This work presents different studies in which EIS is applied to investigate various aspects of HTPEM fuel cell performance. The main contribution of this dissertation is achieved by combining information from EIS and steady state polarisation curves with mathematical modelling. The aim is to develop a tool, that can be used to estimate parameters, such as the electrochemical surface area and electrode acid content of an HTPEM fuel cell. Determining some of these parameter would otherwise require subjecting the fuel cell to destructive tests in specialised testing equipment. The possibilities for applying this tool are diverse, ranging from investigation of the reasons for observed performance differences between fuel cells of different designs to determining the changes occurring in the fuel cell as a result of degradation.

1.2 Methodology

The methods, which have been applied in order to achieve the aim of the project, are listed in this section.

1.2.1 MEA characterisation

The main part of the experimental work performed during this project is characterisation of single HTPEM fuel cells using EIS and polarisation curves. EIS is performed by subjecting the cell to sinusoidal current or voltage signals at different frequencies and calculating the impedance at each frequency from the relation between the signal and the response. Polarisation curves have been recorded by two methods. Either by slowly ramping up the load from minimum to maximum, or by fixing the current, waiting for the cell to reach steady state, and measuring for some time. The characterisation has been performed using different MEAs subjected to different operating conditions. These include variations in temperature, reactant stream composition, and cell load.

1.2.2 Break-in monitoring

Before the MEAs can be subjected to characterisation, an initial activation or break-in period is necessary. Here the fuel cell is operated at a low current density for a period of time, to condition the MEA. The conditioning serves to increase performance and durability. During the break-in period, the operation is monitored by recording the voltage, and performing EIS sweeps with regular intervals. This is applied to investigate the difference in break-in patterns of different MEA types and to investigate possibilities for improving the break-in method.

1.2.3 Equivalent circuit modelling

In order to better analyse large amounts of EIS data, the impedance spectra can be fitted to simple models of equivalent electrical circuit. The main advantage of this approach is the ability to easily compare the individual spectra by comparing the values of the individual circuit elements. The main drawback of this method is their simplicity. Different models may fit the same data equally well and the physical interpretation of the results can be ambiguous. The results are used for analysing changes happening over time or when changing operating conditions.

1.2.4 Mechanistic modelling

As already mentioned, the main contribution of this work is a fuel cell model, that can be used for extracting MEA parameters from EIS and polarisation data. The model is developed using the finite volume method and implemented using the MATLAB® software package. Emphasis is put on the modelling of the processes

within the cathode catalyst layer, including the characteristics of phosphoric acid. The model is applied to extract MEA parameters from EIS and polarisation data collected as part of the MEA characterisation. A model validation study is performed by comparing the effects of various operating parameters on the model results to the effects seen in the measured data.

1.3 Thesis outline

The contents of this thesis has been divided into the following chapters:

Chapter 1 introduces the aims and means of the Ph.D. project. A brief account of the intended contribution is given, and the methods for achieving those goals are described.

Chapter 2 describes the fundamentals of fuel cells in general and of HTPEM fuel cells in particular including the relevant experimental techniques. An account is given of the state of the art in HTPEM fuel cell research.

Chapter 3 describes the experimental work conducted as part of the project. This includes descriptions of the experimental set-ups and procedures, data analysis using equivalent circuit models, and a brief overview of the published results. The data collected for use with the model is also presented.

Chapter 4 contains an account of the mechanistic modelling performed in this project. The governing equations and sub models of the final version of the model are developed and discussed.

Chapter 5 presents the different fitting cases to which the model is applied. The results of the parameter extraction are presented and discussed. The ability of the model to reproduce data outside the fitting range is evaluated and the shortcomings and necessary improvements of the model are discussed.

Chapter 6 wraps up the main contributions of the work and suggests a path for applying the results in future work.

Chapter 2

Fuel cells

This chapter introduces the fuel cell technology and its place in the energy system of the future. A brief account is given of some of the main fuel cell technologies available. Eventually, the state of the art of the high temperature proton exchange membrane fuel cell technology is described.

2.1 Towards a sustainable future?

With global green house gas emissions continuously increasing, the IPCC now projects a global temperature rise of about 4 °C within this century, assuming business as usual [2]. Meanwhile rising oil prices and demand make oil companies operate in fragile ecosystems already under pressure from climate change. Indeed, humanity seems to be at a crossroads. There is a strong moral obligation for action for those who have the power to act.

In order to limit the global temperature rise to 2 °C, as was pledged by the participants in the COP15 summit in Copenhagen 2009, annual net reductions in global CO_2 emissions are required as early as 2020 [2]. With Denmark aiming for a 40% reduction in CO_2 emissions relative to 1990 by 2020 and a 100% renewable energy sector by 2050, radical changes in all levels of the domestic energy sector will be necessary. The reduction in emissions are supposed to be brought about using a variety of instruments. One prominent contribution is supposed to come from increasing efficiency. Some of this can be achieved by better building insulation, but increasing the efficiency of energy conversion is necessary. Another important factor is the transition to renewable energy technologies with wind power expected to produce 50% of all electricity in 2020 [3]. Such a massive wind power penetration raises new challenges in terms of grid balancing and energy storage to make up for wind power peak production not necessarily coinciding with peak electricity consumption. To accommodate these challenges, changes in the technologies making up the energy conversion infrastructure are

required. The diversity of technologies, which will be employed in the energy system of tomorrow, will undoubtedly be greater than what we see today. Many of the already proven and available technologies can be directly employed in a carbon neutral energy system. Some applications could, however, benefit from technologies which have not yet achieved widespread commercial success. One such candidate is the fuel cell technology.

2.2 An electrochemical solution?

A fuel cell is a device, which converts the chemical energy in a fuel to electrical work through an electrochemical process. In it's most basic form, a fuel cell consists of two electrodes separated by an electrolyte. One electrode (the anode) is fed fuel, and the other (the cathode) is fed an oxidant. This results in a voltage difference between the electrodes. When the electrodes are connected through an external load, the reactants are consumed, and a current flows through the external circuit. At the same time, an equivalent ionic current flows through the electrolyte. This process is sustained as long as reactants are supplied to the fuel cell.

The principle was demonstrated independently by William Robert Grove and Christian Friedrich Schönbein in 1839. Grove called the invention a gas voltaic battery. The principle of his set-up is shown in figure 2.1. He used platinum electrodes inside glass cylinders sealed in one end. The other end was submerged in the dilute sulphuric acid electrolyte. The cylinders were filled with hydrogen and oxygen respectively. When a load was connected to the terminals, a current would flow between the two cylinders, while hydrogen and oxygen was consumed. The reactions happened at the so-called triple phase boundary (TPB), where the electrolyte, the electrode material, and the reactant were all in contact. Grove also demonstrated that the process could be reversed by connecting a series of cells to an electrolyser cell. [4, 5] The electrochemical processes happening in the gas voltaic battery are also illustrated in figure 2.1.

Since it's demonstration by Grove, many different types of fuel cells have been developed. Some types use liquid electrolytes like Grove's cell, but most use some form of solid ionic conductor, since solid electrolytes are more manageable. Platinum is still a popular catalyst material because of it's very high activity even at low temperatures, but due to the high price, alternatives are continuously being sought. Some fuel cell types already employ cheaper catalyst materials, but these materials requires a high operating temperature, which poses other problems in the system.

With the number of fuel cell technologies available today, it would be theoretically possible to introduce fuel cells in all applications, where the conversion of chemical energy to electrical energy is desired. While fuel cells are already competitive in some niche markets, the two major hurdles of price and life time still need to be overcome for mass commercialisation to be realisable.

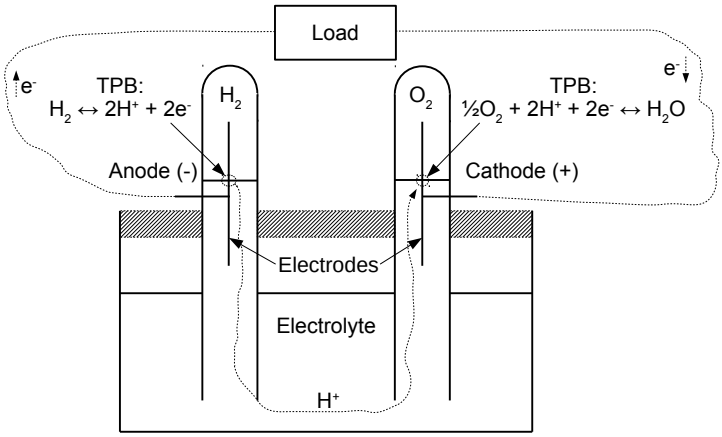

Figure 2.1 – The gas voltaic battery as demonstrated by Grove [4].

2.3 Fuel cell types

Since the first demonstrations, many different types of fuel cells have been developed. Variations between types include electrolyte materials, catalyst materials, operating temperature, feasible fuels, and possible applications. Fuel cell types are generally named after the electrolyte employed. In this section, at brief account of different available fuel cell types, their characteristics, and their applications are given. The fuel cells types are listed in the order of their invention. All sections below contain information from sources [5–7]. An overview of the different types is given in table 2.1.

2.3.1 Molten carbonate fuel cells

The molten carbonate fuel cell (MCFC) was first developed in the 1930's as part of the quest to enable direct conversion of coal to electricity. After the idea of a direct coal fuel cell was abandoned, the MCFC was further developed to use coal gas and other gases as fuel.

Operating at over 600 °C, the MCFC is characterised as a high temperature fuel cell. The electrolyte normally consists of a mixture of alkali carbonates, that are in the liquid state at the operating temperature (hence the name). A matrix of a chemically and electrically inert material is used to immobilise the electrolyte. The electrodes use Nickel based catalysts with metallic Ni for the Anode and NiO for the cathode. The charge carrier in the MCFC is CO_3^{2-}. In order to generate this ion, CO_2 has to be supplied to the cathode. This serves to complicate MCFC systems as most other fuel cells just use atmospheric air. Also, the high operating temperature poses challenges in terms of insulation and gas seals. Other issues

Fuel cell type	Abbreviation	Electrolyte	Catalyst	Operating temperature	Fuel	Poisons	Applications
Low temperature proton exchange membrane	LTPEM	Nafion®	Pt, Pt-Ru	$< 100\,^{\circ}C$	H_2, Reformate	CO, Sulphur	Vehicles, CHP, APU
Direct methanol	DMFC	Nafion®	Pt, Pt-Ru	$< 100\,^{\circ}C$	Methanol	CO	APU
Alkaline	AFC	Liquid KOH, Anion exchange membrane (AEM)	Pt, Ni, Ag	$60 - 220\,^{\circ}C$	H_2	CO_2	Space, Submarine
Phosphoric acid	PAFC	Liquid phosphoric acid (PA)	Pt	$100 - 200\,^{\circ}C$	H_2, Reformate	CO, Sulphur	CHP
High temperature proton exchange membrane	HTPEM	PA doped polybenzimidazole (PBI)	Pt, Pt-Ru	$100 - 200\,^{\circ}C$	H_2, Reformate	CO, Sulphur	CHP, APU
Molten carbonate	MCFC	Liquid alkali carbonates	NiCr NiO	$600 - 700\,^{\circ}C$	H_2, CH_4		CHP
Solid oxide	SOFC	Yttria stabilised zirconia (YSZ)	Perovskites	$700 - 900\,^{\circ}C$	H_2, CH_4, CO	Sulphur	CHP

Table 2.1 – A list of different fuel cell types, their electrolytes, catalysts, temperature range, poisons, and applications. [6–8]

include corrosion problems and relatively high electrolyte loss as well as risk of electrode flooding due to the liquid electrolyte. [9]

The ability to use non-precious metals for catalysts is a great advantage of the MCFC. Another advantage is the ability to use natural gas as a fuel. The natural gas is mixed with water vapour before entering the anode, and the high operating temperature of the MCFC allows for internal reforming via the steam reforming ($CH_4 + H_2O \rightleftharpoons 3H_2 + CO$) and the water-gas shift ($CO + H_2O \rightleftharpoons H_2 + CO_2$) reactions. CO can also be converted electrochemically.

MCFCs are suitable for larger scale stationary power generation. The high operating temperature allows for easy utilisation of the waste heat for heating purposes or in combined cycle systems. Also, MCFCs have been suggested for application in natural gas combined cycle power plants to concentrate CO_2 in the exhaust for easier carbon capture [10].

2.3.2 Solid oxide fuel cells

The solid oxide fuel cell (SOFC) is a high temperature fuel cell made from ceramic materials. As with MCFCs, SOFCs were born from the quest for a direct coal fuel cell.

The electrolyte is generally Yttria stabilised zirconia (YSZ), which conducts O^{2-} ions at high temperatures. The SOFC anode catalyst is usually a mixture of YSZ and Nickel while the cathode catalyst is a ceramic with mixed ionic and electronic conductivity.

SOFCs operate at even higher temperatures than MCFCs which accentuates both challenges and benefits of high temperature operation. For SOFCs differences in thermal expansion between different cell components are a concern, since the ceramic materials are brittle. Compared to MCFCs, SOFC have higher power density and simpler auxiliary systems. The fuel flexibility of SOFCs is similar to that of MCFCs. They are well suited for large scale combined heat and power (CHP) but unlike MCFCs, they can also be used on a smaller scale as auxiliary power units (APUs) [11].

2.3.3 Alkaline fuel cells

As the name suggests, alkaline fuel cells (AFCs) use an alkaline electrolyte (as opposed to acids as used by Grove). The first alkaline fuel cell was developed by Francis T. Bacon in the late 1930's. After WWII, alkaline fuel cells were developed further and were eventually used as power and drinking water supply in space missions.

Alkaline fuel cells generally use liquid KOH as electrolyte. A great advantage of the use of alkaline electrolytes is the ability to use cheap catalysts, such as Nickel at much lower temperatures than for example MCFCs. This is possible because the oxygen reduction reaction (ORR) is much faster in alkaline media than in acidic media.

The main disadvantage of the KOH electrolyte is a tendency to degrade in the presence of CO_2. This means that the reactants supplied to the cell must be pure H_2 and O_2. This makes AFCs unsuited for terrestrial applications. Other issues include a need to replenish the electrolyte periodically and a risk of electrode flooding. Recent development of AFCs have seen the introduction of solid polymer anion exchange membranes (AEM). The solid membranes reduce the problems with electrolyte CO_2 poisoning and remove the problems of the liquid electrolyte but the technology is still early in the development phase [12].

2.3.4 Phosphoric acid fuel cells

The third type of liquid electrolyte fuel cell is the phosphoric acid fuel cell (PAFC). Research into the technology began in the 1960s with the aim of allowing efficient conversion of natural gas to electricity. The strategy was to reform the natural

gas to a hydrogen rich gas mixture before feeding it to the cell. Several systems up to MW scale were demonstrated.

The PAFC uses a concentrated phosphoric acid (PA) electrolyte immobilised in a SiC matrix. The electrodes are made from carbon supported platinum catalyst. Platinum is an excellent catalyst, but it is susceptible to poisoning by CO which is a by-product of the natural gas reforming. The poisoning effects are reduced at high temperature, so PAFCs are generally operated at around 200 °C. High temperature also enhances electrode kinetics. The waste heat from PAFCs is of high quality, making them suitable for CHP applications. The PAFC technology is a relatively mature technology and systems are commercially available. Several plants have proven over 40000 hours of operation [13].

Apart from the risk of CO poisoning, PAFCs also have a problem of the electrolyte absorbing on the catalyst, reducing the activity. This offsets some of the kinetic benefits of higher temperature. As with other liquid electrolyte fuel cells there may be problems with electrode flooding and electrolyte loss.

2.3.5 Proton exchange membrane fuel cells

The proton exchange membrane (PEM) fuel cell (sometimes also called polymer electrolyte membrane fuel cell) is perhaps the most active area of fuel cell research. PEM fuel cells use a solid polymer electrolyte capable of conduction H^+ ions. The first PEM fuel cell was developed in 1960 and based on polystyrene. Five years later a PEM fuel cell served in the Gemini space programme. A significant breakthrough in the development of the PEM fuel cell came about in 1972, when DuPont introduced Nafion®, which was far superior to previous polymer electrolytes. Nafion®is still the electrolyte of choice in most PEM fuel cells.

Nafion® based PEM fuel cells have many appealing properties. Nafion® has high proton conductivity and membranes can be made very thin. Platinum catalysts are also more active in Nafion® than in PA, enabling lower catalyst loading and higher power density than PAFC. Nafion® based PEM fuel cells are also sometimes referred to as low temperature PEM (LTPEM) fuel cells, since they operate between room temperature and 90°C. The low operating temperature enables very rapid start up of the cells, since no preheating is required. LTPEM fuel cells can even be started at subzero temperatures [14]. LTPEM fuel cells are currently the fuel cell technology of choice for the automotive industry.

One serious shortcoming of LTPEM fuel cells is the intolerance to fuel impurities. The standard LTPEM catalyst is Pt supported on carbon. Using this catalyst, CO concentrations as low as 100 ppm will cause severe and partially irreversible degradation of the fuel cell voltage. Alloy catalysts able to operate under 100 ppm CO have been developed [15], but LTPEM fuel cells operating on reformed hydrocarbon fuels still need some kind of CO clean-up if the cell is to operate efficiently.

LTPEM fuel cells are currently available commercially for niche applications

including forklifts [16] and telecom backup applications [17].

2.3.6 Direct methanol fuel cells

An interesting application for Nafion® based PEMs is for use with liquid fuel. The most popular liquid fuel for this application is methanol (MeOH) and the corresponding fuel cell subtype is denoted direct methanol fuel cells (DMFC). The first attempts at developing DMFCs were made in the 1960s, but Nafion↑ was not used as electrolyte before 1992.

DMFCs are fed a mixture of liquid MeOH and water, which reacts at the anode catalyst to form CO_2 and H^+ ions. The main advantages of using MeOH is the much higher energy density compared to hydrogen and the much greater ease in handling liquid fuels compared to gaseous or cryogenic hydrogen. The price of a methanol filling station is orders of magnitude lower than that of a hydrogen filling station [18]. DMFC units can be made very compact and simple with only passive reactant supply. One example of this is currently ongoing research to develop DMFC power supplies to replace batteries for hearing aids [19].

A weakness of the DMFC technology is the tendency of MeOH to permeate through the membrane. When reaching the cathode side, the MeOH combusts catalytically, thereby reducing the efficiency. The greater chemical complexity of MeOH means that the anode kinetics are slower than in a hydrogen fuelled PEM fuel cell. The kinetics are further slowed by the evolution of CO in the MeOH oxidation reaction. To mitigate this effect, Pt-Ru catalysts are used. Even so, the fuel efficiency of DMFCs is lower compared to hydrogen fuelled PEM fuel cells. This limits the applicability of DMFCs to applications where simplicity and system energy density is more important than efficiency.

2.3.7 High temperature PEM fuel cells

In 1995, Wainright et al. [1] introduced phosphoric acid doped polybenzimidazole (PBI) membranes into the PEM fuel cell arena. Fuel cells based on these membranes operate at temperatures above 100 °C. The higher operating temperature compared to Nafion® based PEMs have earned them the name high temperature PEM (HTPEM) fuel cells. This name is also used for PEMs using other membrane materials, operating in the same temperature range. In this work, only PBI based HTPEMs are considered. Chandan et al. [20] published a review including other membrane technologies.

The standard to which the HTPEM fuel cell is usually compared is the LTPEM fuel cell, since the HTPEM is suited for similar applications. There are, however a number of significant differences, which will be outlined below.

Researchers have found HTPEM fuel cells interesting for a number of reasons. Perhaps the most compelling advantage compared to LTPEM is the ability of HTPEM to tolerate moderate amounts of CO in the anode feed. While concen-

trations as low as 100 ppm can cause dramatic performance drops in LTPEMs with non-optimised catalysts, several works demonstrate moderate performance losses of HTPEM fuel cells fed with CO concentrations in the percent range. An example is the work of Modestov et al. [21], where an HTPEM fuel cell using pure Pt-C catalysts lost a mere 19% current density at 0.4 V and 180°C when fed a CO-H_2 mixture containing 17% CO. By comparison, the reduction in current density at 0.6 V is 21% when introducing 100 ppm CO for the best catalyst presented in [15]. Other sources report less impressive results for the CO tolerance of HTPEM fuel cells [22, 23] but in all cases the performance degradation could be minimised by increasing the operating temperature. During prolonged operation, concentrations will have to be significantly lower to avoid permanent degradation. Moçotéguy et al. [24] demonstrated 500 hours of potential cycling operation using hydrogen containing 1% CO with negligible permanent performance degradation.

Another advantageous property of the HTPEM is that the high operating temperature enables easier cooling. This is an advantage in portable and automotive applications, due to the limited space for heat exchangers. The waste waste heat from HTPEM fuel cells is of high quality, which makes HTPEM fuel cells suitable for CHP applications or other processes requiring heat. Since the temperature is above 100 °C, there is no liquid water present in the cell. This eliminates the risk of flooding, which may be an issue for LTPEM. While the presence of water vapour increases the electrolyte conductivity [25], HTPEM fuel cells can be operated using dry feed gasses.

The good CO tolerance and high temperature cooling streams make HTPEMs suitable for use with reformed hydrocarbon fuels. Several papers have investigated the use of methanol in HTPEM fuel cells. Recently, a proof of concept study was made, demonstrating the feasibility of using an HTPEM fuel cell system fuelled with steam reformed methanol as a range extender for a battery electrical vehicle [26]. One group investigated internal reforming of MeOH in HTPEM fuel cells [27–29]. Other studies dealt with control of the reformer from a 350W methanol fuelled HTPEM system [30], used Adaptive Neuro-Fuzzy-Inference-Systems to model the gas composition from the same reformer [31], and investigated the effects of residual methanol in the anode feed [32, 33]. In another study on methanol reformation for HTPEM fuel cells Weng et al. [34] integrated a two step reformer with an HTPEM fuel cell stack. An earlier work byPan et al. [35] investigated a similar concept. Commercial methanol fuelled HTPEM systems are available in the marked [36].

In spite of the promising properties of HTPEM fuel cells, a number of hurdles still have to be overcome before widespread commercialisation is possible. Apart from the ever present issue of cost, HTPEM fuel cells have issues with limited life time. When operating HTPEM fuel cells at constant load, the degradation is usually approximately linear during most of the system life time [37, 38]. When the fuel cell is subjected to load changes, the degradation rate is generally increased [39]. When operating at low current and steady state, life times over 10,000 hours

are possible [38, 40]. When running a fuel cell stack, degradation is affected by gradients in load and temperature within the stack, resulting in earlier failure of some cells [41, 42].

Since PBI based HTPEM fuel cells have PA as the primary proton conductor, they have the issue of reduced kinetics due to PA adsorption in common with the PAFC.

Many different methods have been applied in order to increase the understanding of the workings of HTPEM fuel cells. The work presented in this dissertation focusses on experimental characterisation and, in particular, modelling of single HTPEM fuel cells.

2.4 Modelling and characterisation

As in all other branches of engineering, mathematical models play an important role in fuel cell research. They can be used for gaining insight into the behaviour of the fuel cells in cases where measuring said behaviour is difficult or impossible, they can be used to predict the behaviour of systems in which fuel cells interact with other components, and they can be used to analyse data from operating fuel cells. Sufficiently accurate and detailed model should also be able to predict the effects of different design parameters to limit the number of experimental iterations necessary when developing improved fuel cells.

Models come in all complexities, from one or two equations used for analysing electrode behaviour under idealised conditions to complete, time dependent 3D models of whole fuel cells or even stacks. The following sections are devoted to models of different complexity as well as the characterisation methods needed to verify the model results.

2.4.1 Lumped models

The lumped (or 0D) models describe fuel cell behaviour without need for resolving the cell spatially. The simplicity makes for fast solution times which is useful in system models. Since the parameters are lumped, no information about variations within the fuel cell can be extracted. The primary purpose of a 0D model is usually to reproduce the current and voltage of a fuel cell under different conditions.

An Example of a 0D model was developed by Korsgaard et al. [43]. Here, a single equation describing the relationship between current, stoichiometry, operating temperature and cell potential was developed and fitted to data from a Celtec-P 1000 MEA. The model was expanded with an anode model taking into account the effect of CO and CO_2 in the fuel [44]. Subsequently, the model was applied in a transient micro CHP system model [45, 46].

2.4.2 1D models

Spatially resolving a model gives more predictive qualities in terms of local values of different variables. An example is local reactant concentration within the GDL and CL. 1D models usually resolve the fuel cell through the membrane. This was the case with the model developed by Cheddie and Munroe [47]. The model was used to investigate effects of changing different fuel cell parameters on the steady state performance. Another 1D model by Scott et al. [48] was used to investigate effects of different electrode compositions and catalyst loadings.

2.4.3 2D models

Going to two dimensions enables investigation of more effects compared to 1D models. Some models are termed pseudo-2D, since different parts of the model is resolved in different dimensions. An example is the analytical model by Shamardina et al. [49], which was used to investigate steady state effects of different operating and fuel cell parameters. Here an analytical solutions for the transport of reactants along the channel and through the membrane were developed individually and subsequently combined to calculate the effect on the local current density.

Resolving through the membrane and along the channel enables investigation of the combined effects of local variations in both directions. Sousa et al. [50] developed such a model. The model was used to compare the effects of a variety of operating and fuel cell parameters. Kazdal et al. [51] Developed another steady state model, which was resolved in the same way. Here, the focus was on the effects of water on the degree of phosphoric acid flooding of the catalyst layer.

Models resolved across the channel can be used to investigate the effects of the land on the fuel cell performance. An example of such a model was developed by Hu et al. [52]. The model considered the cathode only. Here electrochemical impedance spectroscopy was used to extract the cell ohmic resistance and exchange current density. Another cross channel model was developed by Sousa et al. [53]. This model was dynamic and included temperature variations in the cell. The model was used to investigate different effects related to heating of the cell as well as long term degradation.

2.4.4 3D models

Resolving the fuel cell in three dimensions is the approach, which can yield the most information about local variations within the cell, but it comes at the cost of greatly increased solution time. Cheddie and Munroe developed two 3D HTPEM models. One assuming gas phase reactions [54] and a second one that took into account effects of reactant solubility and diffusion in the CL membrane phase [55]. Another early 3D HTPEM model assuming gas phase reactions was developed by Peng and Lee [56]. The model was later expanded to take into account transient

variations [57]. Jiao and Li [58] developed a model, which was use to investigate the effects of operating temperature, acid doping level, cell humidification, and stoichiometry. The model was later expanded to take into account the effects of CO poisoning of the anode [59]. A complete 3D model of a sol-gel HTPEM fuel cell including flow field was developed by Siegel et al. [60]. Chippar and Ju [61] developed a 3D HTPEM model that considered the effect of liquid coolant flow on the performance. The model was further developed to include effects of gas cross over [62] and to consider water transport through the membrane [63].

2.4.5 Experimental characterisation

The most direct way to assess the performance of a fuel cell is through experimental characterisation. The experimental techniques can be divided into ex-situ and in-situ techniques, depending on whether the analysis is carried out on an operating fuel cell or not. Wu et al. published a review of different characterisation methods [64, 65]. For this work, the focus is on in-situ characterisation methods, particularly polarisation curves and electrochemical impedance spectroscopy (EIS).

The most common way to characterise a fuel cell is to measure the polarisation curve at different operating conditions. The model by Korsgaard et al. [43] is an example of this approach. The basis of the model is a characterisation of the polarisation performance of a Celtec-P 1000 MEA within the feasible operating range of temperature and stoichiometry. The effects of CO and CO_2 were also included in this characterisation.

Other studies aim at characterising the effects of MEA or cell design parameters as well as of the operating point. Lobato et al. [66] made PA doped PBI membranes, which were characterised by different ex-situ techniques. HTPEM MEAs were made using those membranes, using different catalyst layer designs. The performance of the cells was investigated at different temperatures using polarisation curves.

While polarisation curves give the actual steady state performance of a fuel cell under a set of operating parameters, it can sometimes be hard to distinguish the importance of individual loss mechanisms directly form a polarisation curve. Electrochemical impedance spectroscopy (EIS) is capable of providing more information on the loss mechanisms in a fuel cell by measuring only the voltage and current. Another advantage of this method is that measurements can be performed without changing the operating point of the fuel cell. The method consists of superimposing a sinusoidal signal on the voltage or current and measuring the response. The impedance can then be calculated from the amplitudes and the phase shift. By varying the frequency, the impedance response can be characterised. A more thorough introduction to EIS is given in chapter 3.

Several characterisation studies using mainly EIS have been published. Jespersen et al. [67] investigated the effect of current density, temperature, and stoi-

chiometry on the impedance spectra of a Celtec-P 1000 HTPEM MEA. Mamlouk and Scott [68] used EIS to investigate the effects of various variables on their in-house HTPEM fuel cells. The conclusion drawn from the impedance spectra were validated using polarisation curves. Andreasen et al. [69] measured the impedance of single HTPEM cells and a stack and used single cell data to develop an empirical temperature dependent impedance model for a stack. EIS has also been employed as a tool in the study of HTPEM fuel cell degradation [37, 41, 70, 71] and break-in studies [72, 73].

Another study by Lobato et al. [74] characterised the effects of temperature on the development of HTPEM fuel cell performance over time using both EIS and polarisation curves. The same group studied the effects of the PBI loading in the CL of HTPEM fuel cells, using both polarisation curves and EIS in the analysis [75] .

2.4.6 Impedance models

When fitting models to fuel cell impedance spectra, the models used are typically simple equivalent circuit models [37, 41, 67]. While these models can be useful for quantifying changes to the impedance spectrum as operating parameters are changed or the fuel cell degrades, the mechanistic insights provided by these models are limited by their empirical nature. Some models take physics into account by using simplified linearised versions of the most important transport equations to derive the fuel cell impedance as a function of perturbation frequency. Most of these models concern themselves with LTPEM. To the best of this author's knowledge, the first such model was published by Springer et al. [76] as early as 1996. Another example of an LTPEM impedance model compared the effects of different reaction mechanisms [77]. An analytical model developed by Kulikovsky and Eikerling [78] enabled direct extraction without fitting of the Tafel slope, double layer capacitance and CL conductivity from impedance spectra recorded under conditions where mass transport losses were negligible.

Combined modelling of steady state performance and impedance has only been performed a few times. One such model was a 1+1D model of an LTPEM fuel cell focusing on the gas channel dynamics [79]. The model results were not directly compared to experimental data. Another example is the work by Roy et al. [80], where a steady state and a frequency dependent model was developed to investigate the effects of reaction mechanisms on the low frequency loop in the impedance spectrum. Jaouen and Lindbergh [81] developed an LTPEM cathode model capable of simulating polarisation curves, current interrupt, and impedance spectra. The model was applied to analysis of experimental data [82]. One model concerning HTPEM fuel cells was presented by Boaventura et al. [83]. They constructed a simple 1D dynamic model considering the dynamics of gas transport and double layer charging. The model was capable of fitting the polarisation data quite well, but fell short in matching the time scales in the impedance spectra.

Another study dealt with impedance and steady state behaviour of solid oxide fuel cells [84]. The model used was a dynamic 2D along-the-channel type, which took into account mass transport and heat transfer. The model was validated against button cell data, showing good agreement when heat transfer and momentum was neglected. No validation was performed with respect to full size cells. Simulations using the full model showed significant effects of convection and temperature on the impedance spectrum. Recently, an HTPEM impedance model was developed by Shamardina et al. [85]. Apart from impedance, the model was able to simulate polarisation curves, step changes in potential and current interrupt. The model was capable of extracting electrode parameters to fit a polarisation curve form one impedance spectrum for a cell of around 1 cm^2.

2.5 Contribution of this project

As can be seen from the above, the field of HTPEM research is active and growing. Much work has been carried out within impedance spectroscopy studies and modelling of HTPEM fuel cells. There does, however seem to be a lack of models that are capable of simulating impedance spectra and polarisation curves for practical sized fuel cells. The main goal for this project is to develop a model, which is capable of this. The model should be detailed enough to enable estimation of parameters that would usually require the application of ex-situ experimental methods. Also, the model should have predictive qualities, so fitting to a limited dataset will enable faithful representation of data recorded at other operating points. A model capable of this, would also be capable of assisting in MEA design by predicting the effects of changes in catalyst layer composition. Another possible application could be analysis of degradation phenomena. Finally, the project contains an amount of experimental work. This work is carried out in part to obtain base data for fitting the model and in part to investigate the capabilities of EIS as a stand-alone analytical tool.

Chapter 3

Experimental Work

This chapter deals with the experimental investigations conducted in the course of this project. Initially, an introduction to the impedance spectroscopy method is given. Subsequently, the experimental set-ups used are introduced. An account is given of the equivalent circuit models applied and their applicability and shortcomings are discussed. A brief account is given of the conclusions of the two papers published on the experimental work. Eventually, the experimental data collected for use with the mechanistic impedance model is presented.

3.1 Electrochemical impedance spectroscopy

Electrochemical impedance spectroscopy is an in-situ characterisation method for electrochemical systems. The method is used to gain information about the time scales and individual importance of different processes in the system. For fuel cells, measurements are carried out by running the cell at steady state and superimposing a sinusoidal signal onto the current or the voltage. A phase shifted voltage or current response of the same frequency will be generated by the cell. The amplitudes (ΔV [V] and Δi $\left[\mathrm{A\,cm^{-2}}\right]$) and the difference in phase (φ) are used to calculate the impedance (Z $\left[\Omega\,\mathrm{cm^2}\right]$) as:

$$Z = \frac{\Delta V}{\Delta i}\left(\cos\varphi + j\sin\varphi\right) \tag{3.1}$$

By performing this operation on a range of frequencies, the impedance spectrum is recorded. The spectrum is usually visualised using a Nyquist plot, but Bode plots or plots of the real and imaginary parts of the impedance versus the logarithm of frequency can also be used.

When plotting the impedance spectra, a number of different features can be seen. Not all features are visible in all spectra. There can be significant differences between spectra for different MEAs. Figure 3.1 shows impedance spectra for two

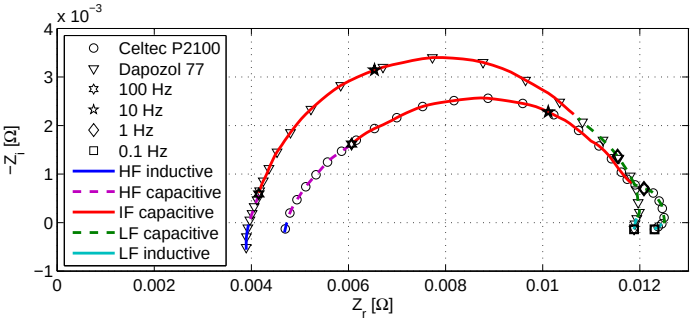

Figure 3.1 – Nyquist plot of impedance spectra for two different MEAs. Coloured parts denote different contributions. Taken from paper 3.

of the MEAs tested in paper 3. The different features in the spectra have been coloured to better enable distinction. As can be seen, some of the smaller features are more or less masked by the more prominent ones, so the colouring is more of a rough guide than a strict instruction in how to divide the spectrum. The HTPEM impedance spectrum usually exhibits a maximum of six distinguishable contributions. These consist of three capacitive loops, two inductive loops and one pure ohmic contribution. The following discussion of the individual contributions is a rewritten version to the one given in paper 3.

The ohmic contribution is responsible for the offset between the imaginary axis and the point where the high frequency part of the spectrum and the real axis intersect. The ohmic contribution is related to resistive losses in the fuel cell. The most prominent is the resistance to proton transport in the membrane, but contact resistances between the individual cell components can also be significant.

The inductive and capacitive contributions are denoted by the relative frequency at which they appear in the spectrum. The capacitive contributions are denoted as high frequency (HF), intermediate frequency (IF), and low frequency (LF) respectively. The HF contribution is highlighted in purple. It is visible above 100 Hz towards the left of both spectra. This contribution is more pronounced in the Celtec®-P2100 MEA. This loop is either a 45° slope attributed to the effects of limited catalyst layer conductivity [76, 86] or a semicircle related to anode activation [7, 69, 87]. Some sources either do not observe this contribution [70] or neglect it when modelling [67]. The intermediate frequency contribution (red) is the most prominent loop in the Nyquist plot, primarily associated with cathode activation. The top point of the resulting loop is located slightly above 10 Hz in the spectrum of the Celtec®-P2100 MEA and slightly below 10 Hz in the Dapozol® 77 MEA spectrum. The low frequency capacitive loop becomes visible just above 1 Hz. In the spectrum of the Dapozol® MEA, the low frequency capacitive loop and the intermediate frequency loop overlap, so distinction becomes

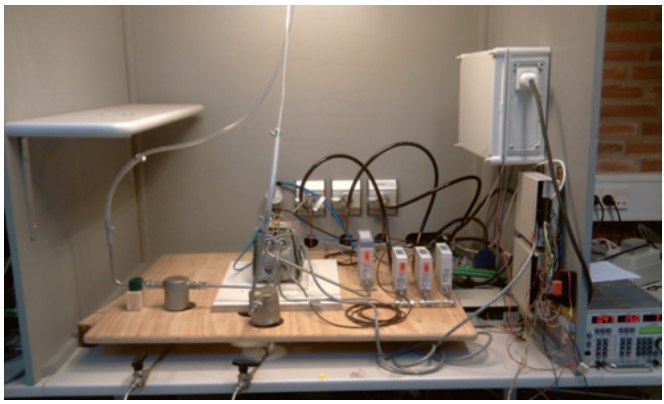

Figure 3.2 – Photo of the in-house single cell test bench.

difficult. This contribution is related to some kind of mass transport limitation. The exact nature of this limitation is debated. Some sources attribute it to diffusion in the gas diffusion layer and the catalyst layer [68, 76], while others claim it to be a result of gas channel dynamics [79, 88–90]. The latter interpretation is backed by the modelling study performed in this work. See section 5.4.

The inductive contributions are visible in either end of the Nyquist plot, where the spectrum crosses below the real axis. The high frequency inductive contribution is located in the left-most part of the spectrum. This contribution pulls the intersection of the spectrum with the real axis slightly to the right. This contribution can be attributed to the inductance of wires and other components in the fuel cell [70]. The low frequency inductive loop is visible around 0.1 Hz. It can be attributed to the formation of intermediates in the electrode reactions and/or platinum oxidation [77, 80, 91].

3.2 Experimental set-ups

For the experimental work conducted during this project, two different experimental set-ups have been used. One set-up is an in-house developed single cell test bench, which has been refined during this project. The other is a commercial Greenlight Innovation G60 test bench. The set-ups are described briefly in this section.

3.2.1 In-house test bench

The in-house developed system is depicted in figure 3.2. This set-up is the one used for the measurements in papers 1, 2, and 3. The set-up employs an electrically heated single cell assembly with serpentine flow fields. Reactants are supplied

to the cell using mass flow controllers (MFCs). The cathode is supplied using a Bürkert 8712 air MFC. The anode can be supplied with either pure hydrogen or a mixture of H_2, CO, and CO_2, using three Bürkert 8711 MFCs. Current is drawn from the fuel cell using a TDI RBL488 50-150-800 electronic load module. The temperature is measured using two type T thermocouples inserted into groves in the anode flow plate.

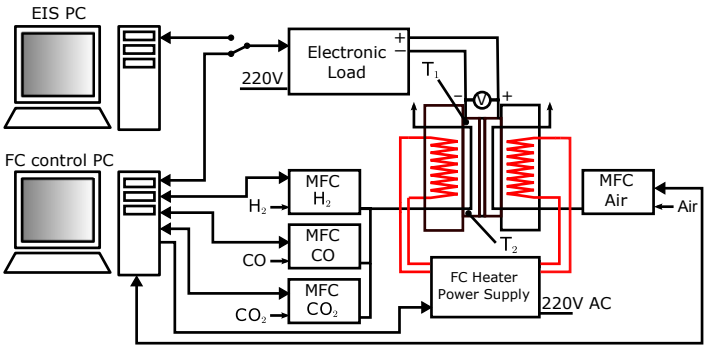

Figure 3.3 – Schematic representation of the in-house single cell test bench.

The set-up is controlled using two LabVIEW real-time PCs. The PC labelled "FC control PC" is used to control the set-point of the system and to record the monitored system variables. The load and the MFCs have internal controllers, but the temperature is controlled by adjusting the duty cycle of the heaters using a PI controller inside the LabVIEW code. The program can also be set to record polarisation curves. The control programme enables automated execution of a series of measurements consisting of impedance spectra and polarisation curves at different operating conditions. The PC labelled "EIS PC" only performs impedance spectroscopy measurements. When instructed by the control programme to perform EIS, control of the load module is transferred to the EIS PC and the frequency sweep is performed. The EIS PC performs all the necessary signal processing and prints the recorded impedance spectrum to a file. Detail of the equipment used is given in table 3.1.

The in-house impedance system has been compared to the performance of a commercial Gamry FC350^{TM} Fuel Cell Monitor. A comparison of BASF Celtec®-P2100 MEA impedance spectra recorded using the two systems is shown in figure 3.4. As can be seen, the agreement is quite good at intermediate-low frequency even if the data points are more scattered when using the in-house system. The disagreement at high frequencies seems to stem from difference in the inductive contribution. The in-house system does not correct for the inductance of the measuring wires. This is considered a minor concern, since the additional inductive contribution can be accounted for, when fitting the spectra to equivalent circuit models.

Equipment	Model	Range	Accuracy	Bias error
Air MFC	Bürkert 8712	0.04 - 2 $\frac{l_N}{min}$	±0.8%	±0.3%
H_2 MFC	Bürkert 8711	0.02 - 1 $\frac{l_N}{min}$	±0.8%	±0.3%
Load	RBL488 50-150-800	0 - 150 A	±0.25%	±0.1%
Thermocouples	AMETEK 1500 MT4 - Type T	-40 - 400°C	±0.4%	±0.125%
FC ctrl PC AI	NI 6229	0 - 10 V	±0.015%	±0.015%
FC ctrl PC AO	NI 6704	0 - 10 V	± > 0.01%	±0.007%
EIS PC AI	NI 6229	0 - 10 V	±0.015%	±0.015%
EIS PC AO	NI 6229	0 - 10 V	±0.015%	±0.017%

Table 3.1 – Overview of the equipment used in the in-house test bench and the associated uncertainty. Accuracy refers to the measured/specified value. Bias errors refer to full scale values.

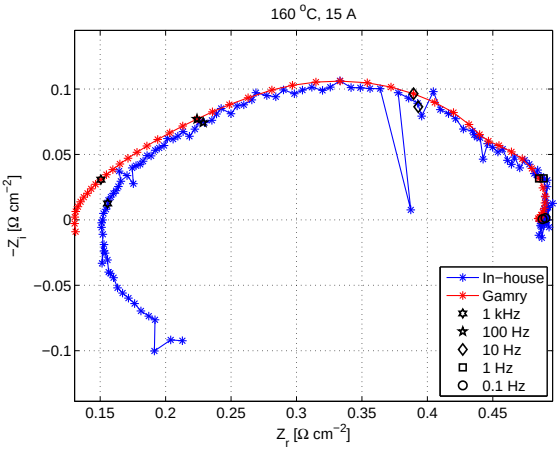

Figure 3.4 – Comparison between impedance spectra recorded using a Gamry FC350^{TM} Fuel Cell Monitor and the in-house developed LabVIEW based impedance system.

3.2.2 Greenlight Innovation G60 test bench

The G60 test bench from Greenlight Innovation has been used to perform the measurements to support the modelling studies presented in chapter 5. A schematic drawing of the test bench is shown in figure 3.5. The G60 test bench is more advanced than the in-house version. In addition to H_2, CO_2, and CO, the

anode can be supplied with CH_4 and methanol to better simulate reformate gas operation. The cathode is supplied with air. Both electrodes can be purged using N_2. The gas pipes are fitted with temperature controlled humidifiers and heating elements for reactant preheating. The fuel cell load is controlled using a TDI load module. A Gamry Reference 3000^{TM} impedance analyser can be connected to the set-up to record impedance spectra. The operation of the cell as well as the measurement sequence are controlled using a build-in PC.

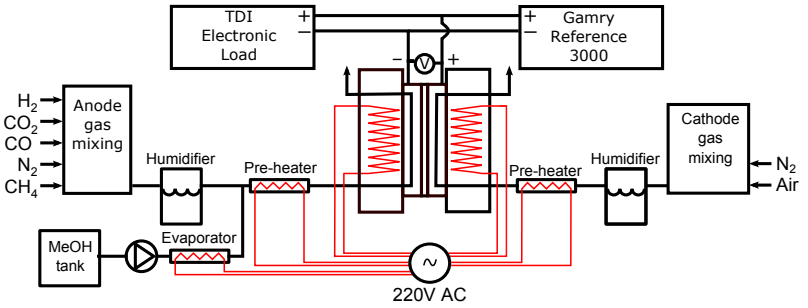

Figure 3.5 – Schematic representation of the G60 single cell test bench.

3.2.3 Fuel cell assembly

The single cell assemblies used in the two test benches are very similar. The components of a single cell assembly are shown in figure 3.6. All components except the MEA come in mirrored pairs. The steel end plate (A) is used to clamp the assembly together, serves as a manifold for the reactant gas, and has slots for the cylindrical electric heating elements. The material on the surface of the end plate is a dielectric to prevent the cell from short-circuiting. The current collector plate (B) is used for connecting the wires from the load and the wires for measuring the voltage. The conduction enhancer (C) is made from soft carbon and serves to reduce the conduction resistance. The cell used with the G60 test bench lacks conduction enhancers. D is the flow plate. The one shown is for the cathode with three serpentine flow channels. The anode flow plate has two channels. The flow plates differ between the test benches. The in-house test bench has cathode flow channels of 2 mm depth, while the depth is 1 mm for the G60. The anode flow channels are 1 mm deep in both cases. The channel width is 1.2 mm for both anode and cathode. PTFE gaskets (E) are employed in order to keep the assembly gas tight. The thickness of the gaskets depends on the MEA tested. The choice is a compromise between several factors. If the gaskets are too thick, contact resistance will be high. If the gasket is too thin, the mass transport limitation may be high due to excessive compression, or the assembly may not be gas tight. No systematic study has been made in this regard. Gaskets are

400 µm when using Celtec®-P MEAs and 250 µm when using Dapozol® MEAs. The MEA (F) is supplied by our partners.

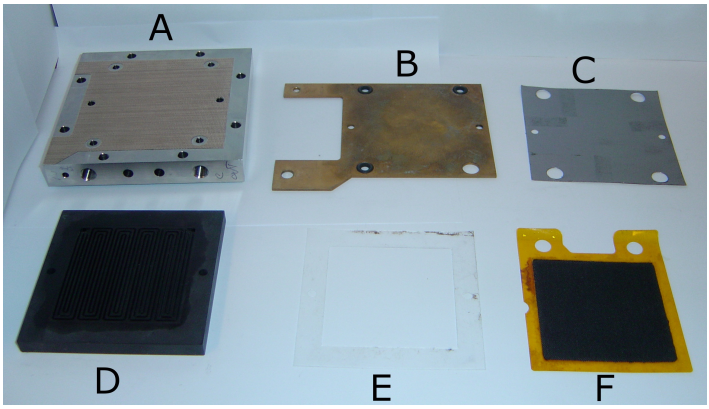

Figure 3.6 – Components of the single cell assembly. A: End plate, B: Current collector, C: Conduction enhancer, D: End plate, E: PTFE gasket, F: MEA.

3.3 Equivalent circuit modelling

Equivalent circuit models are widely used in the analysis of fuel cell impedance spectra. The philosophy is to represent the fuel cell dynamics using a number of ideal electrical components, such as resistors, capacitors, and inductors. This type of model is convenient in many ways, since it allows relatively quick fitting to large amounts of data. This facilitates comparison of individual parts of the impedance spectrum at different operating points, which can otherwise be hard using only the impedance data. Even though the models can be a powerful tool, they have shortcomings. Different equivalent circuit models may fit the same impedance spectrum equally well. Also, the link between the fitted resistances and the actual loss mechanisms in the fuel cell is ambiguous. In papers 1 and 3 equivalent circuit models have been used to quantify the effects of fuel composition (paper 1) and break-in time (paper 3).

3.3.1 Circuit elements

The equivalent circuit models are constructed by combining circuit elements of different types in series and parallel. The types used in this work are resistors, capacitors, inductors, constant phase elements (CPEs), and bounded Warburg impedances. The formulation used for the CPE and the bounded Warburg are given in (3.2) and (3.3). Here $\omega \left[s^{-1}\right]$ is the radial frequency. For the CPE, ϕ is the CPE exponent and $Q \left[\mathrm{S\,s^{\phi}\,cm^{-2}}\right]$ is the pseudo-capacitance. ϕ can be

any value between -1 (pure inductor) and 1 (pure capacitor). In this study the CPE is used as a capacitive element only. In the bounded Warburg formulation, R_{W} $\left[\Omega\,\mathrm{cm}^2\right]$ is the Warburg coefficient and T_{W} $\left[s^{-\frac{1}{2}}\right]$ is the diffusion parameter.

$$Z_{\mathrm{CPE}} = \frac{1}{Q(j\omega)^{\phi}} \tag{3.2}$$

$$Z_{\mathrm{W}} = R_{\mathrm{W}} \frac{\tanh\left(T_{\mathrm{W}}(j\omega)^{\frac{1}{2}}\right)}{T_{\mathrm{W}}(j\omega)^{\frac{1}{2}}} \tag{3.3}$$

3.3.2 Models

Basic fuel cell impedance models usually include a resistor in series with one or more parallel resistor-capacitor pairs. When modelling practical size fuel cells, the models have to be adjusted to capture the behaviour observed.

The model used in paper 1 is presented in figure 3.7. The first part of the model consists of an ohmic resistance to reproduce the resistive losses in the cell. The next part is a parallel inductor-resistor pair, which accounts for the high frequency inductive contribution. This feature is prominent in the measurements made using the in-house set-up. The model then considers a high frequency capacitive contribution in the form of a resistor in parallel with a CPE. The CPE exponent is set to $\phi = 0.85$. Another similar circuit represents the intermediate frequency loop of the spectrum. The low frequency capacitive contribution is modelled as a resistor in parallel with a pure capacitor. When fitting the model to the impedance data at various operating points, the fitted resistances yielded clear trends to aid the interpretation of the spectra.

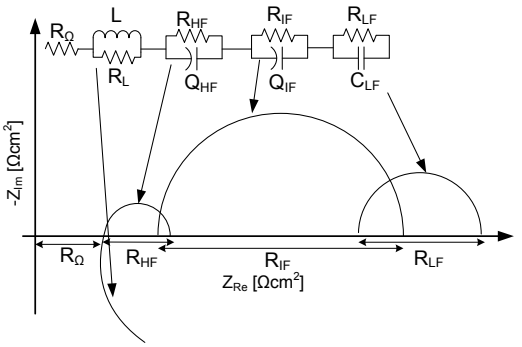

Figure 3.7 – Illustration of the equivalent circuit model used in paper 1 and a schematic representation of the resulting simulated impedance spectrum.

In paper 3, three different equivalent circuit models were compared in order to determine which to use for the analysis of the impedance spectra recorded dur-

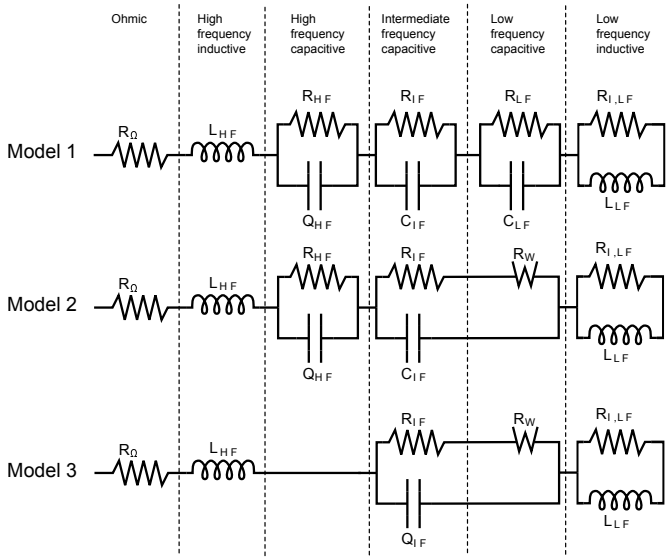

Figure 3.8 – Illustration of the equivalent circuit models used in paper 3.

ing break-in of three post-doped Dapozol® 77 MEAs and three sol-gel Celtec®-P MEAs. The circuits are shown in figure 3.8. The models differ from the previous example in a number of ways. The high frequency inductive contribution is modelled only as an inductor. The high frequency loop is represented using a CPE with $\phi = 0.5$. This was intended to reproduce the 45° slope at high frequency. Model 3 does not include a high frequency loop. The intermediate frequency loop is represented using ideal capacitors in models 1 and 2. Model 3 used a CPE with $\phi = 0.8$. The low frequency loop is represented using another ideal parallel R-C circuit in model 1. Models 2 and 3 used bounded Warburg elements connected with the intermediate frequency contribution to form a modified Randles circuit [92]. The models all take into account the low frequency inductive contribution. This is modelled using a parallel R-L circuit.

A comparison of the impedance spectra of the fitted models are shown in figure 3.9. Models 1 and 2 show practically identical results. Model 3 deviates somewhat from the others due to the lack of the high frequency loop. Mostly, the deviation is within the variation exhibited by the data points. In paper 3, model 3 was chosen for the analysis, since it produced more consistent values when fitting to the impedance spectra recorded during break-in of the MEAs.

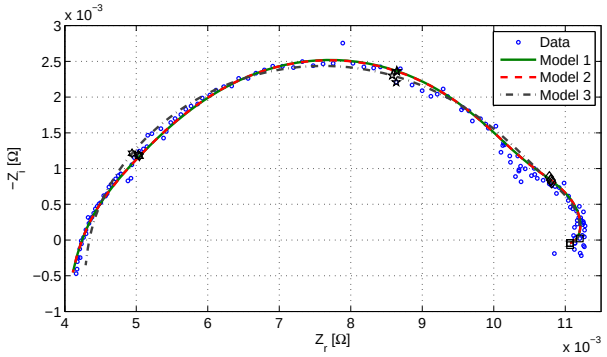

Figure 3.9 – Comparison of the fits of the equivalent circuit models used in paper 3. The black symbols denote decade frequencies. The leftmost group is 100 Hz, the rightmost is 0.1 Hz.

3.3.3 An afterthought on suitable E-C models

The differences between the models of papers 1 and 3 and the fact that they are all capable of fitting recorded impedance spectra with reasonable accuracy, illustrates one of the problems with equivalent circuit models. The importance of the individual circuit elements depends very much on the design of the circuit and does not necessarily reflect the processes that they are supposed to represent. This is also the case in the models used in papers 1 and 3.

The use of a parallel R-CPE circuit to represent the high frequency part might not be a good idea unless there is a clearly visible capacitive loop. In the absence of a high frequency inductive part, the 45° slope is not well represented in this way. The attempt to get the slope by using a CPE with $\phi = 0.5$, resulted in the high frequency resistance being larger than the one at intermediate frequency. This is not realistic if there is a high frequency loop related to the anode kinetics. A compromise could be to use a bounded Warburg element for the intermediate frequency loop. This would give the 45°high frequency slope while also providing a capacitive loop for the intermediate frequency range. The bounded Warburg is derived for diffusion limited processes, but as is shown in section 5.4, there is at least some reactant transport contribution to the intermediate frequency loop. The low frequency capacitive loop can be modelled using a simple R-C or R-CPE circuit. It might also be worthwhile to abstain from modelling the low frequency inductive contribution. The low frequency part of the spectrum is very prone to variations in for example the cell temperature. Since the low frequency inductive loop is small, compared to the degree of random noise in this region, the inclusion of this in the model may cause more uncertainty than clarity.

3.4 MEA characterisation

The main characterisation work carried out in connection with this project was published in paper 1. This section presents a brief overview of this work.

3.4.1 Methods

The aim of the work is to investigate the effects of CO and CO_2 on the steady state and impedance response of an HTPEM fuel cell using a 45 cm^2 Celtec®-P2100 MEA. The MEA is tested using the in-house test bench described in section 3.2. The cell is subjected to different temperatures and fuel compositions. One polarisation curve is recorded at each combination of temperature and gas composition. EIS is conducted at different currents as well. The operating parameters are given in table 3.2. The values for stoichiometry quoted in the table differs from those in the paper due to an error when converting the desired stoichiometry to volume flow rate in the LabVIEW control programme. This error was only discovered after publication of the paper but should not affect the conclusions.

Parameter		Values								
CO content [%]		0			25					
CO_2content [%]		0.15			0.25		0.5		1	
EIS current [A]		5			10		15			
Stoichiometry	Air	4.4								
	H_2	1.3 (3.3 when using CO)								
Temperature [°C]	Pure H_2	100	110	120	130	140	150	160	170	180
	With CO					140		160		180

Table 3.2 – Operating parameters for Celtec®-P2100 characterisation. The hydrogen stoichiometry is increased when using CO due to limitations in the turn down ratio of the CO mass flow controller.

3.4.2 Contribution

The results obtained using pure hydrogen were generally in agreement with the literature. The trends were generally decreasing resistances with increasing temperature and current. This follows intuitively from the reduced slope of the polarisation curve at higher currents and temperatures and has also been demonstrated by several other sources [67, 68]. The low frequency resistance did, however, behave unexpectedly at low currents. Figure 3.10 shows that the low frequency resistance is highest at 5 A. This is counter-intuitive, since mass transfer limitations are smallest at low current. Also, Chen and Lai [87] demonstrated a monotonically decreasing low frequency resistance with increasing current, using

a model similar to the one used here. At any rate, the phenomenon is probably model related, since the low and intermediate frequency loops overlap more at low current, making it harder to distinguish the contributions.

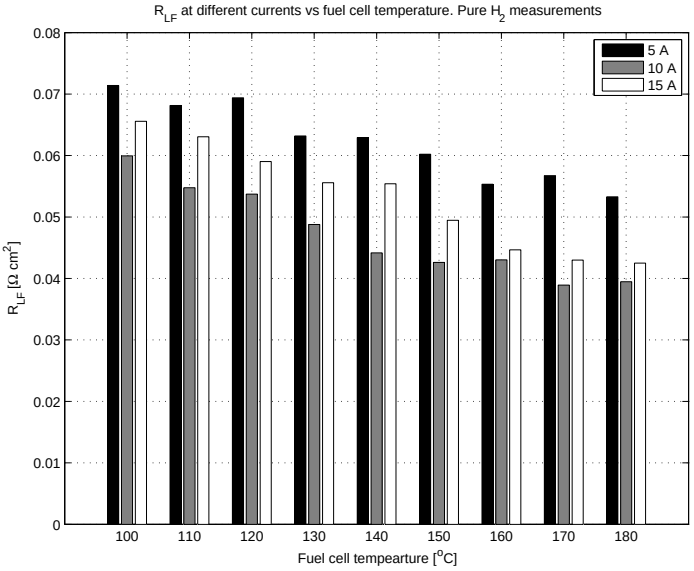

Figure 3.10 – Low frequency resistance at different currents using pure H_2. Taken from paper 1.

When adding CO and CO2 in the anode gas, changes were seen in the entire frequency range of the fuel cell. Both low, intermediate and high frequencies were affected. This is a strong indication that the arcs in the impedance spectrum are caused by a combination of phenomena on both the anode and the cathode and cannot each be attributed to one single effect as is common practise. The effects of anode gas composition on the intermediate frequency resistance at 10 A is shown in figure 3.11.

When adding CO to the fuel, an increase in ohmic resistance was observed. In the paper, this was attributed to the addition of CO, but the mechanism was not discussed. A mechanism for this behaviour could be deactivation of the catalyst closest to the membrane, forcing the anode reactions to occur closer to the CL-GDL interface. This would in turn increase the conduction losses in the anode CL. Another reason for the increase in ohmic resistance may, however, be the change in flow rate of the fuel stream. Since the anode gasses are completely dry, increasing the flow rate by 150% causes increased drying of the membrane, which results in lower conductivity. Jespersen et al. [67] observed about half the increase in ohmic resistance when increasing anode stoichiometry from 1.1 to 4. Thus it may be reasonable to assume that both phenomena play a role in the case

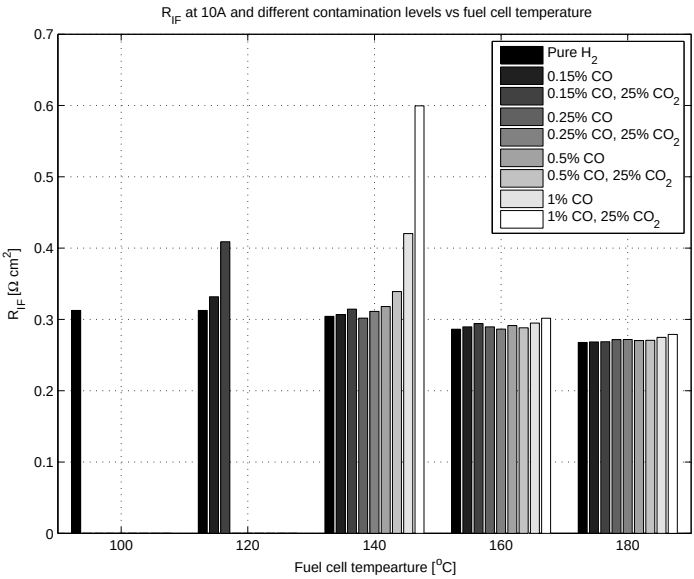

Figure 3.11 – Intermediate frequency resistance at 10 A using different operating temperatures and fuel compositions. Taken from paper 1.

at hand.

The effects on the high frequency impedance was attributed to reduced active area due to CO adsorption and reduced H2 concentration in the catalyst layer due to dilution with CO2. The effects on the intermediate and low frequency impedance were assumed to originate from limitations in H2 transport.

Two impedance measurements were conducted in each operating point in order to test the consistency of the measurements. The RMS deviation between the consecutive measurements conducted were within an acceptable range in most cases, but steady-state problems were identified at high CO concentration and low temperature. To ensure more reliable measurements in these problematic points, longer settling times for the CO adsorption are required for future tests.

3.5 Break-in studies

Paper 3 presents an investigation of the break-in of two different MEA types. These are the sol-gel based Celtec®-P MEAs and the post-doped Dapozol® 77 MEAs. Break-in studies treating both sol-gel [72, 73, 93] and post-doped [74, 94] MEAs have been published, but no studies have compare the break-in of the two types directly. The main conclusions from this study are outlined in this section.

3.5.1 Methods

MEAs were broken in for a minimum of 90 hours at 160°C and 9 A. The voltage and the impedance was recorded throughout the break-in period. The in-house set-up presented in section 3.2.1 was used for the tests. Data for the MEAs tested is given in table 3.3. The individual parts of the impedance were quantified by fitting the equivalent circuit model denoted model 3 in section 3.3.

MEA name	MEA type	Cathode Pt loading	Normalised C/PBI wt. ratio in CL	Cell area
DPS1	Dapozol® 77	0.98 mg/cm^2	1	46 cm^2
DPS2	Dapozol® 77	0.98 mg/cm^2	1.22	46 cm^2
DPS3	Dapozol® 77	0.8 mg/cm^2	1	46 cm^2
BASF1	Celtec®-P2100	–	–	45 cm^2
BASF2	Celtec®-P2100	–	–	45 cm^2
BASF3	Celtec®-P1000	0.75 mg/cm^2[39]	–	45 cm^2

Table 3.3 – Data for the MEAs used for the break-in impedance tests.

3.5.2 Contribution

The study showed that there is a significant difference between the break-in behaviour of the sol-gel MEAs and the post doped MEAs. The most significant difference can be observed in the development of the fuel cell voltage as shown in figure 3.12 and the intermediate frequency resistance as shown in figure 3.13.

The BASF MEAs seem to have a common tendency towards increasing voltage and decreasing intermediate frequency resistance (R_{IF}). The voltage increases 15-20 mV during the first 10-15 hours and subsequently levels out. After this rapid initial voltage increase, the voltage increases more or less linearly at a slower pace for all three MEAs. This continues until break-in is terminated for the BASF2 and BASF3 MEAs, while the voltage of the BASF3 MEA reaches a maximum at 40 hours and settles around 0.66 V.

When regarding the intermediate frequency resistance, a similar trend can be observed. The resistance decreases exponentially during the initial phase of the break-in and levels out to within the random variation between 20 and 40 hours. Similar results for the development of R_{IF} for Celtec®-P2100 MEAs were obtained by Galbiati et al. [72].

This suggests that the important part of the break-in is completed after around 30-40 hours. This means that the break-in time of BASF MEAs can most likely be significantly shortened from the official 100 hour recommendation without causing

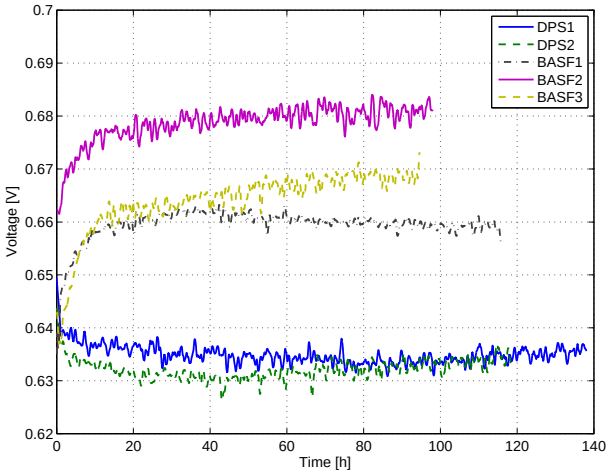

Figure 3.12 – Development of the cell voltages during the break-in period.

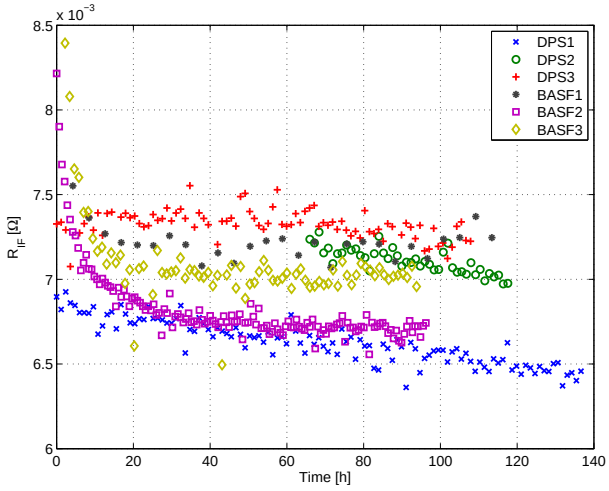

Figure 3.13 – Fitted values of the intermediate frequency resistance vs. time. Results from model 3.

performance degradation.

The DPS MEAs all exhibit less significant development. The voltage initially decreases, but after some time starts increasing again. Except for a very rapid decrease during the first hour of break-in, the voltage stays within 0.01V throughout the break-in period. The intermediate frequency resistance shows a gradual decrease throughout the break-in period. This might suggest that no significant

activation processes take place in the MEAs after the first hour, and thus they may be ready for use with little or no break-in.

In case of both MEA types, establishing whether a shorter break-in time is feasible will require further testing. A suitable test could be subjecting MEAs that have been broken in for 0, 25, 50, 75, and 100 hours to a realistic load profile for several hundred hours and comparing their performance and degradation rates.

3.6 Measurements for the modelling study

This section describes the experimental work carried out to support the modelling study. The primary part of this work is the recording of impedance spectra and polarisation curves for use when fitting the model. Apart from this, the porosity of the gas diffusion layer of the MEA has been determined.

3.6.1 Dapozol® 77 MEA data

In order to get sets of impedance spectra and polarisation curves for fitting and validating the model, a series of measurements have been performed in the laboratory. Measurement were carried out in the G60 test bench from Greenlight Innovation. The MEA was a Dapozol® 77 from Danish Power Systems®. Impedance was recorded using a Gamry Reference 3000™ impedance analyser.

The MEA has been characterised at different operating points by varying the temperature and stoichiometry. For the impedance spectra, the current is varied as well. This is done, since these variables affect the polarisation curves and the impedance spectra. The data is needed to verify whether the model is able to account for these effects. The operating parameters are given in table table 3.4.

Temperature [°C]	Stoichiometry	EIS current [A]
140	2	5
150	4	10
160		15
170		20
180		

Table 3.4 – Operating parameters for Dapozol® 77 characterisation.

The trends exhibited by the data when varying one parameter are consistent across the operating points. The trends agree with what would intuitively be expected. For the polarisation curve, the performance improves when increasing temperature or stoichiometry. Both effects increase at higher temperature. The polarisation curves are plotted in figure 3.14. The curves at lower temperature are closer together than the curves at higher temperature. Also, the difference

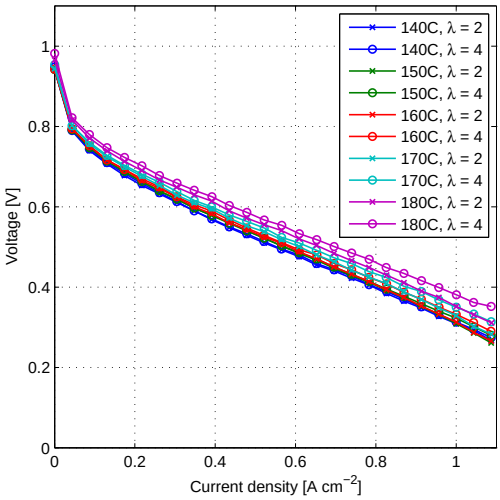

Figure 3.14 – Measured polarisation curves for the Dapozol® 77 MEA.

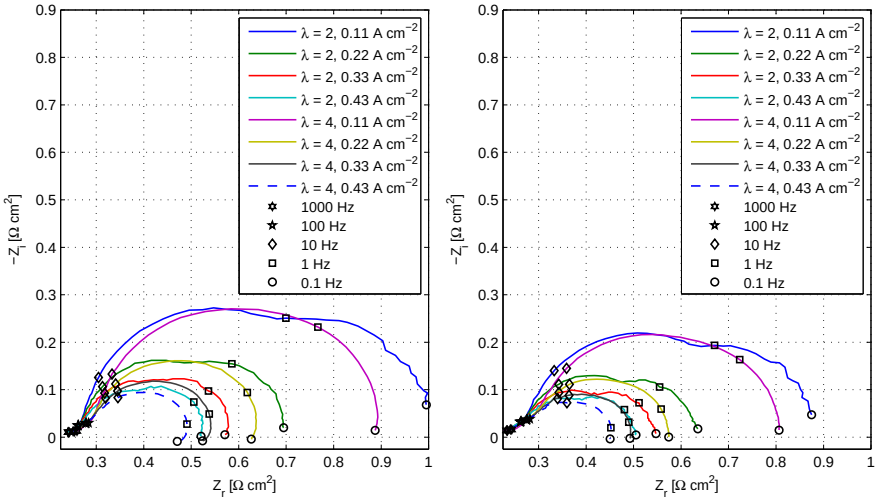

Figure 3.15 – Measured impedance spectra for the Dapozol® 77 MEA, showing the effects of stoichiometry and current. Left: $T = 140\,^{\circ}\mathrm{C}$. Right: $T = 180\,^{\circ}\mathrm{C}$.

between the curves at λ_{O_2} of 2 and 4 is almost non-existent at 140 °C but becomes pronounced along the whole current range at 180 °C.

Impedance spectra recorded at 140°C and 180°C are plotted in figure 3.15. The impedance spectra also exhibit trends, which are in line with expectations.

When increasing the current, the impedance is reduced. This follows from the reduced slope of the polarisation curve at higher current densities. The effect of stoichiometry also agrees with previously published results [67]. Lowering the stoichiometry results in an increase of the low frequency capacitive contribution. At $0.11\,\mathrm{A\,cm^{-2}}$ this contribution covers the range $1 - 0.1\,\mathrm{Hz}$. At higher current densities, the effect becomes pronounced at higher frequencies. The effects are comparable at both ends of the temperature range. When comparing with the polarisation curves, this raises a question. How come, that the stoichiometry has the same effect on the impedance at 140 °C and 180 °C, when the effect on the polarisation curve is significant at 180 °C but negligible at 140 °C? The explanation could be that the effects of stoichiometry on the impedance spectrum are mainly transient and thus decoupled from the steady state performance. A plausible source of such an effect could be compounded oscillations in O_2 concentration in the flow channel [88, 89].

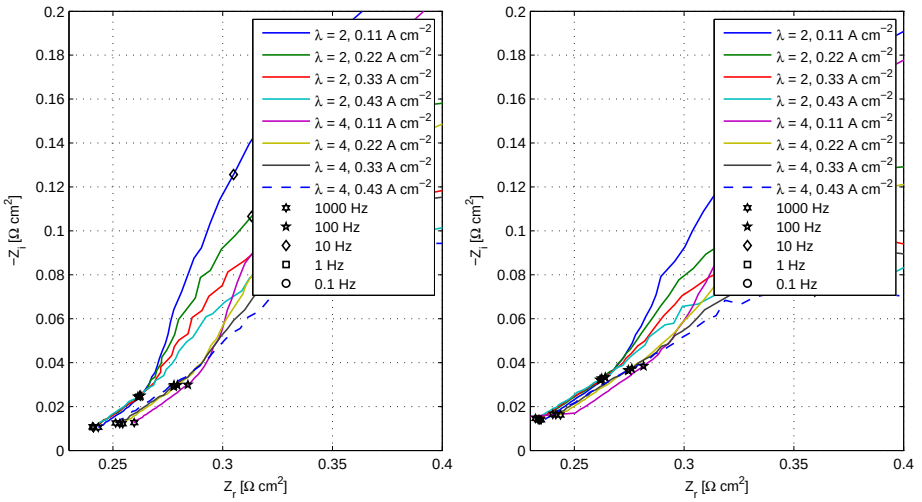

Figure 3.16 – Measured impedance spectra for the Dapozol® 77 MEA, showing the effects of stoichiometry and current. Zoom on the high frequency region. Left: $T = 140\,^{\circ}\mathrm{C}$. Right: $T = 180\,^{\circ}\mathrm{C}$.

Zooming in on the high frequency region of the impedance spectra (figure 3.16), it can be seen, that the patterns in this region are similar at high and low temperatures. At low stoichiometry, the resistance is lower and the curves are almost coinciding in the range $1\,\mathrm{kHz} - 100\,\mathrm{Hz}$. At $\lambda = 4$, the resistance is generally higher, owing to drier conditions, but the resistance also decreases as the current is increased. The difference in resistance between $\lambda = 2$ and $\lambda = 4$ is smaller at high temperatures. Also, the 45° slope in the range $1\,\mathrm{kHz} - 100\,\mathrm{Hz}$ is more pronounced at high temperature.

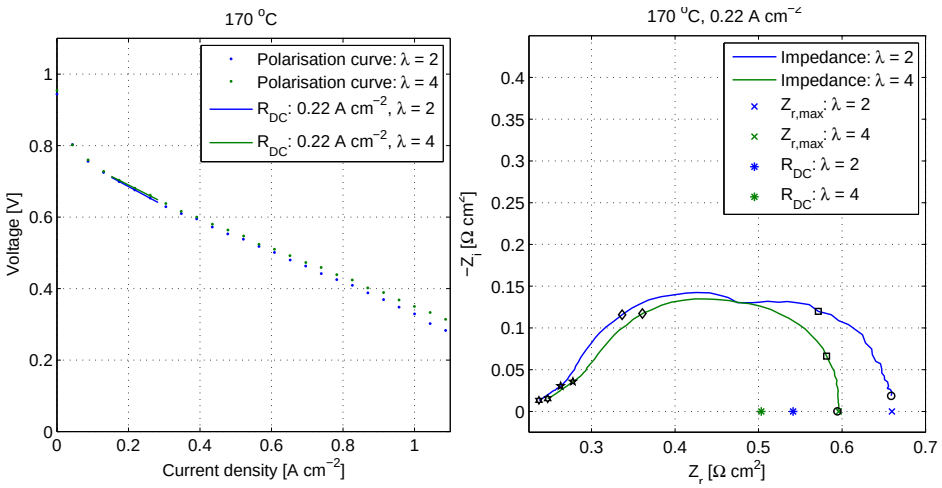

Figure 3.17 – Illustration of the meaning of R_{DC} and $Z_{\mathrm{r,max}}$. Left: The polarisation curve slope corresponding to R_{DC} at $0.22\,\mathrm{A\,cm^{-2}}$. Right: Impedance spectra at $0.22\,\mathrm{A\,cm^{-2}}$ and corresponding values of R_{DC} and $Z_{\mathrm{r,max}}$.

Another detail, which is of interest when modelling the relation between impedance and polarisation curves, is the relation between the maximum real part of the impedance spectrum at given operating conditions and the slope of the polarisation curve at the same conditions. This relationship can give a hint of how important 'purely transient' contributions are in the impedance spectrum compared to those effects that directly affect the polarisation curve. The relevant ratio is calculated as:

$$r_{\mathrm{max}} = \frac{Z_{\mathrm{r,max}}}{R_{\mathrm{DC}}} \tag{3.4}$$

where $Z_{\mathrm{r,max}}\ \left[\Omega\,\mathrm{cm^2}\right]$ is the maximum real part of the impedance spectrum and $R_{\mathrm{DC}} = \frac{dV}{di}_{\mathrm{pol}}\ \left[\Omega\,\mathrm{cm^2}\right]$ is the slope of the polarisation curve around the impedance current at the same operating conditions. An illustration of $Z_{\mathrm{r,max}}$ and R_{DC} at 170°C and $0.22\,\mathrm{A\,cm^{-2}}$ is given in figure 3.17. As can be seen from the figure, there can be a significant difference between $Z_{\mathrm{r,max}}$ and R_{DC} due to transient phenomena.

When $r_{\mathrm{max}} > 1$ it is an indication that purely transient contributions play a role in the impedance spectrum. This means that resistances derived from fitting an equivalent circuit model will not accurately reflect the losses in the system. Consequently, any attempts to deduce the polarisation behaviour of the cell from impedance spectra will tend to over predict the losses. A model that wishes to capture both steady state and impedance behaviour will have to account for these

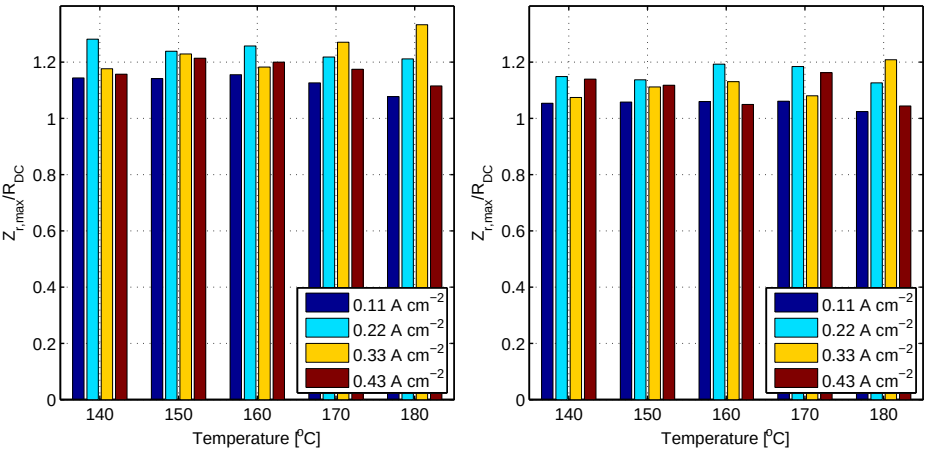

Figure 3.18 – Plot of the ratio of the maximum real part of the impedance spectra to the slope of the polarisation curve at the impedance current. The left plot contains the values for $\lambda = 2$ and the right plot for $\lambda = 4$.

transient effects.

On the other hand, if $r_{\max} = 1$ and the imaginary part corresponding to $Z_{\mathrm{r,max}}$ is close to zero, it is likely that there are no significant effects of a purely transient nature and that the all important contributions have shorter time scales than the lowest frequency used.

$r_{\max} < 1$ would indicate, that the frequency range used is insufficient to capture all of the transient effects. This can also be the case when $r_{\max} >= 1$. An indication of this would be that the imaginary part corresponding to $Z_{\mathrm{r,max}}$ is far from zero.

The value of the real part at the lowest frequency ($Z_{\mathrm{r,lf}}$ $\left[\Omega\,\mathrm{cm}^2\right]$) can similarly give an indication of whether it can be assumed that all significant dynamics have time scales within the frequency window investigated. This would be the case when (3.5) is close to 1, and the imaginary part of the impedance at the lowest frequency is close to zero.

$$r_{\mathrm{lf}} = \frac{Z_{\mathrm{r,lf}}}{R_{\mathrm{DC}}} \tag{3.5}$$

Figures 3.18 and 3.19 show $r_{\max}$ and r_{lf} for all data sets respectively. As can be seen, both values are generally larger than 1, increasing slightly with increasing impedance current. The ratios are generally smaller at $\lambda = 4$. Also, the difference between r_{lf} and $r_{\max}$ is small. Note that these values are subject to some random variation, since small inaccuracies in the polarisation curve or the low frequency part of the impedance spectrum have significant effect on r_{lf} and $r_{\max}$. The ratios

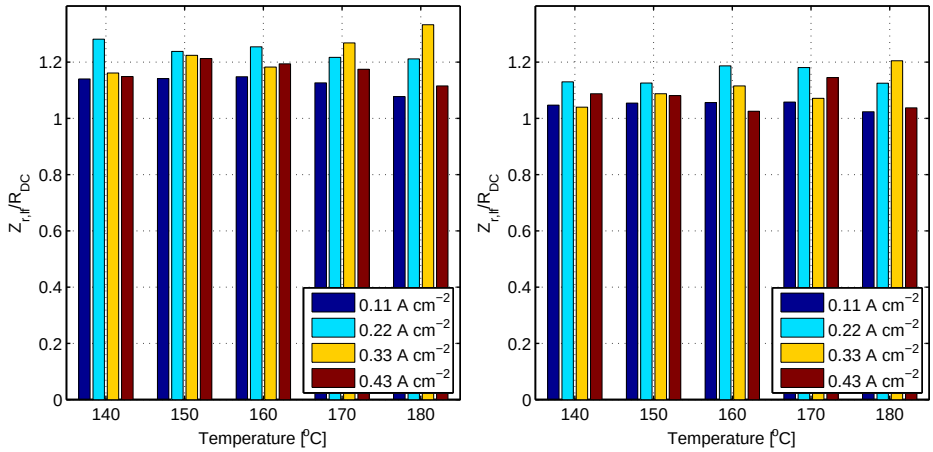

Figure 3.19 – Plot of the ratio of the real part of the impedance at 0.1 Hz to the slope of the polarisation curve at the impedance current. The left plot contains the values for $\lambda = 2$ and the right plot for $\lambda = 4$.

indicate that there are indeed some important low frequency phenomena that have longer time scales than 10 seconds. This could be related to water dynamics in the membrane. A study by Gu et al. [95] showed that the settling time for the water content of a PA-PBI membrane was around 5 minutes above 100 °C.

The data presented in this section is intended for use in fitting and validating the mechanistic impedance model. A sufficiently good model should be able to fit the data simultaneously at multiple operating points. It should also be able to reproduce the trends in the data with respect to temperature, stoichiometry and impedance current density outside the fitting range.

3.6.2 GDL porosity measurement

The Dapozol® 77 uses GDLs of the type Freudenberg H2315 C2. The porosity was not reported in the data sheet, so porosity was investigated using a Porotech 3.1 Standard Porosimeter. The gas diffusion layer was pealed of the MEA after characterisation using a pair of tweezers. The thickness was measured with a micrometer gauge and a circular sample of diameter 2.3 cm was cut. The sample was dried under vacuum for 120 minutes. The dry sample was put in a glass bottle and weighed using a ACCULAB ALC-210.4 precision scale. Subsequently, the sample was soaked in octane for 20 minutes under vacuum to drive out all gas. The wet sample was weighed in the same bottle, and the porosity was calculated from the following formula:

$$\epsilon_{\text{exp}} = \frac{m_{\text{wet}} - m_{\text{dry}}}{\rho_{\text{Octane}} \cdot V_{\text{sample}}} \tag{3.6}$$

Where m_{wet} [g] is the mass of the wet sample in the bottle and m_{dry} [g] is the dry mass of the same. ρ_{Octane} $\left[\text{g cm}^{-3}\right]$ is the density of octane and V_{sample} $\left[\text{cm}^3\right]$ is the sample volume. For comparison, the porosity is also calculated using the data from the data sheet [96] and assuming, that the carbon fibres have density similar to that of graphite.

$$\epsilon_{\text{calc}} = 1 - \frac{\rho_{\text{GDL}} t_{\text{GDL}}}{\rho_{\text{graphite}} t_{\text{GDL}}} \tag{3.7}$$

The necessary data for the calculations are given in table 3.5 along with the results. As can be seen, the results are quite close. For modelling purposes, the experimentally derived value will be used.

Parameter	Value	Comment
m_{wet}	$31.9374\,\text{g}$	Measured
m_{dry}	$31.8784\,\text{g}$	Measured
V_{sample}	$0.108\,\text{cm}^3$	Calculated from measured dimensions
ρ_{Octane}	$0.703\,\text{g cm}^{-3}$	[97]
$\rho_{\text{GDL}} t_{\text{GDL}}$	$135\,\text{g m}^{-2}$	[96]
t_{GDL}	$260\,\mu\text{m}$	Measured
ρ_{graphite}	$2.2\,\text{g cm}^{-3}$	[98]
ϵ_{exp}	0.78	
ϵ_{calc}	0.76	

Table 3.5 – Porosity measurement and control calculation data.

3.7 Summary

The experimental work related to this Ph.D. project has explored some of the possibilities for applying EIS in diagnosis of HTPEM fuel cells. The applicability of EIS for investigating the effects of CO on the performance of the cell has been demonstrated. CO was shown to affect the whole impedance spectrum. The challenges in terms of achieving steady state measurements when dealing with slow processes like CO poisoning have also been highlighted. It has been demonstrated that EIS can supplement voltage measurements when monitoring the break-in process. Also, the significant differences in the break-in process of HTPEM fuel cells using either post-doped or sol-gel MEAs have been pointed out. The analysis of the impedance and voltage data indicates that break-in

times for sol-gel MEAs can be significantly shortened with respect to current recommendation and that post-doped MEAs need almost no break-in.

Chapter 4

Modelling

In this section, the mathematical framework for the fuel cell model is presented. The fuel cell model is developed using the MATLAB® software package. The model takes into account species transport, electrode kinetics, potential distribution and effects of phosphoric acid water content on the electrochemical processes. The model is intended to be solved in both steady-state and dynamic mode to generate polarisation curves and impedance spectra.

The model described in this section is the result of many iterations of implementation and testing different modelling approaches and sub-models. Preliminary incarnations of the model have been published in paper 2 and in poster 1. These models differ significantly from the model described below. Partly by being resolved in 2D and partly by the way individual parts of the fuel cell are modelled. The results of the initial modelling studies were not sufficiently good for reliable parameter estimation, and they will thus not be treated further here. They have, however, helped pave the way for the current incarnation of the model, which is described below.

4.1 Assumptions and simplifications

In this section, the necessary assumptions and simplification made in order to develop the model are presented.

4.1.1 Assumptions

The following simplifying assumptions have been made in the development of the model:

- All species are assumed to obey the ideal gas law.
- The temperature is assumed constant throughout the fuel cell.

- The anode processes are disregarded in the calculations.
- The feed air consists only of N_2, O_2, and H_2O.
- The flow in the gas channel can be considered plug flow.
- The gas diffusion layer and the catalyst layer is assumed to be macro-homogeneous.
- The micro-porous layer on the GDL is neglected in the model. Its effects are lumped with those of the GDL.
- The catalyst particles are assumed to be dispersed uniformly on the surface of the catalyst layer solid phase.
- The catalyst layer phosphoric acid is evenly distributed over the entire surface of the solid phase.
- The phosphoric acid and the gas phase are assumed to be in equilibrium with respect to water content.
- Reactions proceed via one dominant reaction pathway. No parallel reaction paths are considered.

Figure 4.1 shows an illustration of the catalyst layer model.

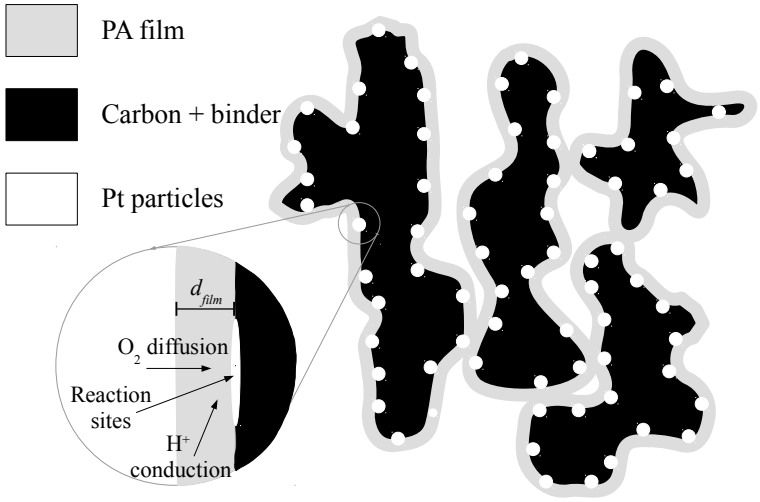

Figure 4.1 – Drawing of the assumed structure of the catalyst layer.

4.1.2 Computational domain

The fuel cell is resolved in 1D through the membrane. The channel is resolved separately along the length in order to better account for the effect on the fuel cell dynamics. An illustration of the computational domain is given in figure 4.2.

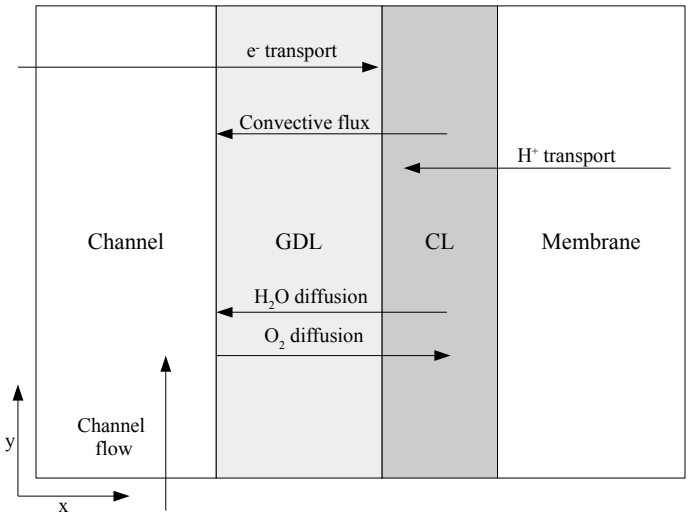

Figure 4.2 – Schematic representation of the computational domain.

In order to represent the flow field dynamics as accurately as possible without resolving the model across the channel, some simplifications of the flow field geometry have been implemented. Instead of three serpentine channels separated by a land area, the fuel cell is assumed to have one straight channel of cross sectional area equal to that of the three channels and width equal to the width of the channels plus the land. If capital letters denote actual dimensions and lower case letters denote the simplified model geometry, the width and height of the model channel is given in (4.1). The notation used is shown in figure 4.3.

$$\begin{aligned} w_{\text{channel}} &= 3(W_{\text{channel}} + W_{\text{land}}) \\ h_{\text{channel}} &= \frac{W_{\text{channel}} H_{\text{channel}}}{W_{\text{channel}} + W_{\text{land}}} \end{aligned} \tag{4.1}$$

As the land covers a significant part of the fuel cell area, the average effective diffusion length from the channel to the catalyst layer will be longer than the thickness of the GDL. This is accounted for by taking a weighted average of the diffusion length under the land and under the channel as shown in (4.2). Again,

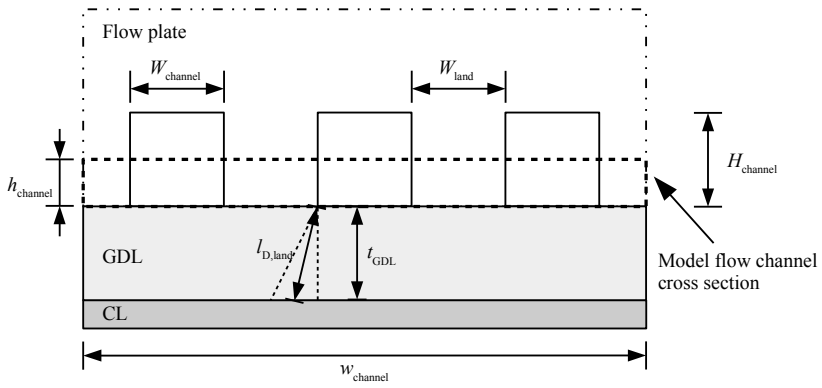

Figure 4.3 – Illustration of the dimensions considered in (4.1) and (4.2).

the notation is shown in figure 4.3.

$$\begin{aligned} l_{\mathrm{D,GDL}} &= \frac{W_{\mathrm{land}} l_{\mathrm{D,land}} + W_{\mathrm{channel}} t_{\mathrm{GDL}}}{W_{\mathrm{land}} + W_{\mathrm{channel}}} \\ &= \frac{W_{\mathrm{land}} \sqrt{t_{\mathrm{GDL}}^2 + \left(\frac{1}{2} W_{\mathrm{land}}\right)^2} + W_{\mathrm{channel}} t_{\mathrm{GDL}}}{W_{\mathrm{land}} + W_{\mathrm{channel}}} \end{aligned} \tag{4.2}$$

The geometry considerations are illustrated in figure 4.3.

4.1.3 A note on discretisation

Since the model is solved numerically, the computational domain must be discretised. The discretisation is made using the finite volume method as described in Versteeg and Malalasekera [99]. The basic discretisation is standard, but the determination of the cell face values deserves a few comments.

The cell face values of conductivity and diffusion coefficient are calculated using the resistance network approach. The notation for the calculations is shown in figure 4.4. Upper case subscripts denote cell centroid values and lower case subscripts denote cell face centroid values. If k is either a diffusion coefficient or a conductivity, the value at cell face w is calculated as in (4.3).

$$k_{\mathrm{w}} = \frac{\Delta x_{\mathrm{P}} + \Delta x_{\mathrm{W}}}{\Delta x_{\mathrm{P}}/k_{\mathrm{P}} + \Delta x_{\mathrm{W}}/k_{\mathrm{W}}} \tag{4.3}$$

For the convective transport, the cell face value of the transported parameter is determined using linear upwind differencing. The value is calculated as the upwind value plus the distance from the upwind cell centroid to the cell face

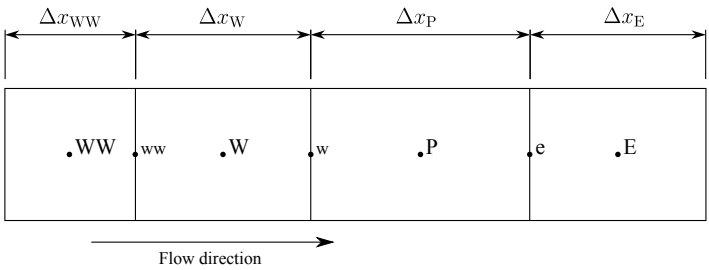

Figure 4.4 – Schematic representation of the notation used in the discretisation calculations.

times the upwind gradient. If ϕ is the transported parameter, the value at cell face e is:

$$\phi_e = \phi_P + \frac{\Delta x_W (\phi_P - \phi_W)}{\Delta x_P + \Delta x_W} \tag{4.4}$$

4.2 Model dynamics

This section deals with the equations governing the steady state and dynamic behaviour of the fuel cell model. The equations express the time rate of change of the variables, for which the model is solved. Subsequent sections are devoted to the details of each equation.

4.2.1 Reactant transport

In the transport of species, diffusion, convection and generation is taken into account. Oxygen and water are accounted for in this way. The conservation of nitrogen is taken care of by continuity. The convective and diffusive terms are identical for both species.

$$\frac{\partial c_x}{\partial t} = \frac{\nabla (\mathbf{u} c_x) + \nabla (c D_x \nabla y_x) + S_x}{\epsilon} \tag{4.5}$$

Here D_x $\left[\mathrm{m^2\,s^{-1}}\right]$, c $\left[\mathrm{mol\,m^{-3}}\right]$ and y are the diffusion coefficient, total concentration, and mole fraction, respectively. Subscript x denotes the species. ϵ is the local porosity. The source terms for oxygen $\left(S_{O_2}\ \left[\mathrm{mol\,m^{-3}\,s^{-1}}\right]\right)$ and water $\left(S_{H_2O}\ \left[\mathrm{mol\,m^{-3}\,s^{-1}}\right]\right)$ as shown in (4.6) and (4.8) . The source terms are zero outside the catalyst layer.

S_{O_2} is the perceived oxygen consumption rate in the catalyst layer pores. It is equal to the rate of removal of O_2 from the gas phase by diffusion to the catalyst sites through the PA film. It is calculated in (4.6) as the product of the catalyst

surface area per unit volume of the CL ($A_{\mathrm{Pt,V}}\left[\mathrm{m^2 m^{-3}}\right]$) and the diffusion flux of oxygen to the catalyst sites ($r_{\mathrm{O_2,film}}\left[\mathrm{mol\,m^{-2} s^{-1}}\right]$).

$$S_{\mathrm{O_2}} = -r_{\mathrm{O_2,film}} \cdot A_{\mathrm{Pt,V}} \tag{4.6}$$

$r_{\mathrm{O_2,film}}$ is calculated using (4.7). Here $c_{\mathrm{O_2,PA}}$ and $c_{\mathrm{O_2,Pt}}$ $\left[\mathrm{mol\,m_{PA}^{-3}}\right]$ are the equilibrium concentration of O_2 in phosphoric acid and the concentration of O_2 at the Pt catalyst respectively. The interface between the gas phase and the acid phase is assumed to be in equilibrium. $D_{\mathrm{O_2,film}}\left[\mathrm{m^2\,s^{-1}}\right]$ is the diffusion coefficient of oxygen in the acid film.

$$r_{\mathrm{O_2,film}} = D_{\mathrm{O_2,film}} \frac{c_{\mathrm{O_2,PA}} - c_{\mathrm{O_2,Pt}}}{d_{\mathrm{film}}} \tag{4.7}$$

The expression for $S_{\mathrm{H_2O}}$ is given in (4.8). Here $c_{\mathrm{H_2O,tot}}$ is the total water content in the CL including both PA and gas phase. $r_{\mathrm{H_2O,gen}}$ and $r_{\mathrm{H_2O,con}}$ $\left[\mathrm{mol\,m^{-2} s^{-1}}\right]$ are the rates of generation and consumption of H_2O per catalyst ESA. $\frac{\partial c_{\mathrm{H_2O}}}{\partial c_{\mathrm{H_2O,tot}}}$ is the rate of change of the water concentration in the gas phase with respect to the total water concentration in the gas and the solid phase.

$$\begin{aligned}
S_{\mathrm{H_2O}} &= \left(r_{\mathrm{H_2O,gen}} - r_{\mathrm{H_2O,con}}\right) A_{\mathrm{Pt,V}} + \dot{c}_{\mathrm{H_2O,corr}} \\
&= \left(r_{\mathrm{H_2O,gen}} - r_{\mathrm{H_2O,con}}\right) A_{\mathrm{Pt,V}} + \frac{\partial c_{\mathrm{H_2O,tot}}}{\partial t} \left(\frac{\partial c_{\mathrm{H_2O}}}{\partial c_{\mathrm{H_2O,tot}}} - 1\right) \\
&= \left(r_{\mathrm{H_2O,gen}} - r_{\mathrm{H_2O,con}}\right) A_{\mathrm{Pt,V}} \frac{\partial c_{\mathrm{H_2O}}}{\partial c_{\mathrm{H_2O,tot}}} \\
&\quad + \left(\nabla\left(\mathbf{u} c_{\mathrm{H_2O}}\right) + \nabla\left(c D_{\mathrm{H_2O}} \nabla y_{\mathrm{H_2O}}\right)\right) \left(\frac{\partial c_{\mathrm{H_2O}}}{\partial c_{\mathrm{H_2O,tot}}} - 1\right)
\end{aligned} \tag{4.8}$$

Since PA absorbs water from the gas phase, the rate, at which the water concentration in the gas phase changes, is coupled to the water content of the PA. Since equilibrium is assumed, the rate of change of the local water content in the gas is significantly slowed by the relatively large water content of the acid phase.

4.2.2 Continuity

Continuity is assured in the model, by solving for the molar concentration within the porous media. The terms relevant for continuity are the convective transport of species and the mass source term.

$$\frac{\partial c}{\partial t} = \frac{-\nabla\left(\mathbf{u} c\right) + S_{\mathrm{c}}}{\epsilon} \tag{4.9}$$

Here c $\left[\mathrm{mol\,m^{-3}}\right]$ is total molar concentration, $\mathbf{u}$ $\left[\mathrm{m\,s^{-1}}\right]$ is the velocity vector and ϵ is the porosity. The source term S_{c} $\left[\mathrm{mol\,m^{-3}\,s^{-1}}\right]$, given in (4.10), is the sum of the source terms for water and oxygen.

$$S_{\mathrm{c}} = S_{\mathrm{O_2}} + S_{\mathrm{H_2O}} \tag{4.10}$$

4.2.3 Reactants at catalyst sites

The concentrations of reactants at the catalyst sites change with the generation and consumption of said reactants. For oxygen, the concentration is also affected by the speed of diffusion through the acid film. The dynamics of the dissolved oxygen is given in (4.11). $r_{\mathrm{O_2}}$ $\left[\mathrm{mol\,m_{Pt}^{-2}\,s^{-1}}\right]$ is the conversion rate of oxygen per Pt surface area. This equation is the same for all reaction models. For reaction mechanisms consisting of multiple steps, the dynamics of intermediate specie i are governed by (4.12). Here $r_{i,\mathrm{gen}}$ and $r_{i,\mathrm{con}}$ $\left[\mathrm{mol\,m_{Pt}^{-2}\,s^{-1}}\right]$ are the rates of generation and consumption of the intermediate per catalyst surface area.

$$\frac{\partial c_{\mathrm{O_2,Pt}}}{\partial t} = \frac{\left(r_{\mathrm{O_2,film}} - r_{\mathrm{O_2}}\right) A_{\mathrm{Pt,V}}}{d_{\mathrm{film}}} \tag{4.11}$$

$$\frac{\partial c_{i,\mathrm{Pt}}}{\partial t} = r_{i,\mathrm{gen}} - r_{i,\mathrm{con}} \tag{4.12}$$

4.2.4 Overpotential

The cathode activation overpotential is governed by (4.13). Here η [V] is the overpotential, κ_{i} $\left[\mathrm{S\,m^{-1}}\right]$ is the ionic conductivity, ϕ [V] is the membrane phase potential, j_{V} $\left[\mathrm{A\,m^{-3}}\right]$ is the current density per catalyst layer volume, and $C_{\mathrm{dl,V}}$ $\left[\mathrm{F\,m^{-3}}\right]$ is the double layer capacitance.

$$\frac{\partial \eta}{\partial t} = \frac{\nabla\left(\kappa_{\mathrm{i}} \nabla \phi\right) - j_{\mathrm{V}}}{C_{\mathrm{dl,V}}} \tag{4.13}$$

4.3 Sub-models

This section deals with the sub-models describing the quasi-steady parameters. Emphasis is put on modelling the influence of PA concentration on the catalyst layer properties.

4.3.1 Phosphoric acid concentration

The concentration of phosphoric acid is an important parameter in modelling HTPEM fuel cells, since it influences most of the processes happening in the fuel cell to some extend. MacDonald and Boyack [100] measured the mutual dependence of water vapour partial pressure, phosphoric acid concentration, and temperature. From this data they developed an expression for the water vapour partial pressure as a function of H_3PO_4 mole fraction and temperature. This

relation was only valid for H_3PO_4 mole fractions up to 1, even though their data included points of higher concentrations. For the present work, it has been chosen to develop a new relation, expressing the weight fraction of H_3PO_4 as a function of water vapour partial pressure and temperature. This allows for using the whole data range as well as determining the concentration directly without iteration.

The suggested relation is given in (4.14). Here T is temperature in K and p_{H_2O} is water vapour partial pressure in Pa. The proposed equation was fitted to the data using the MATLAB® Curve fitting toolbox. The coefficient values are given in table 4.1.

$$w_{H_3PO_4} = \frac{a_0 + a_1 \cdot (T - 273.15) + (b_0 + b_1 \cdot (T - 273.15)) \cdot \ln\left(p_{H_2O}\right)}{100} + \frac{\left(c_0 + c_1 \cdot (T - 273.15) + c_2 \cdot (T - 273.15)^2\right) \cdot p_{H_2O}}{100} \tag{4.14}$$

Coefficient	i		
	0	1	2
a_i	108.000522	$5.55230211 \cdot 10^{-2}$	-
b_i	-2.40049611	$3.18506367 \cdot 10^{-3}$	-
c_i	$-1.31390952 \cdot 10^{-3}$	$1.32974352 \cdot 10^{-5}$	$-3.50261017 \cdot 10^{-8}$

Table 4.1 – Coefficients for the PA concentration fit of (4.14).

Figure 4.5 shows the temperature and water vapour partial pressure dependence of the concentration of phosphoric acid. The fitted values deviate only very slightly from the data points. The RMS error is 0.65% of the data range and the R^2 value is 0.999. As can be seen from the lines for 110 °C and 190 °C in figure, extrapolating outside the temperature range gives values within a reasonable range.

When using the concentration of PA to determine other properties of the fuel cell, the H_3PO_4 weight fraction is not always the best regression variable. It may be beneficial to use the mole fraction of phosphorous pentoxide (P_2O_5) instead. The conversion of $w_{H_3PO_4}$ to $y_{P_2O_5}$ is given in (4.15) and (4.16).

$$w_{P_2O_5} = w_{H_3PO_4} \cdot \frac{M_{H_3PO_4}}{M_{P_2O_5}} = w_{H_3PO_4} \cdot 0.724 \tag{4.15}$$

$$y_{P_2O_5} = \frac{w_{P_2O_5}/M_{P_2O_5}}{w_{P_2O_5}/M_{P_2O_5} + \left(1 - w_{P_2O_5}\right)/M_{H_2O}} \tag{4.16}$$

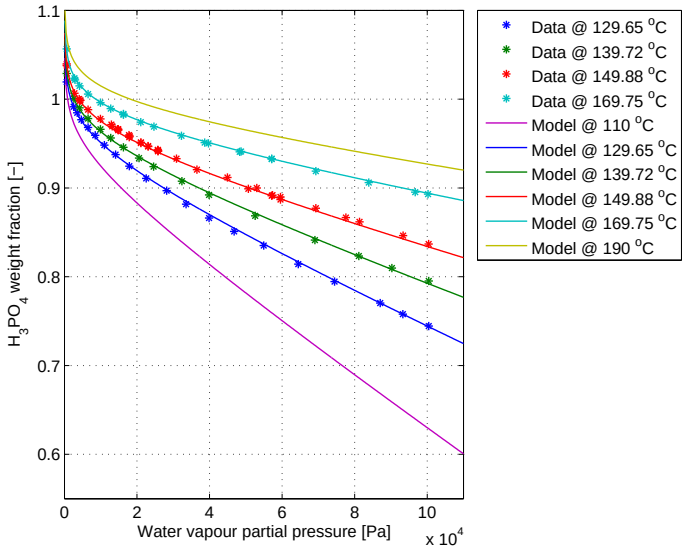

Figure 4.5 – Data points and fitted values of H_3PO_4 weight fraction as a function of water vapour partial pressure at different temperatures [100].

The molar concentration, $c_{H_2O,PA}\left[\mathrm{mol\,m^{-3}}\right]$ of water in the acid is also a useful property. This is calculated from the density of the acid, $\rho_{PA}\left[\mathrm{kg\,m^{-3}}\right]$ and $y_{P_2O_5}$.

$$c_{H_2O,PA} = \frac{\rho_{PA} \cdot \left(1 - y_{P_2O_5}\right)}{M_{H_2O}} \tag{4.17}$$

It should be noted that this number is not a measure of the amount of "free" water, but rather a measure of how much water it would be theoretically possible to extract if all the acid was dehydrated to P_2O_5.

The acid density is calculated using the relation in (4.18), developed by MacDonald and Boyack [100]. The coefficient values are given in table 4.2.

$$\rho_{PA} = 10^3 \left(A_0 + A_1 w_{H_3PO_4} - \left(A_2 - A_3 w_{H_3PO_4}\right)(T - 273.15)\right) \tag{4.18}$$

Coefficient	A_0	A_1	A_2	A_3
Value	0.68235	1.2011	$1.2379 \cdot 10^{-3}$	$3.7938 \cdot 10^{-4}$

Table 4.2 – Density relation coefficients [100].

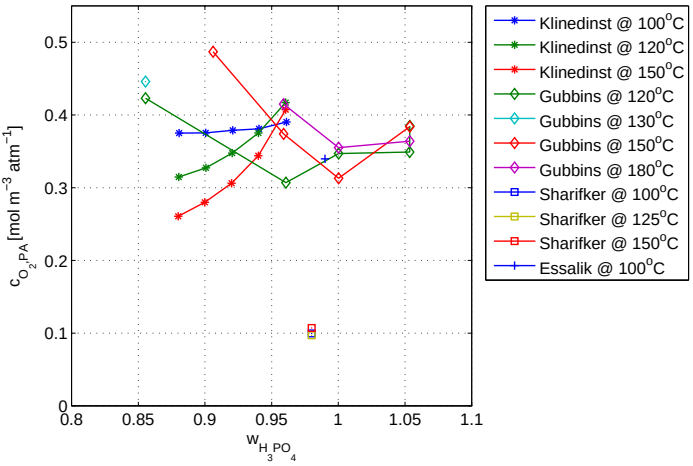

Figure 4.6 – Oxygen solubility in PA. Data from several sources [101–104].

4.3.2 Oxygen in phosphoric acid

The most comprehensive studies of the solubility and diffusion coefficient of oxygen in phosphoric acid (PA) were made by Klinedinst et al. [101] and Gubbins and Walker [102]. Solubility in this work is defined as the number of moles of solute per m^{3}of solution at a gas phase partial pressure of 1 atm of the solute.

Klinedinst et al. [101] determined the diffusion coefficient of oxygen in PA $\left(D_{O_2,PA}\right)$ and the diffusion coefficient-solubility product $\left(Dc_{O_2,PA}\right)$. They were calculated from the transient response of an electrode submerged in PA at different temperatures and concentrations. The solubility $\left(c_{O_2,PA}\right)$ was then determined by taking the ratios the linear regressions of $Dc_{O_2,PA}$ and $D_{O_2,PA}$ with respect to H_3PO_4 wt% at each temperature. The resulting solubility decreased with temperature below a H_3PO_4 concentration of 95 wt% and increased with concentration. Gubbins and Walker [102] also measured solubility, but only reported two values of $D_{O_2,PA}$ at low temperature and 85 wt% H_3PO_4. Here the solubility was found to increase with temperature and decrease with concentration up to 100 wt% and subsequently level out. Other data at only one PA concentration was presented by Essalik et al. [103] and Scharifker et al. [104]. An overview of the solubility data is given in figure 4.6. As can be seen, the data of Gubbins and Walker [102] and Klinedinst et al. [101] is in the same ballpark in spite of the opposite trends with temperature and concentration. This is also true of the data from Essalik et al. [103], but Scharifker et al. [104] found significantly lower values.

Comparing the solubility data of Gubbins and Walker [102] and Klinedinst et al. [101], a thought springs to mind. What if the reason for the trends observed by Klinedinst et al. [101] is merely a result of the choice of regression, rather than

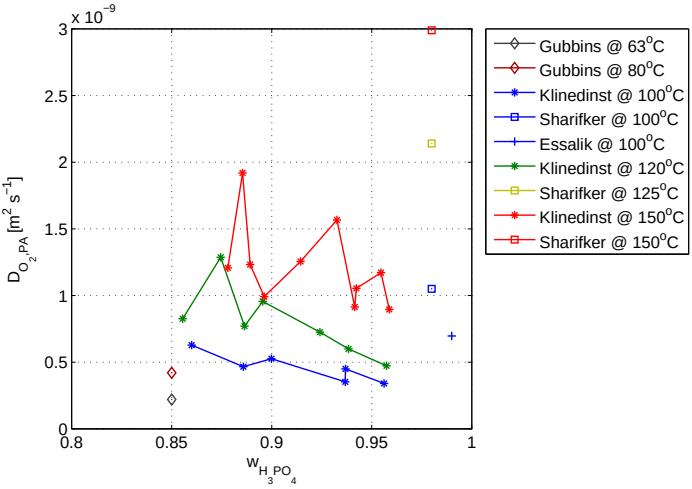

Figure 4.7 – Oxygen diffusion coefficient in PA. Data from several sources [101–104].

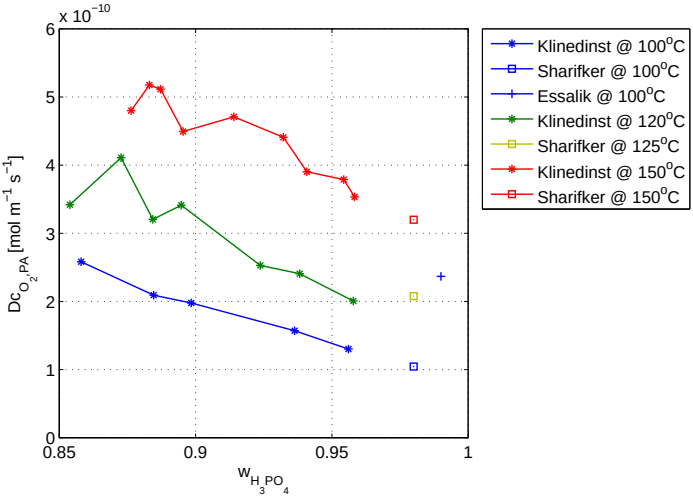

Figure 4.8 – Oxygen diffusion coefficient-solubility product in PA. Data from several sources [101, 103, 104].

an actual physical phenomenon? This will have to be investigated further.

Data for diffusion coefficients from different sources are plotted in figure 4.7. As with the solubility, there is some disagreement with respect to the values found. Klinedinst et al. [101] show the diffusion coefficient to increase with temperature

and decrease with concentration. The data points are rather scattered, but no better data exists. Scharifker et al. [104] found significantly higher values. The one data point of Essalik et al. [103] also shows a higher value. The low temperature values of Gubbins and Walker [102] agree quite well with the temperature trend.

When looking at the values of $Dc_{O_2,PA}$ from Klinedinst et al. [101] in figure 4.8, an interesting detail can be observed. These values are much less scattered than the diffusion coefficient data. Also, the $Dc_{O_2,PA}$ values from Scharifker et al. [104] agree closely with the trend of Klinedinst et al. [101]. Two new correlations for $c_{O_2,PA}$ and $D_{O_2,PA}$ are developed as described below.

Diffusion coefficient

Several general relations for the diffusion coefficient of a solute in a liquid or supercritical fluid were developed by Magalhães et al. [105]. The relation chosen for fitting to the $D_{O_2,PA}$ data is given in (4.19). The relation is modified by subtracting 273.15 K from the temperature. This improves the fit.

$$D_{O_2,PA} = \exp\left(a_{D1} \cdot \ln\left(\frac{T - 273.15\,\mathrm{K}}{\mu_{PA}}\right) + a_{D2}\right) \tag{4.19}$$

The viscosity of PA (μ_{PA} $\left[kg\,m^{-1}s^{-1}\right]$) is fitted to data tabulated by Chin and Chang [106]. The fit was obtained using the MATLAB® Curve fitting toolbox. The relation is given in (4.20). Here the variables are absolute temperature T and phosphorus pentoxide mole fraction $y_{P_2O_5}$.

$$\mu_{PA} = (2.7007{\cdot}10^{-4}{+}3.7605{\cdot}10^{-3}{\cdot}y_{P_2O_5}){\cdot}\exp\left(\frac{14.626 + 1050.4 \cdot y_{P_2O_5}}{T - 273.15}\right) \tag{4.20}$$

Solubility

The idea when it comes to fitting the solubility of oxygen in PA, is to express it as a function of the solubility of oxygen in water and the mole fraction of P_2O_5. This should ensure, that the values fall within a feasible limit inside the operating range.

The molal solubility of O_2 in water ($b_{O_2,water}$ $\left[\mathrm{mol_{O2}\,kg^{-1}_{water}}\right]$) as a function of temperature is calculated using (4.21) developed by Tromans [107].

$$\begin{aligned} b_{O_2,water} = &\exp\left(\frac{0.046 \cdot T^2 + 203.35 \cdot T \cdot \ln(T/298)}{8.3144 \cdot T}\right) \cdot \\ &\exp\left(\frac{-(299.378 + 0.092 \cdot T) \cdot (T - 298) - 20.591 \cdot 10^3}{8.3144 \cdot T}\right) \end{aligned} \tag{4.21}$$

The molal solubility is converted to molar solubility:

$$c_{O_2,water} = \frac{b_{O_2,water} \cdot \rho_{sat,water}}{1 + b_{O_2,water} \cdot M_{O_2}}; \tag{4.22}$$

Here $\rho_{\text{sat,water}}$ $\left[\text{kg m}^{-3}\right]$ is the density of saturated liquid water at the relevant temperature.

The empirical expression shown in (4.23) is fitted to the solubility data of Gubbins and Walker [102].

$$c_{\text{O}_2,\text{PA}} = \frac{c_{\text{O}_2,\text{water}} \cdot a_{c1}^{y_{\text{P}_2\text{O}_5}}}{a_{c2} \cdot \left(1 + y_{\text{P}_2\text{O}_5}\right)^2} + a_{c3} \cdot y_{\text{P}_2\text{O}_5}^2 \tag{4.23}$$

Fits

The fits are produced by simultaneously minimising the RMS deviation between (4.23) and the Gubbins and Walker [102] solubility data, the RMS deviation between (4.19) and the Klinedinst et al. [101] $D_{\text{O}_2,\text{PA}}$ data, and the RMS deviation between the product of (4.23) and (4.19) and the Klinedinst et al. [101] $Dc_{\text{O}_2,\text{PA}}$ data. The fits are deemed acceptable given the limitations of the data. The values of the fitting coefficients are given in table 4.3.

			x		
Fit		Coefficient	1	2	3
Diffusion coefficient	$D_{\text{O}_2,\text{PA}}$	a_{Dx}	0.654661162430493	6.72763244794933	-
Solubility	$c_{\text{O}_2,\text{PA}}$	a_{cx}	4.11500117966429e-05	0.296030815669062	3.23663842302862

Table 4.3 – Fit coefficients of the solubility and diffusion coefficients in PA

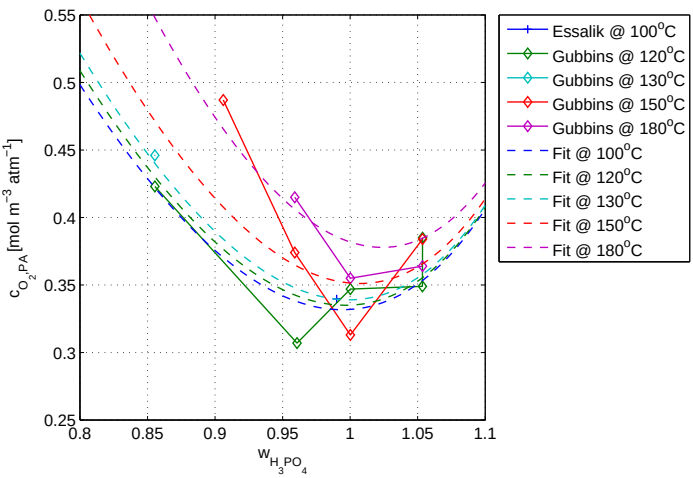

Figure 4.9 – Oxygen solubility in PA. Fit compared to data [102, 103].

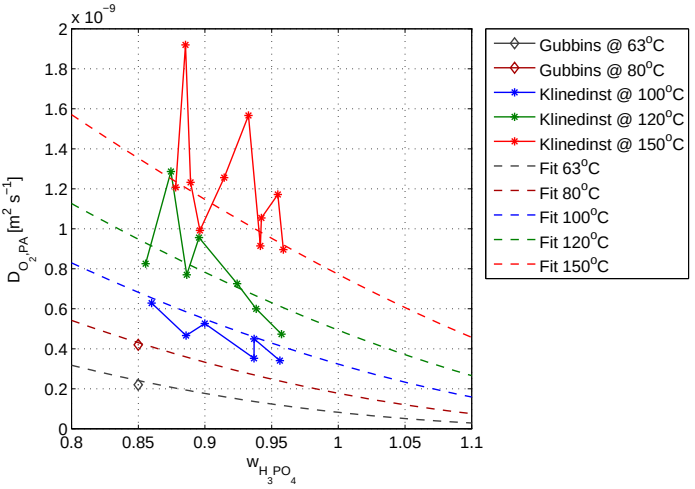

Figure 4.10 – Oxygen diffusion coefficient in PA. Fit compared to data [101, 102].

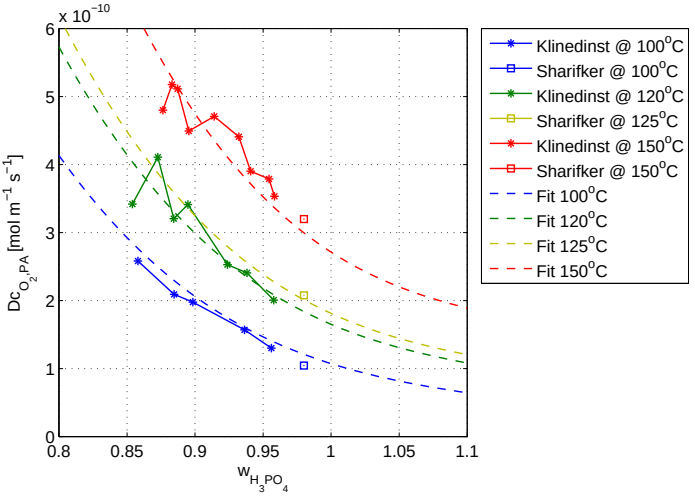

Figure 4.11 – Oxygen diffusion coefficient-solubility product in PA. Fit compared to data. [101, 104].

The solubility fit is plotted in figure 4.9. The fit is constrained by the values for solubility of oxygen in pure water. Given this property and the amount of scatter in the data points, the relation seems to capture at least the general trend of the solubility fairly well. The RMS deviation of the fit is 16.7% of the span of the data. Increasing the expression complexity to improve the fit is deemed

infeasible in light of the limited data.

The fit to the diffusion coefficient is shown in figure 4.10. This fit is better than for the solubility. The fits for 150 °C and 120 °C lie within the the variation of the data points. For 100 °C, the fit over predicts the value slightly but the two data points from Gubbins and Walker [102] agree well with the fits, even though they have not been considered by the fitting algorithm. The RMS deviation of the fit is 14.5% of the span of the data.

The fit to $Dc_{O_2,PA}$ is shown in 4.11. The agreement is close for the Klinedinst et al. [101] data with a RMS deviation of 8.17%. The correspondence with the Scharifker et al. [104] data is also acceptable.

4.3.3 Reaction kinetics

The cathode reaction kinetics are modelled using the Butler-Volmer equation which is given in its general form in (4.24) [7].

$$j = j_0 \left(\frac{c_R}{c_{R,ref}} \exp\left(\frac{\alpha n F}{RT} \eta \right) - \frac{c_P}{c_{P,ref}} \exp\left(\frac{(1-\alpha) n F}{RT} \eta \right) \right) \tag{4.24}$$

Here j and j_0 $\left[\mathrm{A\,m^{-2}}\right]$ are the current density and exchange current density per platinum surface area, respectively. c $\left[\mathrm{mol\,m^{-3}}\right]$ denotes concentration and subscripts P and R denote products and reactants, respectively. Subscript ref denotes the reference value as opposed to the actual value at the catalyst. α is the transfer coefficient and n is the number of electrons taking part in the reaction.

For the purpose of the present study, the above formulation of the Butler-Volmer equation is modified as follows: The exchange current density is converted to a limiting reduction rate constant k_{limit} $\left[\mathrm{mol\,m^{-2}\,s^{-1}}\right]$ as in (4.25). This rate constant is the same for the rate limiting step in all the reaction mechanisms considered. In this way, the steady state reaction rates are identical, regardless of the reaction mechanism applied. This means, that the intermediate steps in the reaction mechanism will only have an impact on the impedance spectrum. The reaction mechanisms, which have been investigated, are outlined in the following sections.

$$k_{limit} = \frac{j_0}{4F} \tag{4.25}$$

One step mechanism

The simplest way to model the cathode reaction of an HTPEM fuel cell is as a one step reaction, where oxygen reacts with protons and electrons to form water ($4\,H^+ + 4\,e^- + O_2 \rightleftharpoons 2\,H_2O$). The appropriate Butler-Volmer equation for the one step mechanism is given below. The water activity is not included in the reverse step, since it is taken into account in the calculation of the open circuit voltage (see section 4.3.5).

$$r_{\mathrm{O}_2} = k_{\text{limit}} \left(\frac{c_{\mathrm{O}_2}}{c_{\mathrm{O}_2,\text{ref}}} \exp\left(\frac{\alpha 4F}{RT}\eta \right) - \exp\left(\frac{(1-\alpha)4F}{RT}\eta \right) \right) \tag{4.26}$$

Here r_{O_2} is the conversion rate of O_2 per platinum surface area. The reference concentrations are taken as the local equilibrium concentration in the catalyst layer electrolyte phase, assuming 1 atm partial pressure of the species in question. Thus, $c_{\mathrm{O}_2,\text{ref}}$ is equal to the solubility of oxygen in PA as calculated by (4.23).

Three step mechanism

This mechanism was applied by Antoine et al. [108] and Bultel et al. [77] to develop an impedance model for Nafion based PEM fuel cells. The reaction mechanism was originally proposed by Damjanovic and Brusic [109]. The mechanism consists of a rate determining electrochemical step, in which O_2 reacts with H^+ and e^- to form $\mathrm{O_2H}$. The following step is a chemical one, in which $\mathrm{O_2H}$ reacts with water to form OH. In the final electrochemical step, OH reacts with H^+ and e^- to form water. The reactions are listed below.

$$\begin{aligned} \mathrm{O_2} + \mathrm{H}^+ + \mathrm{e}^- &\rightleftharpoons \mathrm{O_2H} \\ \mathrm{O_2H} + \mathrm{H_2O} &\rightleftharpoons 3\mathrm{OH} \\ \mathrm{OH} + \mathrm{H}^+ + \mathrm{e}^- &\rightleftharpoons \mathrm{H_2O} \end{aligned} \tag{4.27}$$

The relevant rate equations are given in (4.28). The intermediates are assumed to stick to the catalyst surface. Thus, the intermediate concentrations are taken with respect to the catalyst area. The reference concentrations for intermediates are taken as the surface concentration assuming the whole catalyst surface is covered by a monolayer of the intermediate. The reference concentration is calculated using (4.29). Here N_A is Avogadro's number and A_{int} $\left[\mathrm{m}^2\right]$ is the cross sectional area of an adsorbed reactant molecule. Since no values for $\mathrm{O_2H}$ and OH have been found, the value for water is used [110].

$$\begin{aligned} r_{\mathrm{O}_2} &= k_{\text{limit}} \left(\frac{c_{\mathrm{O}_2}}{c_{\mathrm{O}_2,\text{ref}}} \exp\left(\frac{\alpha_{\mathrm{O}_2} F}{RT}\eta \right) - \frac{c_{\mathrm{O_2H}}}{c_{\text{ref,int}}} \exp\left(\frac{(1-\alpha_{\mathrm{O}_2})F}{RT}\eta \right) \right) \\ r_{\mathrm{O_2H}} &= k_{\mathrm{O_2H}} \frac{c_{\mathrm{O_2H}}}{c_{\text{ref,int}}} - k_{\mathrm{OH}} \frac{c_{\mathrm{OH}}}{c_{\text{ref,int}}} \\ r_{\mathrm{OH}} &= k_{\mathrm{OH}} \left(\frac{c_{\mathrm{OH}}}{c_{\text{ref,int}}} \exp\left(\frac{\alpha_{\mathrm{OH}} F}{RT}\eta \right) - \exp\left(\frac{(1-\alpha_{\mathrm{OH}})F}{RT}\eta \right) \right) \end{aligned} \tag{4.28}$$

$$\begin{aligned} c_{\text{ref,int}} &= \frac{1}{A_{\text{int}} N_\mathrm{A}} = \frac{1}{12.5 \cdot 10^{-20}\,\mathrm{m}^2 \cdot 6.02214 \cdot 10^{23}\,\mathrm{mol}^{-1}} \\ &= 1.3284 \cdot 10^{-5} \mathrm{mol\,m^{-2}} \end{aligned} \tag{4.29}$$

Two step mechanism

The two step mechanism is a different interpretation of the Damjanovic mechanism used by Roy et al. [80]. Here, the rate determining electrochemical step is assumed to produce H_2O_2 which is converted to H_2O in a subsequent electrochemical step. The mechanism and relevant rate equations are listed below.

$$\begin{aligned} O_2 + 2H^+ + 2e^- &\rightleftharpoons H_2O_2 \\ H_2O_2 + 2H^+ + 2e^- &\rightleftharpoons 2H_2O \end{aligned} \tag{4.30}$$

$$\begin{aligned} r_{O_2} &= k_{\text{limit}} \left(\frac{c_{O_2}}{c_{O_2,\text{ref}}} \exp\left(\frac{\alpha_{O_2} 2F}{RT} \eta \right) - \frac{c_{H_2O_2}}{c_{\text{ref,int}}} \exp\left(\frac{(1-\alpha_{O_2})2F}{RT} \eta \right) \right) \\ r_{OH} &= k_{H_2O_2} \left(\frac{c_{H_2O_2}}{c_{\text{ref,int}}} \exp\left(\frac{\alpha_{H_2O_2} 2F}{RT} \eta \right) - \exp\left(\frac{(1-\alpha_{H_2O_2})2F}{RT} \eta \right) \right) \end{aligned} \tag{4.31}$$

4.3.4 Exchange current density

Measured values of the exchange current density of oxygen reduction on carbon supported Pt catalysts in PA and PA-PBI systems have been published on several occasions [103, 104, 111–115]. Kunz and Gruver [112] published a large number of measured values of the exchange current density per cm^2 Pt $\left(i_{0,\text{Pt}} \left[\text{A cm}_{\text{Pt}}^{-2}\right]\right)$in PA at different PA concentrations and temperatures. The exchange current density increases with increasing temperature and decreases with increasing PA concentration. The expression used for fitting the exchange current density is given in (4.32). The expression consists of a pre-exponential factor, which is linearly proportional to the P_2O_5 mole fraction, and an exponent that is inversely proportional to the acid concentration and linearly proportional to the temperature. The fitting was accomplished using the MATLAB® Curve fitting toolbox.

$$i_{0,\text{Pt}} = \left(a_0 + a_1 y_{P_2O_5}\right) \cdot \exp\left(b_0 + \frac{b_1}{y_{P_2O_5}} \cdot \frac{T - 373.15}{373.15} \right) \tag{4.32}$$

Coefficient	$x = 0$	$x = 1$
a_x	$6.84622680182766 \cdot 10^{-5}$	$-2.29098564381625 \cdot 10^{-4}$
b_x	7.96497447357910	2.12031438007528

Table 4.4 – Fitting coefficients for (4.32).

The resulting fit is plotted together with data from several sources [104, 112–114] in figure 4.12. The data points are coloured to reflect the acid concentration. As can be seen from the figure, there is a reasonable agreement between the colour of the Kunz and Gruver [112] data points and the fitted lines that pass through the point clusters. The agreement of the fit with the Appleby [114] data is acceptable,

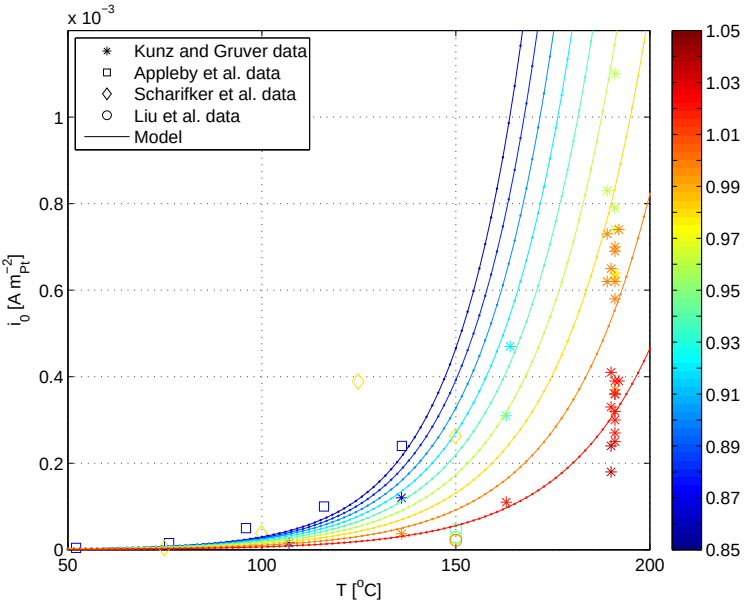

Figure 4.12 – Exchange current density per Pt area plotted as a function of temperature. The colour bar denotes the acid concentration in H_3PO_4 mass fraction. Fit compared to data [104, 112–114].

whereas the values presented by Scharifker et al. [104] are much higher and the data points from Liu et al. [113] measured in a PA-PBI system are much lower. The Liu et al. [113] data points do, however, suggest a similar dependence on acid concentration. Also, Mamlouk and Scott [115] presented values for exchange current densities on carbon supported platinum in a PA-PBI system at 100 °C and different acid loadings, that were one order of magnitude larger than the Scharifker et al. [104] data point at the same temperature. They were also one to two order of magnitude larger than values at similar acid doping levels from Liu et al. [113]. The acid concentration was not reported by Mamlouk and Scott [115], but the differences illustrate the degree of disagreement in the literature. Other sources do not report the exchange current density per platinum area which makes comparison difficult.

In spite of the disagreement with some sources, the fit produced is deemed suitable for use in the fuel cell model since any offset in the prediction of the exchange current density can be countered by adjusting the apparent Pt surface area accordingly. The exchange current density is usually only modelled as a function of temperature [50, 53, 56, 57, 116] or even as a constant [54, 83]. Cheddie and Munroe [55] and Siegel et al. [60] both took into account the effect of PA doping level in the CL PA-PBI system, but the effect of acid concentration was

neglected.

Considering the detail levels usually employed in HTPEM fuel cell models and the degree of disagreement between different sources, the expression in (4.32) is sufficiently detailed for the purpose of this modelling study. Also, the effect of acid loading on the catalyst activity is indirectly taken into account by the effect of free acid on the diffusion coefficient.

Catalyst area and Tafel slope

The exchange current density of Kunz and Gruver [112] was calculated by fitting the Tafel equation to electrode polarisation data. The Tafel slope used when fitting was 2.3RT/F. This translates to a Butler-Volmer equation with $\alpha n = 1$ for the reaction $O_2 + 4H^+ + 4e^- \rightleftharpoons 2H_2O$. The catalyst surface area of the electrodes used in the study were in the area of $60\,m^2\,g_{Pt}^{-1}$ for most electrodes.

When applying this data to a fuel cell model, it should be noted, that the performance of the electrodes used for obtaining the exchange current density data was significantly better than that of a real fuel cell. An earlier work by the same authors presented an electrode with $0.25\,mg_{Pt}\,cm^{-2}$ in $96w\%$ H_3PO_4 that exhibited a voltage of 0.6 V under air operation and 0.7 V under pure oxygen at $1A\,cm^{-2}$ [111]. For comparison, a BASF Celtec P1000 MEA with a cathode loading of $0.75\,mg_{Pt}\,cm^{-2}$ demonstrated a similar IR corrected performance under pure oxygen and a similar Tafel slope. The performance under air operation was worse due to concentration losses [39]. This would suggest that the effective surface area of the catalyst in a P1000 MEA is around $20\,m^2\,g_{Pt}^{-1}$. Generally, the mass specific catalyst surface area will have to be fitted to the individual fuel cells. ESA values from different fuel cell electrodes presented in the literature are given in table 4.5. As can be seen from the table, the assumption of around $20\,m^2\,g_{Pt}^{-1}$ for the Celtec P1000 cathode seems reasonable.

Source	ESA $\left[m^2\,g_{Pt}^{-1}\right]$	Comments
Kunz and Gruver [112]	45 - 69	PTFE bonded electrodes. Surface area determined by microscopy or by measuring hydrogen adsorption.
Mamlouk and Scott [115]	~ 35, ~16, ~14	Electrodes with acid doped PBI as binder. 20%, 40% and 60% Pt/C catalysts. Measured using cyclic voltametry (CV).
Zhai et al. [117]	17.2, 7.8	PBI bonded electrodes with 40% Pt/C. Before and after 300 h degradation test. Measured using CV.
Kwon et al. [118]	12-24	Measured using CV. Depending on measurement conditions.
Lobato et al. [75]	41-51	Measured using CV. Varied with CL PBI content. PBI bonded electrodes with 2/3 Pt/C catalyst.

Table 4.5 – ESAs from various sources.

Using the measured polarisation data it can be investigated whether the assumption of $\alpha n = 1$ is valid for the investigated fuel cell. Using the Tafel equation

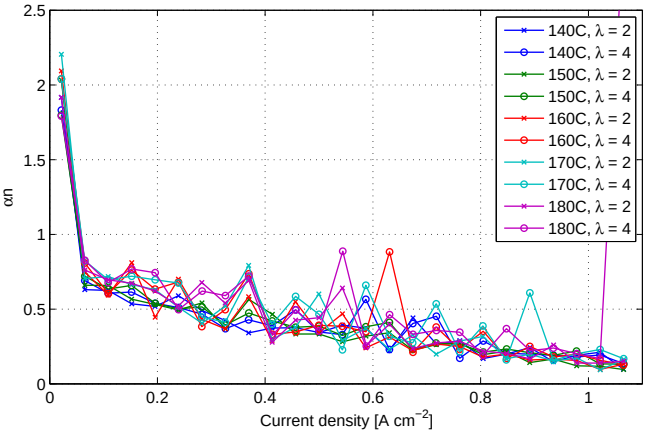

Figure 4.13 – Apparent αn values along the polarisation curve at different temperatures.

and neglecting effects of reactant concentration, the activation overpotential can be expressed as

$$\eta = \frac{RT}{\alpha n F} \ln\left(\frac{i}{i_0}\right) \tag{4.33}$$

In a case where activation is the only relevant loss mechanism, the above equation is valid between any two points on the polarisation curve. The rewritten Tafel equation becomes:

$$V_1 - V_2 = \frac{RT}{\alpha n F} \ln\left(\frac{i_2}{i_1}\right) \tag{4.34}$$

Rearranging to get an expression for αn:

$$\alpha n = \frac{RT}{(V_1 - V_2)\, F} \ln\left(\frac{i_2}{i_1}\right) \tag{4.35}$$

Applying (4.35) between every load step of the IR corrected Dapozol® 77 polarisation curves a pattern emerges. The first step in the polarisation curve yields αn values around 2 for all polarisation curves. All subsequent steps yield values lower than 1. A plot of the calculated local αn values are given in figure 4.13. The fact that the apparent value of αn is 2 at low polarisation could mean one of two things. Either, it is a result of the Tafel equation not being valid close to the exchange current density as was argued by Kunz and Gruver [111]. In that case, the most appropriate value for αn is probably less than 1, since this is the value that is obtained in most of the range. On the other hand, it could be, that $\alpha n = 2$ is indeed the right value, and the lower values obtained when polarising the electrode is a result of losses. In different HTPEM models different values of

αn have been used, ranging from 0.2 [83] over 0.73 [50, 116], 0.8 [49], 0.89 [60], and 1 [56, 57] to 2 [54, 55, 58, 59]. This variety of values used for this very important parameter suggests that investigating values other than $\alpha n = 1$ is worthwhile. For the model fitting, cases using other values will also be investigated.

Since the exchange current density calculated by (4.32) is derived using $\alpha n = 1$, i_0 will have to be corrected when using other values to avoid unreasonable ESA values. Since αn controls the Tafel slope, the correction consists of changing the voltage at which the curves with different αn intersect. If the point of intersection is at current density i, it can be shown that the exchange current density correction factor f_{corr} can be calculated as:

$$f_{\text{corr}} = \left(\frac{i_0}{i}\right)^{\alpha_2/\alpha_1 - 1} \tag{4.36}$$

When applying the correction, information from the data by Kunz and Gruver [112] as well as from the Dapozol® 77 polarisation curves is used. The current of intersection is taken as $0.1\,\text{A}\,\text{cm}^{-2}$, since the transition from the activation region to the ohmic region seems to take place around this point for the tested Dapozol® 77 MEA (see figure 3.14). The calculation in (4.36) is made for each value of i_0 in [112]. Taking the median value of $\frac{i_0}{i}$ for all the points yields $9.55 \cdot 10^{-5}$.

Reaction order

Another parameter that influences the reaction kinetics is the reaction order with respect to the oxygen concentration. Using the Tafel equation, the concentration dependent activation overpotential can be expressed as

$$\eta = \frac{RT}{\alpha n F} \ln\left(\left(\frac{c_{\text{O2}}}{c_{\text{O2,0}}}\right)^{\gamma} \cdot \frac{i}{i_0}\right) \tag{4.37}$$

where γ is the apparent reaction order. Assuming that a polarisation curve can be recorded without diffusion limitations, the difference in η between a curve using pure O_2 and a curve using air with 21% O_2 becomes

$$\begin{aligned}
\Delta\eta = \eta_{\text{air}} - \eta_{\text{O}_2} &= \frac{RT}{\alpha n F}\ln\left(\left(\frac{c_{\text{O2,air}}}{c_{\text{O2,0}}}\right)^{\gamma} \cdot \frac{i}{i_0}\right) - \frac{RT}{\alpha n F}\ln\left(\left(\frac{c_{\text{O2,0}}}{c_{\text{O2,0}}}\right)^{\gamma} \cdot \frac{i}{i_0}\right) \\
&= \frac{RT}{\alpha n F}\left(\ln\left(\left(\frac{c_{\text{O2,air}}}{c_{\text{O2,0}}}\right)^{\gamma} \cdot \frac{i}{i_0}\right) - \ln\left(\left(\frac{c_{\text{O2,0}}}{c_{\text{O2,0}}}\right)^{\gamma} \cdot \frac{i}{i_0}\right)\right) \\
&= \frac{RT}{\alpha n F}\ln\left(\left(\frac{c_{\text{O2,air}}}{c_{\text{O2,0}}}\right)\right)\gamma
\end{aligned} \tag{4.38}$$

Rearranging and applying the assumption that c_{O_2} is linearly proportional to the O_2 mole fraction, the reaction order can be expressed as

$$\gamma = \frac{\alpha n F}{RT \ln(0.21)} \Delta\eta \tag{4.39}$$

To estimate γ, the voltage difference between air and pure oxygen operation for a $0.25\,\mathrm{mg\,cm^{-2}}$ half cell presented by Kunz and Gruver [111] is used. At $T = 433\mathrm{K}$ and $\alpha n = 1$, $\Delta\eta$ is around -0.064 V and -0.071 V at $4\,\mathrm{mA\,cm^{-2}}$ and $300\,\mathrm{mA\,cm^{-2}}$ respectively. This translates to a reaction order between 1.1 and 1.2. Using $\alpha n = 2$, the reaction order is twice as high. However, if $\Delta\eta$ is taken below $1\,\mathrm{mA\,cm^{-2}}$, the value reduces to -0.034 V. This gives $\gamma \approx 1.2$. If $\alpha n = 0.75$ is used, however, the apparent reaction order is around 0.85.

Most sources investigating γ in PA report a reaction order of around 1 [103, 113, 119]. Even so, Mamlouk and Scott [115] observed reaction orders as low as 0.55 at 100 °C. The reaction order, however, increased to 1 at 140 °C. Schmidt and Baurmeister [38] reported a reaction order of 0.6 for Celtec P-1000 MEAs.

The γ value for the DPS MEA characterised for use with the model (see section 3.4 on page 29) can also be estimated. As with the Kunz and Gruver [111] data, polarisation curves recorded at 160 °C are used. The $\Delta\eta$ is estimated by the average voltage difference in the current density range 0.2 to $0.6\,\mathrm{A\,cm^{-2}}$ between the polarisation curves recorded at oxygen stoichiometry of 2 and 4 respectively. This gives $\Delta\eta = 0.0042\,\mathrm{V}$. The average mole fraction of oxygen inside the fuel cell at a given stoichiometry can be estimated by taking the average of the inlet and outlet mole fractions:

$$\begin{aligned} y_{\mathrm{O_2,avr}} &= \frac{1}{2}\left(y_{\mathrm{O_2,in}} + y_{\mathrm{O_2,out}}\right) = \frac{1}{2}\left(y_{\mathrm{O_2,in}} + \frac{\dot{n}_{\mathrm{O_2,out}}}{\dot{n}_{\mathrm{out}}}\right) \\ &= \frac{1}{2}\left(y_{\mathrm{O_2,in}} + \frac{I(\lambda_{\mathrm{O_2}} - 1)/\left(4F\right)}{I(\lambda_{\mathrm{O_2}} + 1)/\left(4F y_{\mathrm{O_2,in}}\right)}\right) \\ &= \frac{y_{\mathrm{O_2,in}}}{2}\left(1 + \frac{(\lambda_{\mathrm{O_2}} - 1)}{(\lambda_{\mathrm{O_2}} + 1)}\right) \end{aligned} \tag{4.40}$$

Assuming that O2 concentration at the catalyst depends only on mean mole fraction and that all other parameters are equal, (4.38) is applied for $\lambda_{\mathrm{O_2}}$ of 2 and 4:

$$\begin{aligned} \Delta\eta &= \frac{RT}{\alpha n F}\ln\left(\frac{\frac{y_{\mathrm{O_2,in}}}{2}\left(1 + \frac{(4-1)}{(4+1)}\right)}{\frac{y_{\mathrm{O_2,in}}}{2}\left(1 + \frac{(2-1)}{(2+1)}\right)}\right)\gamma \\ &= \frac{RT}{\alpha n F}\ln\left(\frac{\left(1 + \frac{(4-1)}{(4+1)}\right)}{\left(1 + \frac{(2-1)}{(2+1)}\right)}\right)\gamma \\ &= \frac{RT}{\alpha n F}\ln\left(\frac{6}{5}\right)\gamma \end{aligned} \tag{4.41}$$

Rearranging now gives

$$\gamma = \frac{\alpha n F}{RT\ln\left(6/5\right)}\Delta\eta = 0.62 \tag{4.42}$$

This value is subject to some uncertainty. The assumption of a linear relation between stoichiometry and local oxygen concentration is not entirely valid, since diffusion limitations will be more severe at lower stoichiometry. This suggests that the actual γ may be smaller. On the other hand, lower stoichiometry may mean higher local water concentration, which increases conductivity and improves performance to counteract the effects of the lower oxygen concentration. If other values of αn are used, this also affects the result of 4.42. For $\alpha n = 2$, $\gamma = 1.24$, while for $\alpha n = 0.75$, $\gamma = 0.465$, At any rate, cases using different values of γ should be investigated, when fitting the model.

4.3.5 Open circuit voltage

The reference state for calculating the open circuit voltage of the fuel cell is calculated using the Engineering Equation Solver software package. Reactants and products are assumed in gas form at $p_0 = 1\,\text{atm}$ and the temperature is $T_0 = 433.15\,\text{K}$. This gives a reference reversible cell potential of $E_0 = 1.152\,\text{V}$. The open circuit voltage of the fuel cell is calculated using the Nernst equation as in (4.43).

$$\begin{aligned} E =& E_0 + \frac{\Delta s\,(T - T_0)}{2F} - \frac{RT}{2F} \ln\left(\frac{a_{\text{H}_2\text{O}}}{a_{\text{H}_2} a_{\text{O}_2}^{1/2}}\right) \\ =& 1.152\,\text{V} + \frac{48.1\,\text{J}\,(\text{mol}\,\text{K})^{-1}\,(T - T_0)}{2F} - \frac{RT}{2F} \ln\left(\frac{a_{\text{H}_2\text{O}}}{a_{\text{H}_2} a_{\text{O}_2}^{1/2}}\right) \end{aligned} \tag{4.43}$$

The activity $a_{\text{H}_2\text{O}}$ is calculated as the ratio of the local H_2O partial pressure and p_0. The oxygen concentration dependence is handled by the Butler-Volmer equation, so $a_{\text{O}_2} = 1$. Since the anode side is disregarded, it is assumed that $a_{\text{H}_2} = 1$.

The temperature dependent term results in a voltage loss of 20 mV between 110 °C and 190 °C. The concentration dependent term is more involved. Since HTPEM fuel cells are usually operated at close to dry conditions, the water activity correction will tend to increase the OCV.

4.3.6 Conductivity

Ionic and electronic conductivity of different parts of the fuel cell play an important part in the performance. The main ohmic loss is usually assumed to derive from proton conduction in the electrolyte membrane, but losses due to contact resistances and electronic conduction in GDL and bipolar plates should not be neglected. The individual conductivities and resistances are considered as stated below.

Catalyst layer ionic conductivity

The catalysts layer ionic conductivity is calculated by correcting the conductivity of phosphoric acid for the volume fraction ϵ_{PA} and tortuosity using the Bruggeman correction.

$$\kappa_{\mathrm{CL}} = \kappa_{\mathrm{PA}} \cdot \epsilon_{\mathrm{PA}}^{1.5}$$

The conductivity of PA as a function of temperature T_{C} [°C] and H_3PO_4 mass fraction $w_{H_3PO_4}$ was expressed by MacDonald and Boyack [100] as a piecewise continuous function. Their relation is given in (4.44) and (4.45) with coefficients modified to give κ_{PA} in $\mathrm{S\,m^{-1}}$. Between a H_3PO_4 mass fraction of 0.94 and 0.96, linear interpolation is applied.

For $0.84 < w_{H_3PO_4} < 0.94$:

$$\begin{aligned}\kappa_{\mathrm{PA}} = &\left(101.365 - 121.548 \cdot w_{H_3PO_4}\right) \\ &- T_{\mathrm{C}} \cdot \left(1.5447 \cdot 10^{-1} - 6.42463 \cdot 10^{-1} \cdot w_{H_3PO_4}\right)\end{aligned} \tag{4.44}$$

For $0.96 < w_{H_3PO_4} < 0.99$:

$$\begin{aligned}\kappa_{\mathrm{PA}} = &-345.285 + 777.294 \cdot w_{H_3PO_4} - 450.762 \cdot w_{H_3PO_4}^2 \\ &- T_{\mathrm{C}} \cdot \left(6.24637 - 13.87186 \cdot w_{H_3PO_4} + 7.18336 \cdot w_{H_3PO_4}^2\right)\end{aligned} \tag{4.45}$$

Membrane conductivity

The conductivity of the electrolyte membrane is a function of acid doping level, humidity and temperature as well as the type of PBI used and the manufacturing process [25, 120, 121]. In a recent paper by Kazdal et al. [51], a relation depending only on amorphous PA volume fraction ($\epsilon_{\mathrm{PA,am}}$) and the conductivity of free PA was proposed. This philosophy was also used in this work. A relation was generated by fitting to data from Ma [122]. The main difference between the relation in this work and the one in Kazdal et al. [51] is the addition of a fitting exponent to the PA conductivity. The resulting relation is given in (4.46).

$$\kappa_{\mathrm{MEM}} = 0.02 \cdot \kappa_{\mathrm{PA}}^{1.693} \cdot \epsilon_{\mathrm{PA,am}}^{1.683} \tag{4.46}$$

Here the amorphous PA volume fraction is calculated using (4.47).

$$\epsilon_{\mathrm{PA,am}} = \frac{(X-2)\,(M_{\mathrm{PA}}/\rho_{\mathrm{PA}})}{X\,(M_{\mathrm{PA}}/\rho_{\mathrm{PA}}) + (M_{\mathrm{PBI}}/\rho_{\mathrm{PBI}})} \tag{4.47}$$

The doping level X is the number of H_3PO_4 molecules per PBI repeat unit. $M_{\mathrm{PA}} = 0.098\,\mathrm{kg/mol}$ and $M_{\mathrm{PBI}} = 0.308\,\mathrm{kg/mol}$ are the molar masses of H_3PO_4 and PBI respectively. The density of PBI is assumed constant ($\rho_{\mathrm{PBI}} = 1300\,\mathrm{kg/m^3}$), while the density of PA is calculated using (4.18).

GDL conductivity

The resistance of the GDLs are also taken into account. Where applicable, the data sheet value is used. When the GDL conductivity is unknown, an estimate is made using a modified Bruggeman correction as given in (4.48) [123]. Here the electronic conductivity of the carbon fibres is $\sigma_{\mathrm{C}} = 10^5\,\mathrm{S\,m^{-1}}$.

$$\sigma_{\mathrm{GDL}} = \sigma_{\mathrm{C}} \left(1 - \epsilon_{\mathrm{GDL}}\right)^{3.4} \tag{4.48}$$

This expression was shown to apply well to the through-plane conductivity of carbon paper GDLs. The same expression is assumed to be valid for woven GDLs.

Cell assembly resistances

Even accounting for the above phenomena, the model still fails to reproduce the appropriate total resistance to allow fitting of impedance spectra. To remedy this, an extra resistance $\left(R_{\mathrm{ct}}\ \left[\Omega\,\mathrm{m^2}\right]\right)$ is introduced. This resistance represents resistive losses in the fuel cell assembly. These are assumed to stem mainly from contact resistance between the individual cell components. This value can be varied by the fitting algorithm to improve the model fit.

4.3.7 Diffusivities

When determining the diffusivity in the porous media two phenomena are taken into account. These include continuum multi component diffusion considering interaction of the diffusing species and Knudsen diffusion considering interactions with the pore walls. Knudsen diffusion is only considered in the CL, since the GDL pores are assumed too large for wall interactions to be significant.

The mixture diffusivity of species i is calculated from the binary diffusivities of i with respect to the other species j using

$$D_{i,\mathrm{mix}} = \frac{1 - y_i}{\sum \left(y_j / D_{ij}\right)} \tag{4.49}$$

The binary diffusivities $\left(D_{ij}\ \left[\mathrm{m^2\,s^{-1}}\right]\right)$ are corrected for temperature and pressure.

$$D_{ij} = D_{ij,0} \frac{P_0}{P} \left(\frac{T}{T_0}\right)^{\gamma} \tag{4.50}$$

Here subscript 0 denotes the reference state and γ is a species specific exponent. The reference values are given in table 4.6.

The Knudsen diffusivity of species i is calculated using the formulation given in Bird et al. [125]:

$$D_{i,\mathrm{K}} = \frac{8r}{3} \sqrt{\frac{RT}{2\pi M_i}} \tag{4.51}$$

Gas pair	D_{ij} $\left[\mathrm{m^2\,s^{-1}}\right]$	T_0 [K]	γ
O_2 - N_2	$2.02 \cdot 10^{-5}$	293.15	1.728
O_2 - H_2O	$2.44 \cdot 10^{-5}$	293.15	1.967
N_2 - H_2O	$2.42 \cdot 10^{-5}$	293.15	2.073

Table 4.6 – Reference values for binary diffusivities [124]

where r [m] is the mean pore radius. The pore radius is estimated by assuming that the catalyst layer consists of identical cylindrical pores. The radius is then given by the ratio of the void volume $\left(V_{\mathrm{pore}}\ \left[\mathrm{m^3}\right]\right)$ over the total CL wall surface area, which is assumed equal to the surface area of the carbon backing $\left(A_{\mathrm{C}}\ \left[\mathrm{m^2}\right]\right)$.

$$r = 2\frac{V_{\mathrm{pore}}}{A_{\mathrm{C}}} \tag{4.52}$$

The bulk diffusion coefficient is calculated by taking the inverse of the sum of diffusion resistances.

$$D_{i,\mathrm{bulk}} = \frac{1}{1/D_{i,\mathrm{K}} + 1/D_{i,\mathrm{mix}}} \tag{4.53}$$

For the GDL, $D_{i,\mathrm{bulk}} = D_{i,\mathrm{mix}}$. The bulk diffusivity is corrected for porosity and tortuosity using the relation of (4.54) given by Zamel et al. [126].

$$D_{i,\mathrm{eff}} = 1.01\,(\epsilon - 0.24)^{1.83}\,D_{i,\mathrm{bulk}} \tag{4.54}$$

Since (4.54) is only valid in the GDL, the Bruggeman correlation is used to correct for porosity and tortuosity in the CL:

$$D_{i,\mathrm{eff}} = \epsilon^{1.5} D_{i,\mathrm{bulk}} \tag{4.55}$$

4.4 Summary

This chapter has treated the 1+1D HTPEM fuel cell model developed in the course of this project. The model solves the governing equations for overpotential and reactants in the gas phase as well as in the electrolyte phase. The electrode processes are modelled assuming either 1-, 2-, or 3-step kinetics. The model can be solved in both steady state and dynamic mode to generate both polarisation curves and impedance spectra. Emphasis is on modelling the influence of the acid concentration on the cell performance. New relations have been developed for solubility and diffusivity of O_2 in PA by combining data from several sources. The effect of PA concentration on the exchange current density is also accounted for. The modelling of the influence of the PA concentration in the catalysts layer is more advanced than what is generally employed in HTPEM fuel cell modelling.

Chapter 5

Simulations

Having established the modelling framework, the model can now be applied to a data set. The focus of the work presented in this section is to fit the model to recorded data assuming different fixed parameter values.

The first section deals with the specification of known model parameters. The second part concerns the selection of the strategy for fitting the model and the grid independence of the solution. The third part presents the fitting cases and the results of the model fitting. The final sections concern various studies of the effects of the gas dynamics and the operating temperature on the simulation results. The shortcomings of the model are discussed, and the the improvements which are deemed necessary to achieve the initial ambitions for the model are accounted for.

5.1 Model parameters

The parameters used when running the model can be divided into two categories. The fixed parameters are those which can be established from data sheets, are supplied by the the MEA manufacturer, or can be found in the literature. The fitting parameters are the ones that are either completely unknown or where the uncertainty is deemed sufficiently large to have an important impact on the result. The model is fitted to impedance spectra and polarisation curves from a Dapozol® 77 MEA. Most of the relevant data for the MEA has been supplied by the manufacturer. The known and assumed parameter values of the Dapozol® 77 are given in table 5.1.

Parameter	Symbol	Value	Comment
CL thickness	t_{CL}	25 µm	Value supplied by DPS.
Membrane thickness	t_{MEM}	80 µm	Value supplied by DPS.
GDL thickness	t_{GDL}	260 µm	Measured on GDL
GDL resistance	R_{GDL}	$10^{-2}\,\Omega\mathrm{cm}^2$	[96]
GDL porosity	ϵ_{GDL}	0.78	See section 3.6.2
Permeability	k_{p}	$10^{-14}\mathrm{m}^2$	[96]. Converted from Air Resistance (Gurley) according to ISO 5636-5:2013(E) [127]. Assumed equal for GDL and CL.
Pt Loading	L_{Pt}	$1.6\,\mathrm{mg\,cm}^{-2}$	Value supplied by DPS.
Pt/C ratio in CL	$r_{\mathrm{Pt/C}}$	0.6	Value supplied by DPS.
PBI/C ratio in CL	$r_{\mathrm{PBI/C}}$	-	Proprietary information. Value supplied by DPS.
O_2 step transfer coefficient	$\alpha n_{\mathrm{O_2}}$	1/1.25/0.75	Depending on the case.
O_2 step reaction order	$\gamma_{\mathrm{O_2}}$	1/1.2/0.6	Depending on the case.
Cell area	A_{FC}	$46\,\mathrm{cm}^2$	Value supplied by DPS.
Channel width	W_{CH}	1.2 mm	Measured on the cathode flow plate.
Channel height	H_{CH}	1 mm	Measured on the cathode flow plate.
Land width	W_{L}	1.2 mm	Measured on the cathode flow plate.
Humidifier temperature	T_{humid}	47 °C	Measured during data acquisition.

Table 5.1 – Fixed parameters of the Dapozol® 77 MEA and the flow field when fitting.

5.2 Fitting strategy

Several investigations are carried out in order to identify the capabilities and limitations of the model. In all cases, a set of unknown parameters are tweaked by a fitting algorithm to get the best possible correlation between the model and the data.

The data set used for fitting the model is chosen as a compromise between the need to generate a parameter set, which is able to faithfully reproduce the measurements across the operating range and the need for acceptable computational times. The chosen set consists of two polarisation curves and four impedance spectra. The operating temperature is 160 °C, the oxygen stoichiometry is varied between 2 and 4, and the impedance DC current is varied between 5 A and 20 A. This should ensure that the resulting parameter set takes into account the effect of varying oxygen concentration as well as the significant effect of the impedance DC current. The temperature is kept constant, since most of the relations used in the model already account for the effect of temperature.

The discretisation of the computational domain is kept as coarse as possible to minimise computational times. The channel has 20 cells, the GDL has 15 cells

and the CL has 25 cells. When running the simulations, the steady state solution is found at the currents corresponding to $n_{\text{pol}} = 12$ linearly spaced voltages on the reference polarisation curve. The impedance is simulated at $n_{\text{eis}} = 20$ logarithmically spaced frequencies between 1 kHz and 0.1 Hz. The model is solved in potentiostatic mode, imposing a sinusoidal voltage on the steady state value. The simulation is sustained for 10 periods and the current and voltage of the two final periods are fitted to phase shifted sine waves to calculate the impedance.

The steady state solutions are obtained with the MATLAB® fsolve function using the Trust-Region-Dogleg algorithm. The dynamic simulations are made using the ode15 function, which is suited for solution of stiff differential equations.

The objective function to be minimised aggregates the deviations of all simulated curves from their measured counterparts in one value as shown in (5.1). Here subscripts ref and sim refer to reference data and simulation results respectively.

$$\begin{aligned} f_{\min} = &\sum \left(\left(\frac{\left(V_{\text{ref}} - V_{\text{sim}}\right) / \text{std}\left(V_{\text{ref}}\right)}{n_{\text{pol}}} \right)^2 \right) + \\ &\sum \left(\left(\frac{\left|Z_{\text{ref}} - Z_{\text{sim}}\right| / \text{std}\left(\left|Z_{\text{ref}}\right|\right)}{n_{\text{eis}}} \right)^2 \right) \end{aligned} \tag{5.1}$$

The optimisation is carried out using the function fminsearchcon developed by John D'Errico, based on the build-in function fminsearch. The function performs optimisation based on the Nelder/Mead simplex method. When fitting the parameters, the algorithm is allowed to run overnight for at least 100 iterations. Optimisation is terminated when no change in the residuals within three significant digits are observed during at least 20 iterations. The PC used has an Intel® Core i7-2600 quad core CPU and 3.8 GB RAM. The OS is Ubuntu Linux 12.04 and the MATLAB® version is 2012b.

5.2.1 Grid independence

In order for the results of the fitting process to be reliable, the solution generated by the model must be independent of the discretisation used. In this section, this dependence is investigated. The objective function value is used to judge the grid independence of the solution. The model is solved using the parameters given in table 5.1 and the fitted values for fitting cases 1 and 7 (see the following section). The effect of varying the resolution of the individual domains by 20% are shown in table 5.2. As can be seen, the effect is negligible for case 7, while there is a slight grid dependence in case 1 with respect to CL and channel resolution. This is most likely related to the steep gradients within the CL in case 1 (see figure 5.2). Since the dependence when increasing the resolution by 20% is less than 1% in all cases, it is deemed infeasible to increase the resolution further to ensure a completely grid independent solution in case 1.

	Base	CL		GDL		Channel	
	resolution	+20%	-20%	+20%	-20%	+20%	-20%
Case 1	0.0568	0.0565	0.0581	0.0568	0.0568	0.0568	0.0572
Case 7	0.0302	0.0302	0.0302	0.0302	0.0302	0.0302	0.0302

Table 5.2 – Effect on objective function value ($f_{\min}$) when varying discretisation.

5.3 Model fitting

In this section, the model fitting cases are presented, and the results are discussed. The cases investigated are listed below.

1. One-step model. $\gamma_{O_2} = 1$, $\alpha n_{O_2} = 1$.
2. One-step model. $\gamma_{O_2} = 1.2$, $\alpha n_{O_2} = 1$. Reaction order as derived from the Kunz and Gruver [111] data (see section (4.3.4)).
3. One-step model. $\gamma_{O_2} = 0.6$, $\alpha n_{O_2} = 1$. Reaction order as derived from voltage difference due to stoichiometry change (see section (4.3.4)).
4. One-step model. $\gamma_{O_2} = 1$, $\alpha n_{O_2} = 1$. PA loading limited to give plausible high frequency behaviour.
5. One-step model. $\gamma_{O_2} = 1$, $\alpha n_{O_2} = 1$. Catalyst layer conductivity model is changed to give plausible high frequency behaviour.
6. One-step model. $\gamma_{O_2} = 1$, $\alpha n_{O_2} = 1.25$. Transfer coefficient increased to better match the low current density behaviour (see section 4.3.4).
7. One-step model. $\gamma_{O_2} = 1$, $\alpha n_{O_2} = 0.75$. Transfer coefficient lowered to match the behaviour in the rest of the current range (see section 4.3.4).
8. One-step model. γ_{O_2} and αn_{O_2} included in optimisation.
9. Two-step model. $\gamma_{O_2} = 1$, $\alpha n_{O_2} = 1$.
10. Three-step model. $\gamma_{O_2} = 1$, $\alpha n_{O_2} = 1$.

The fitting parameters are given in 5.3. These parameters are the ones deemed too uncertain for fixing. Also, they have a significant effect on the performance of the fuel cell. As can be seen from the table, the fitting algorithm converges to quite different parameter combinations depending on the case. The deviation of the individual simulated curves with respect to the data are listed in table 5.4.

Another relevant overview is given in figure 5.1. Here the resistance ratios, as described in 3.6.1, are plotted for the reference data and for each simulation run to enable comparison.

Parameter	Symbol [Unit]		Case # 1	2	3	4	5	6	7	8	9	10
O_2 step transfer coefficient	αn_{O_2}	Value	1.00	1.00	1.00	1.00	1.00	1.25	0.75	0.80	1	1
		Deviation	-	-	-	-	-	(+25%)	(-25%)	(-20%)	-	-
O_2 reaction order	γ_{O_2}	Value	1.00	1.20	0.60	1.00	1.00	1.00	1.00	1.48	1	1
		Deviation	-	(+20%)	(-40%)	-	-	-	-	(+48%)	-	-
Catalyst ESA	$A_{Pt,m}$ $\left[m^2\, g_{Pt}^{-1}\right]$	Value	46.5	63.5	24.2	34.5	40.1	45.9	47.5	100	29.2	25.4
		Deviation	-	(+37%)	(-48%)	(-26%)	(-14%)	(-1.2%)	(+2.2%)	(+115%)	(-37%)	(-45%)
Carbon surface area	$A_{C,m}$ $\left[m^2\, g^{-1}\right]$	Value	188	159	348	378	100	976	237	192	329	262
		Deviation	-	(-16%)	(+84%)	(+101%)	(-47%)	(+418%)	(+26%)	(+2.1%)	(+74%)	(+104%)
CL PA Loading	$L_{H_3PO_4}$ $\left[mg\, cm^{-2}\right]$	Value	0.929	0.928	0.872	0.450	0.773	0.686	0.410	0.400	0.373	0.295
		Deviation	-	(-0.12%)	(-6.1%)	(-52%)	(-17%)	(-26%)	(-56%)	(-57%)	(-60%)	(-60%)
Double layer capacitance	C_{dl} $\left[F\, m^{-2}\right]$	Value	79.7	78.4	82.5	110	125	88.1	109	104	121	139
		Deviation	-	(-1.6%)	(+3.6%)	(+38%)	(+57%)	(+11%)	(+37%)	(+31%)	(+52%)	(+74%)
Miscellaneous resistance	R_{misc} $\left[\Omega cm^2\right]$	Value	0.1084	0.1072	0.1100	0.1085	0.0993	0.1129	0.0989	0.0969	0.0993	0.0930
		Deviation	-	(-1.2%)	(+1.4%)	(+0.0%)	(-8.4%)	(+4.1%)	(-8.8%)	(-11%)	(-8.4%)	(-14%)
OH / H_2O_2 step transfer coefficient	αn_{OH}/ $\alpha n_{H_2O_2}$		-	-	-	-	-	-	-	-	0.351	0.343
OH / H_2O_2 step rate scaling factor	s_{OH} / $s_{H_2O_2}$		-	-	-	-	-	-	-	-	$7.50 \cdot 10^4$	$1.00 \cdot 10^7$
O_2H step forward rate scaling factor	$s_{O_2H,fw}$		-	-	-	-	-	-	-	-	-	$4.19 \cdot 10^7$
O_2H step backward rate scaling factor	$s_{O_2H,bw}$		-	-	-	-	-	-	-	-	-	$8.26 \cdot 10^{-2}$
Objective function value		Value	0.0568	0.0567	0.0485	0.0916	0.1040	0.0292	0.0302	0.0237	0.0256	0.0326
		Deviation	-	(-0.25%)	(-15%)	(+61%)	(+83%)	(-49%)	(-47%)	(-58%)	(-55%)	(-37%)

Table 5.3 – Fitting parameters of the Dapozol® 77 MEA.

Curve		IV		EIS			
λ		2	4	2	4	2	4
i_{DC}		-	-	0.11 A cm^{-2}	0.11 A cm^{-2}	0.43 A cm^{-2}	0.43 A cm^{-2}
Case #	1	1.60% / 2.48%	1.28% / 2.35%	3.04% / 6.38%	3.98% / 6.50 %	2.36% / 3.92%	4.36% / 6.85 %
	2	1.56% / 2.44%	1.18 % / 2.93 %	2.86% / 6.26%	4.19% / 6.89%	2.63% / 4.86%	4.57% / 6.75%
	3	1.61% / 2.43 %	1.36% / 2.36 %	2.80% / 5.33%	3.71% / 5.93%	2.02% / 2.95%	4.12% / 6.01%
	4	1.07% / 1.85%	1.08% / 1.46%	7.54% / 15.6%	8.44% / 15.3%	2.42% / 4.06%	1.94% / 2.74%
	5	2.05% / 3.76%	1.85% / 3.24%	7.69% / 15.9%	8.42% / 15.1%	2.68% / 5.05%	1.84% / 3.17%
	6	1.09% / 1.73%	0.94% / 2.17%	1.54% / 4.03%	3.07% / 5.58%	2.55% / 3.89%	3.00% / 4.14%
	7	2.14% / 5.22%	1.85% / 4.91%	1.74% / 3.22%	2.02% / 3.02%	2.12% / 4.09%	2.13% / 3.42%
	8	1.85% / 4.21%	1.43% / 3.93%	1.08% / 2.23%	2.21% / 3.85%	1.94% / 3.67%	2.10% / 3.51%
	9	0.75% / 1.44%	0.77% / 1.11%	2.26% / 5.63%	2.83% / 5.42%	3.22% / 5.88%	1.74% / 2.46%
	10	0.58% / 1.64%	0.69% / 1.48%	3.81% / 7.22%	2.98% / 6.65%	3.78% / 6.54%	2.06% / 3.54%

Table 5.4 – Deviation of the individual simulated curves from their measured counterparts for all fitting cases. Deviations are normalised by the span of the measured data. The first value for each entry is RMS deviation. The second value is maximum absolute deviation.

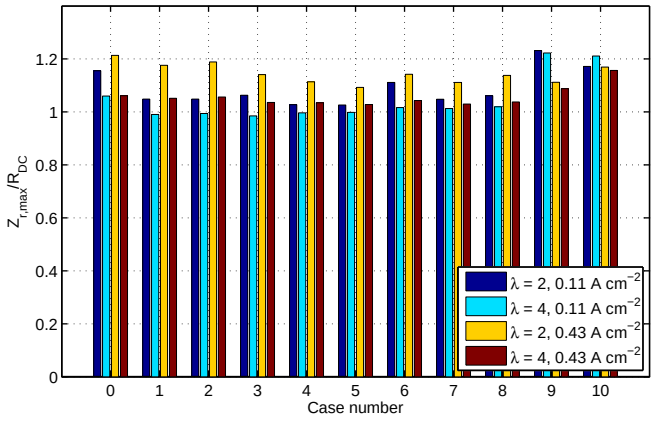

Figure 5.1 – Ratios of the the maximum real part of the impedance to polarisation curve slope at the same point. Values for all fitting cases. The case with number 0 contains the data values.

5.3.1 Case 1: $\gamma_{O_2} = 1$, $\alpha \mathbf{n}_{O_2} = 1$

Case 1 uses the one step model, assuming that the electrode reactions are first order with respect to oxygen concentration. The fitted polarisation curves and impedance spectra are given in figures 5.3 and 5.4 respectively. The fit to the polarisation curve has the largest fitting error for $\lambda = 2$, with an RMS error and a maximum error of 1.60% and 2.48% of the maximum voltage respectively. The impedance fit is less precise. Here the maximum relative error is at $\lambda = 4$ and $i_{DC} = 0.43 \mathrm{A\,cm^{-2}}$. The maximum error is 6.85% of the maximum absolute value of the measured impedance and the RMS error is 4.36%. Even though the errors are within what would be considered an acceptable range for normal engineering practice, the simulation results and the fitting parameters themselves indicate that the parameters, to which the model converges, do not accurately represent the actual fuel cell parameters.

The fitting parameters converge to a set of values, that deserve a few comments. The specific catalyst ESA is quite large at $46.5\,\mathrm{m^2\,g_{Pt}}$. This is within the range of the electrodes tested by Kunz and Gruver [112] and on par with the areas reported by Lobato et al. [75], but significantly larger than reported by other sources [116–118]. This value should be seen in the light of the catalyst loading, which is more than six times larger than the loading used by Kunz and Gruver. This should be expected to give very good performance, but the IR corrected voltage at $1\,\mathrm{A\,cm^2}$ is only around 0.56 V. This means that the effect of the large catalyst area is countered by other losses. Figure 5.2 shows the local current density and the local oxygen mole fraction within the catalyst layer. As shown in the plots, almost all of the reactions occur within the first 30% of

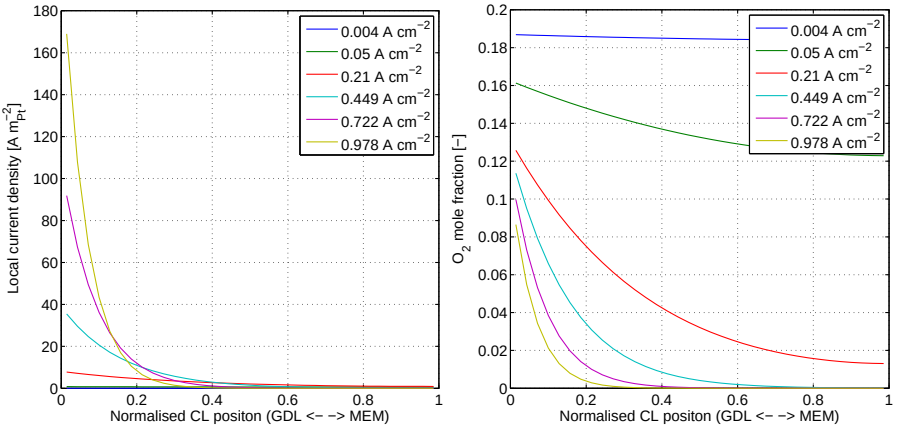

Figure 5.2 – Reaction rates vs. position within the catalyst layer (left) and oxygen mole fraction vs. position within the catalyst layer (right). The membrane side is rightmost in the plots. Plots for case 1. $\lambda = 2$, $T = 160\,^{\circ}\mathrm{C}$.

the catalyst layer, when the current density becomes high. This means that the catalyst ESA actually taking part in the electrochemical reactions at high current density is only about $14\,\mathrm{m}^2\,\mathrm{g}_{\mathrm{Pt}}$. The oxygen mole fraction profiles also indicate that there is a very strong diffusion limitation in the catalyst layer, given the rapid decrease in oxygen mole fraction at higher current densities. This is mainly due to the large PA loading. At this loading, the volume fraction of PA in the catalyst layer is more than 20% while the porosity is 10%-12% depending on the local acid concentration. This number is very low compared to the values used by other sources [54, 57, 58, 61]. Also, of these sources, only Chippar and Ju [61] considered Knudsen diffusion.

The first characteristic deviation between the behaviour of the simulated and measured curves is the difference in performance between the polarisation curves at different stoichiometry. The measured polarisation curves are almost coincident until about $0.6\,\mathrm{A\,cm}^{-2}$, where concentration losses start to become important. At higher current densities, the low stoichiometry curve shows worse performance as should be expected. The simulated curves, on the other hand, have significantly different performance (about 20mV) in most of the range. The measured curves only reach this difference at around $1\,\mathrm{A\,cm}^{-2}$. Also, the simulated curves do not exhibit the characteristic concentration loss region, in spite of the high diffusion resistance. Since this is not consistent with the behaviour of the recorded polarisation curves, the fitting values might not be realistic.

The simulated impedance spectra are able to reproduce the general trends from the data. The impedance spectrum shrinks when the current density is increased and the low frequency impedance becomes more important when lowering

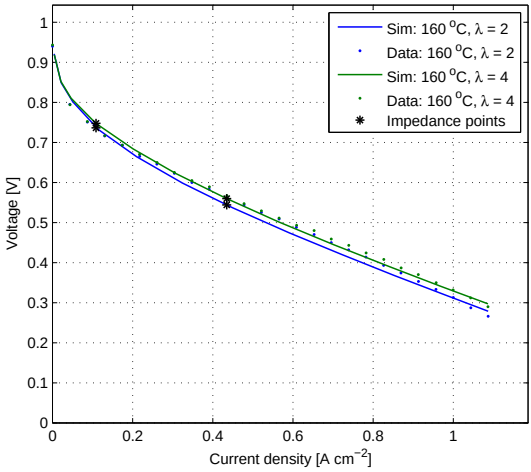

Figure 5.3 – Fitted polarisation curves for fitting case 1.

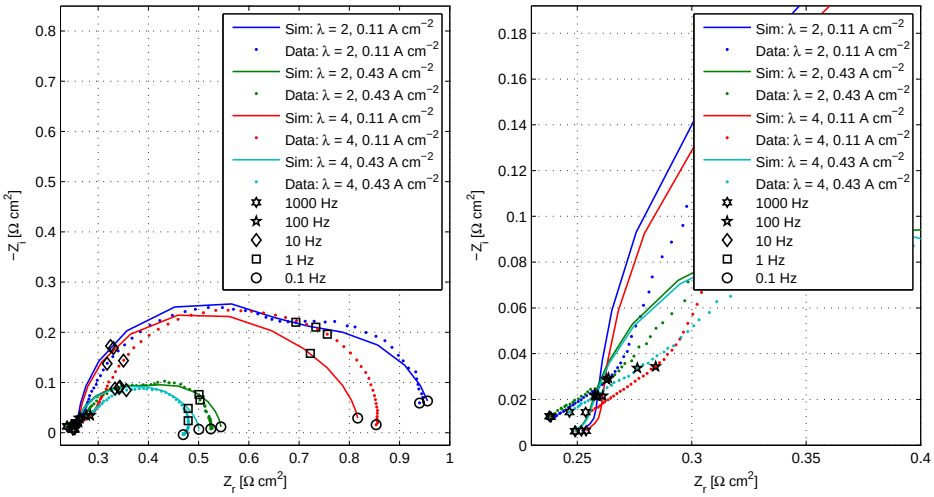

Figure 5.4 – Fitted impedance spectra for case 1. Left: All the spectra. Right: Detail of the high frequency region.

the stoichiometry. The frequency ranges in which the individual contributions are dominant are also quite consistent between the simulation and the data. Other consistent details include the low frequency loop being larger than the high frequency loop in the spectrum recorded at 0.43 A cm^{-2} and $\lambda = 2$ and the transition between the low and intermediate frequency loops taking place just above 1 Hz

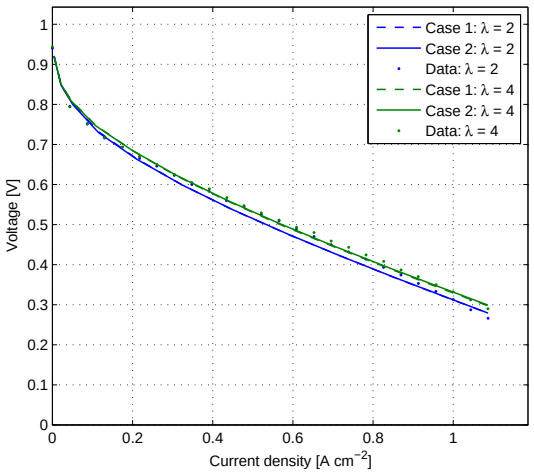

Figure 5.5 – Fitted polarisation curves for fitting case 2 compared to case 1.

in the spectrum recorded at $0.11\,\mathrm{A\,cm^{-2}}$ and $\lambda = 2$.

The simulated impedance spectra also deviate somewhat from their measured counterparts, however. A common feature of all the simulated curves is the under prediction of the 45° slope between 1 kHz and 100 Hz. In case of the simulated curves, the large intermediate frequency loop begins almost immediately after the 1 kHz mark. This also results in the intermediate frequency loop being shifted towards the origin relative to the measured curves. This feature is related to the conductivity of the catalyst layer. The lower the catalyst layer conductivity, the larger the 45° slope. This indicates that the catalyst layer conductivity is too high in the fit. Another difference is in the effect of stoichiometry. At the $0.11\,\mathrm{A\,cm^{-2}}$, the measured curves exhibit a significant difference between the real parts in the high frequency region. In the simulated curves, the difference between the curves is smaller, and the main difference is seen between curves at different currents, not at different stoichiometry. Here, the curves simulated at $0.43\,\mathrm{A\,cm^{-2}}$ coincide in the high frequency region, whereas for the data, the coinciding curves are those recorded at $\lambda = 2$. The difference in stoichiometry becomes more significant in the simulated curves below 10 Hz. In the low frequency region, the low frequency inductive contribution is missing in the simulated spectra. This seems to lead to over prediction of both the real and imaginary parts of the impedance below 1 Hz in the spectra at $0.43\,\mathrm{A\,cm^{-2}}$. There is also a problem with respect to the low frequency dynamics at low currents, since at $0.11\,\mathrm{A\,cm^{-2}}$ and $\lambda = 4$, the low frequency loop is under predicted, while the agreement is acceptable at $\lambda = 2$.

The ratios of the maximum real part of the impedance to the slope of the polarisation curve for case 1 are given in figure 5.1. Here one of the problems of

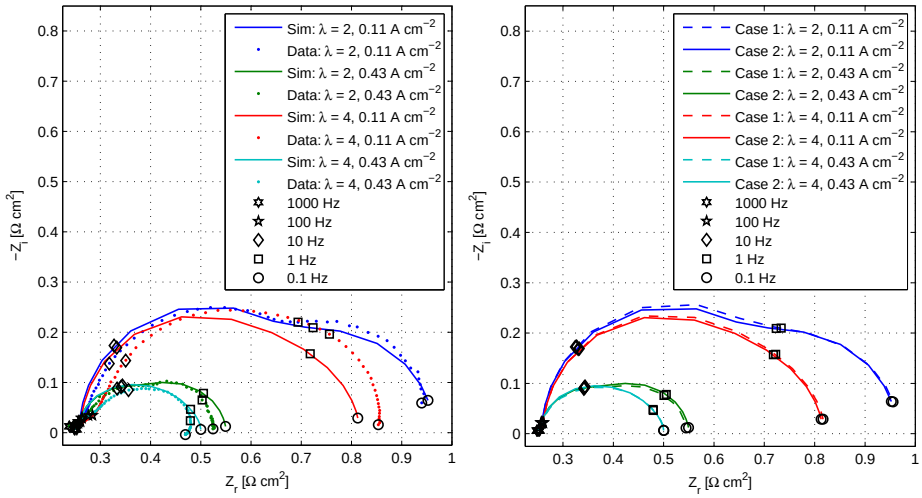

Figure 5.6 – Fitted impedance spectra for case 2. Left: All the spectra. Right: Comparison to the impedance spectra of case 1.

the model becomes apparent. While the measured resistance ratios do not change much when changing DC current, the change is significant when simulating. Here, the ratio is in good agreement with the data at $0.43\,\mathrm{A\,cm^{-2}}$ but at $0.11\,\mathrm{A\,cm^{-2}}$ the simulated value is significantly smaller than the measured. With respect to the trend of lower resistance ratio at high stoichiometry, the simulation results follow the data quite well.

5.3.2 Case 2: $\gamma_{\mathrm{O}_2} = 1.2$, $\alpha \mathbf{n}_{\mathrm{O}_2} = 1$

The only difference in the fixed parameters between cases 1 and 2 is the reaction order with respect to oxygen concentration, which is set to 1.2 in this case. The residuals for the converged solutions are similar as well as the deviation of the individual curves. The main differences in the fitted parameters between cases 1 and 2 are in the catalyst ESA (+37%) and carbon surface area (-17%). The increased ESA increases the exchange current density to make up for the effects of increased dependence on oxygen concentration. The oxygen concentration itself is increased through the lowering of $A_{\mathrm{C,m}}$, which serves to lower the Knudsen diffusion resistance.

The behaviour of the impedance spectra and the polarisation curves is almost identical to what is exhibited by case 1. The polarisation curves and impedance spectra are given in figures 5.5 and 5.6. For the polarisation curves, the voltage is marginally higher at $\lambda = 4$, while the difference is hardly discernible at $\lambda = 2$. The low current impedance spectra exhibit shrinkage of the intermediate frequency

loop. At high current, the intermediate frequency loop grows slightly.

The resistance ratios are slightly higher compared to case 1, but the low current ratios are still much too low compared to the data.

5.3.3 Case 3: $\gamma_{O_2} = 0.6$, $\alpha n_{O_2} = 1$

For case 3, γ_{O_2} is lowered to 0.6. This reflects that that the apparent reaction order of the measured polarisation curves is in this range (see section 4.3.4). This could be expected to give a better agreement between the model and the data in steady state. This is, however, not the case. As seen in table 5.4, the deviation of both polarisation curves is slightly larger in this case compared to case 1. On the other hand, the impedance spectra follow the data better in all cases, resulting in a net decrease of the objective function value of 15%.

The most significant differences in the fitted parameters with respect to case 1 are in the ESA (-48%) and the carbon surface area (+84%), decreasing the total exchange current density and increasing the Knudsen diffusion resistance to correct for the reduced sensitivity to oxygen concentration. The other parameters change more modestly. The PA loading goes down, while R_{misc} and C_{dl} go up.

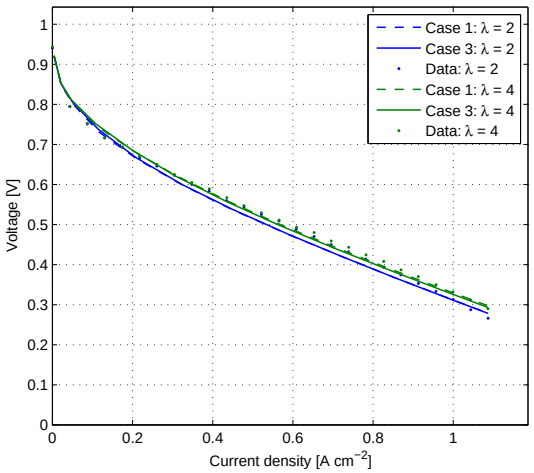

Figure 5.7 – Fitted polarisation curves for fitting case 3 compared to case 1.

In figure 5.7, the polarisation curves are compared to the data as well as the case 1 simulations. Here, the reason for the larger deviation is revealed. While the case 3 curves are marginally closer together, the voltage is lower in most of the range compared to the case 1 curves. This means that the under prediction of the voltage in the range $0.4 - 1\,\text{A cm}^{-2}$ is larger in case 3. Also, the problems related to the general shape of the polarisation curves remain unaddressed in this fit.

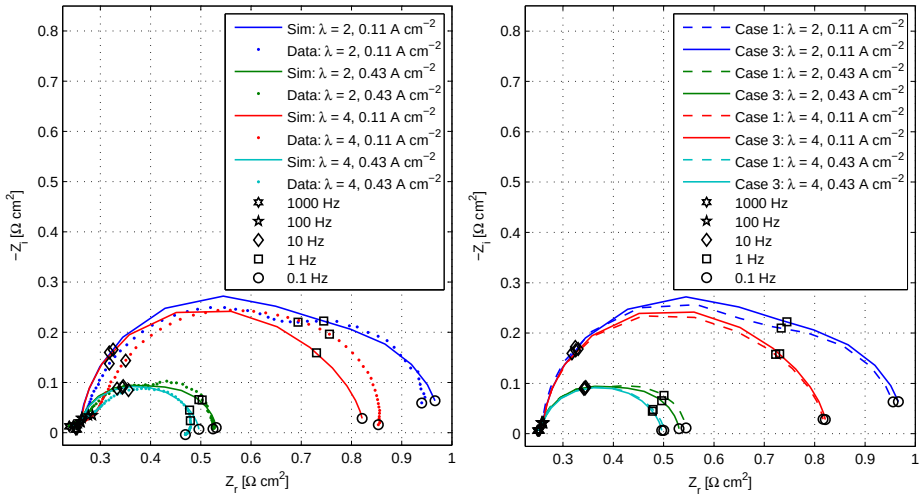

Figure 5.8 – Fitted impedance spectra for case 3. Left: All the spectra. Right: Comparison to the impedance spectra of case 1.

The picture is slightly more complicated in case of the impedance spectra. All the simulated impedance spectra have smaller RMS and maximum deviations. The high current spectra are smaller, reducing the over prediction of the impedance in the intermediate to low frequency range. In the same range, the low current spectra become larger, resulting in reduced under prediction (and even some over prediction in the case of $\lambda = 2$) of the impedance. Comparing the curves of case 3 and case 1 directly, it shows that the shrinkage of the high current spectra primarily occurs for $\lambda = 2$ at low frequency, while the growth of the low current spectra occurs at intermediate frequency. While this on average brings the curves in better agreement with the data, the agreement is not improved when considering the relative importance of the individual parts of the curves. This is most clear in the case of $\lambda = 2$, $i_{\mathrm{DC}} = 0.43\,\mathrm{A\,cm^{-2}}$, where the low frequency loop becomes smaller than the intermediate frequency loop. This disagrees with the evidence presented by the data.

Looking at the resistance ratios in figure 5.1, it shows that the agreement here is not improved. Actually, the resistance ratios in the simulations are slightly smaller than in case 1. This is likely a direct result of the weaker dependence on the oxygen concentration.

5.3.4 Case 4: $\gamma_{\mathrm{O}_2} = 1$, $\alpha \mathbf{n}_{\mathrm{O}_2} = 1$, Low PA loading limit

In case 4, an attempt is made to remedy the missing slope in the high frequency region of the impedance spectra by narrowing the limits for the catalyst layer PA

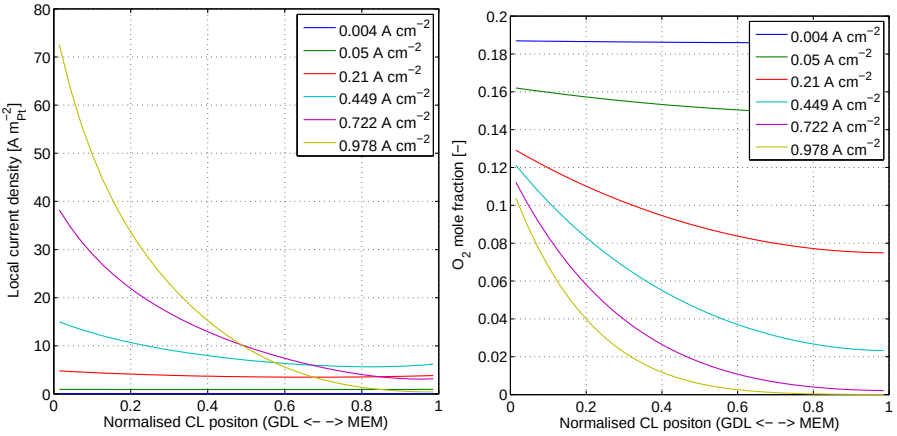

Figure 5.9 – Reaction rates vs. position within the catalyst layer (left) and oxygen mole fraction vs. position within the catalyst layer (right). The membrane side is rightmost in the plots. Plots for case 4. $\lambda = 2$, $T = 160\,^{\circ}\mathrm{C}$.

loading. The upper limit is set to $0.45\,\mathrm{mg\,cm^{-2}}$, since initial simulations have revealed that values in this range give high frequency slopes comparable to those in the data. As can be seen from table 5.3, the fitting algorithm converges to the upper limit. This 52% reduction of the PA loading affects the fit in a number of ways. The carbon surface area goes up by 101%, partially counteracting the reduction in diffusion resistance due to increased CL porosity. The ESA decreases by 26% to accommodate the easier access of oxygen to the electrode. The double layer capacitance also increases significantly. R_{misc} is unchanged. This is counter intuitive, since lower CL PA loading increases the total resistance.

The effects of the parameter changes on local oxygen mole fraction and reaction rate are shown in figure 5.9. Here, the importance of the lower diffusion resistance is reflected in the much higher oxygen concentration compared to case 1. In case 1, the mole fraction starts falling below 2% close to the membrane at $0.21\,\mathrm{A\,cm^{-2}}$, while it only approaches 2% at the membrane at $0.45\,\mathrm{A\,cm^{-2}}$ in case 4. The reactions are also much more distributed in the CL. The maximum current density per platinum area is less than half of that of case 1, even though the available catalyst area is 26% less.

Comparing the deviation of the individual curves to those of case 1, the general trend is that the polarisation curves are in better agreement with the data, while the agreement of the impedance spectra is worse. The disagreement is larger at $0.11\,\mathrm{A\,cm^{-2}}$. At $\lambda = 4$, the RMS and maximum deviation are 8.44% and 15.3% respectively. The only impedance spectrum which exhibits smaller deviation compared to case 1 is at $0.43\,\mathrm{A\,cm^{-2}}$ and $\lambda = 4$. Here, the deviations are less than half compared to case 1.

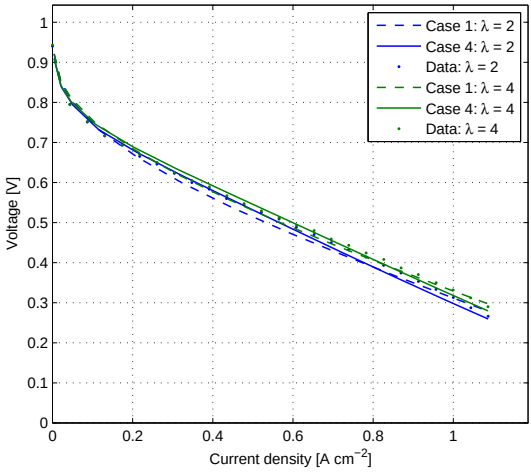

Figure 5.10 – Fitted polarisation curves for fitting case 4 compared to case 1.

The polarisation curves for case 4 are shown in figure 5.10. Compared to the curves of case 1, the activation dominated region is smaller than in the case 4 curves. Above $0.2\,\mathrm{A\,cm^{-2}}$, the development of both curves is linear with respect to current density. The voltage difference between the polarisation curves due to stoichiometry now also develops approximately linearly with respect to current density. The model still does not capture the onset of concentration polarisation around $0.6\,\mathrm{A\,cm^{-2}}$, but otherwise, the agreement is better than for the previous cases.

The impedance spectra of case 4 are shown in figure 5.11. In the impedance spectra, the impedance is under predicted in most of the range for the spectra at $0.11\,\mathrm{A\,cm^{-2}}$. In the $0.43\,\mathrm{A\,cm^{-2}}$ spectra, the agreement is good. The effect of stoichiometry seems to be slightly over predicted, however, since the low frequency impedance is too great at $\lambda = 2$ and slightly too small at $\lambda = 4$. In the right plot in figure 5.11, another problem is shown. The result of the unexpected increase in R_{misc} is a translation of the impedance spectra to the right with respect to the data. This translation corresponds to an over prediction of the ohmic losses in the fuel cell. This is most likely done by the fitting algorithm to compensate the large deviation between the data and the simulations at low frequency. The high frequency feature does, however, agree better with the data, than in case 1.

In figure 5.1 it can be seen, that the simulated resistance ratios for case 4 are smaller for $\lambda = 2$ than in case 1.

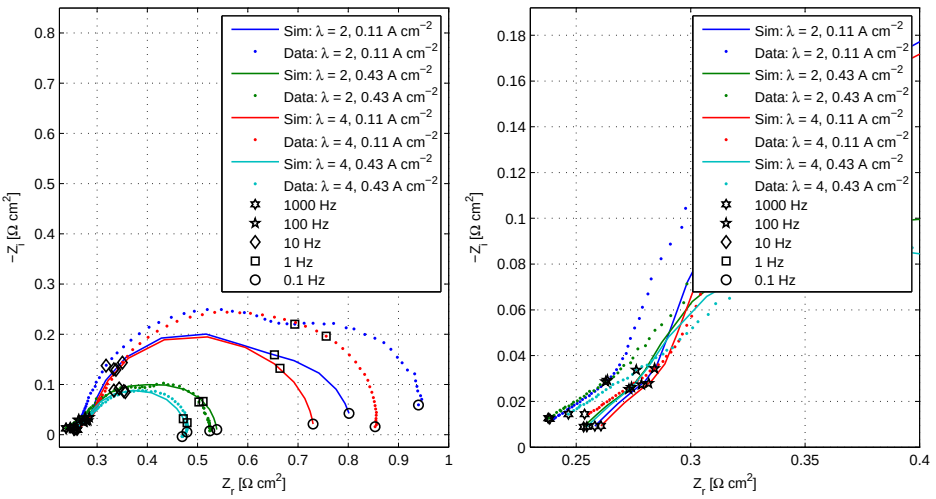

Figure 5.11 – Fitted impedance spectra for case 4 compared to the data. Left: All the spectra. Right: Zoom of the high frequency region of the spectra.

5.3.5 Case 5: $\gamma_{O_2} = 1$, $\alpha n_{O_2} = 1$, Low CL conductivity

In this case, the catalyst layer conductivity model is changed so that the conductivity is calculated using (4.46) rather than (4.44) and (4.45) (see page 66). This results in a significantly lower catalyst layer conductivity. This should in turn affect the high frequency region of the impedance spectra to better represent the actual behaviour. The overall fit quality is not improved by this modification. The objective function value is 83% higher than for case 1.

As in case 4, the main source of the higher residuals are the low current impedance spectra which are much smaller than their measured counterparts. The agreement is better for the high current spectra. Here the simulated curves only deviate in the low frequency region, where the effect of stoichiometry seems to be over-predicted. In the high frequency region, the agreement is remarkably good, except that the low current intermediate frequency loop shows at 100 Hz in the data, while the simulated curves have them start at a lower frequency.

The polarisation curves differ from those of the previous cases by over-predicting the voltage in the range up to 0.5 A cm^{-2}. Around this point, the slope of the curves becomes steeper so that the simulated curves cross the measured curves. This results in a significant under prediction of the voltage at higher current densities.

The effects on the fitting parameters generally make the electrode more accessible. The carbon surface area is reduced by 47% and the PA loading is reduced by 17%. The greater accessibility means that the available catalyst ESA is used

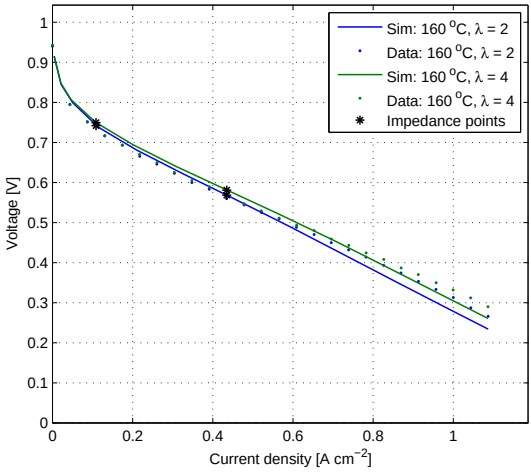

Figure 5.12 – Fitted polarisation curves for fitting case 5.

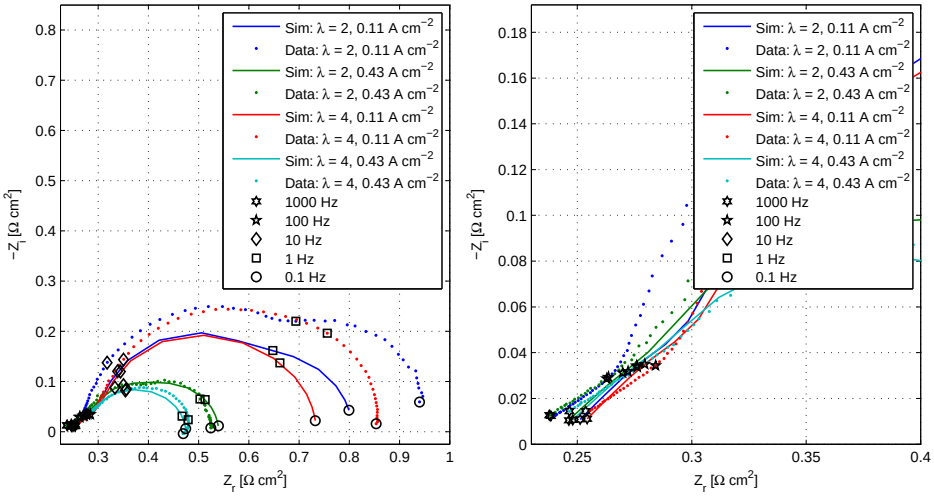

Figure 5.13 – Fitted impedance spectra for case 5. Left: All the spectra. Right: Zoom of the high frequency region of the spectra.

more efficiently, so the ESA is reduced by 14% to compensate. The combined effect of the changed conductivity model and the reduced PA loading increases the ohmic losses in the CL. To accommodate this, the miscellaneous resistance decreases by 12%. The specific carbon surface area of $100\,\mathrm{m^2\,g^{-1}}$ is maybe not realistic, considering that the Pt surface area is $40.1\,\mathrm{m^2\,g^{-1}}$. This would mean

that 40% of the pore surface is covered with Pt.

The deviation of the polarisation curves are about twice as large as in case 4. The low current impedance spectra deviate almost the same as in case 4. The high current spectra have higher maximum deviations but the RMS deviation is higher and lower at $\lambda = 2$ and $\lambda = 4$ respectively.

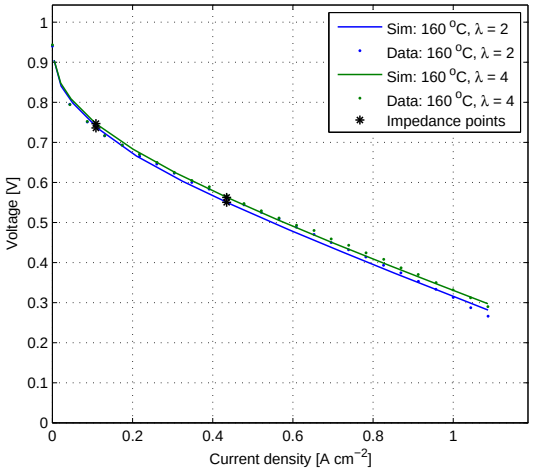

Figure 5.14 – Fitted polarisation curves for fitting case 6.

5.3.6 Case 6: $\gamma_{O_2} = 1$, $\alpha n_{O_2} = 1.25$

In case 6, the value of αn_{O_2} is set to 1.25 to investigate the suitability of reducing the Tafel slope. An initial attempt using $\alpha n_{O_2} = 2$ was made, but the resulting fit was very poor. The plots of the fitted results are given in figures 5.14 and 5.15. The fit is much better than any of the previous attempts with an objective function value 49% lower than case 1. The main changes in fitting values are in carbon surface area and PA loading. The carbon surface area is as high as $976\,\mathrm{m}^2\,\mathrm{g}$. While carbon powders of such large specific surface areas exist, the value is hardly realistic for a porous electrode in which the carbon particles are bound together. The PA loading is decreased by 27%, increasing the importance of the high frequency contribution a little.

The shape of the polarisation curves is similar to that of cases 1-3, only the voltage difference between air stoichiometry of 2 and 4 is smaller. In the impedance spectra, the disagreement between the simulations and the data is similar to case 1 in the high frequency region, even if the 45° region is larger. The agreement of the low current impedance spectra is better than for any of the previous cases. This is especially true for the $\lambda = 2$ case, which only deviates visibly close to 0.1 Hz and in the high frequency region. For the high current spectra, the agreement

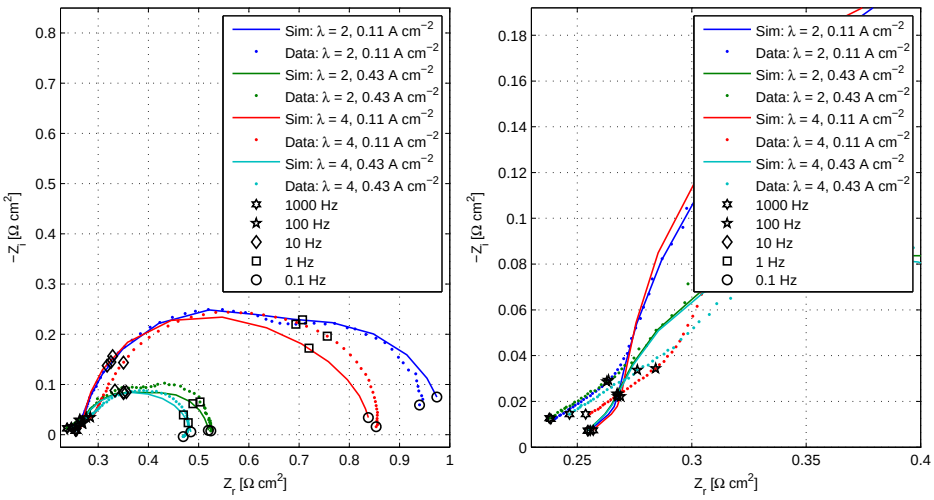

Figure 5.15 – Fitted impedance spectra for case 6. Left: All the spectra. Right: Zoom of the high frequency region of the spectra.

is generally better than in cases 1-3, but the intermediate frequency contribution is shifted towards higher frequencies, resulting in under prediction below 10 Hz.

Looking at figure 5.1, it shows that the resistance ratio is under predicted by the model. The size distribution of the resistance ratios is quite interesting, however. When compared with the other fitting cases, the distribution reflects that of the data much better.

5.3.7 Case 7: $\gamma_{O_2} = 1$, $\alpha n_{O_2} = 0.75$

Changing the value of αn to 0.75, also improves the fit. With an objective function value 47% lower than in case 1, this case shows an agreement close to that of case 6. It is interesting that a better fit is achieved both by increasing and decreasing αn. The polarisation curves are shown in figure 5.16. The behaviour of the polarisation curves is close to what is displayed by the data in most of the range. The slope is slightly too steep around the impedance points and the $\lambda = 2$ curve under predicts the voltage significantly above $0.4\,\mathrm{A\,cm^{-2}}$. Also, both curves over predict the voltage at low current more than when $\alpha n = 1$. Otherwise, the simulations agree quite well with the data. The distinction between activation region and linear region is more believable than in cases 1-3 and 6, even if the voltage difference between the curves increases more linearly than in the data. In spite of this, the RMS deviation of the curves is larger than for any of the other cases.

Except at $0.11\,\mathrm{A\,cm^{-2}}$ and $\lambda = 2$, the impedance shows smaller RMS devi-

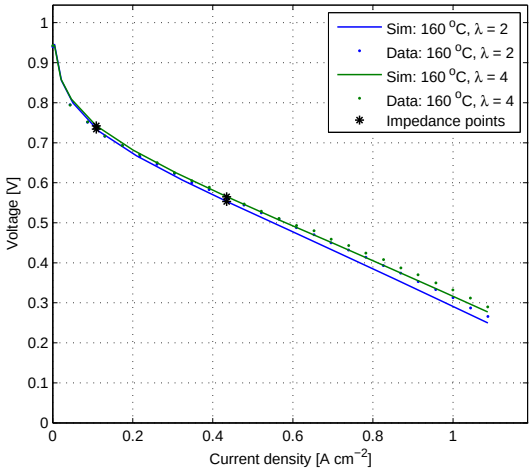

Figure 5.16 – Fitted polarisation curves for fitting case 7 compared to the data.

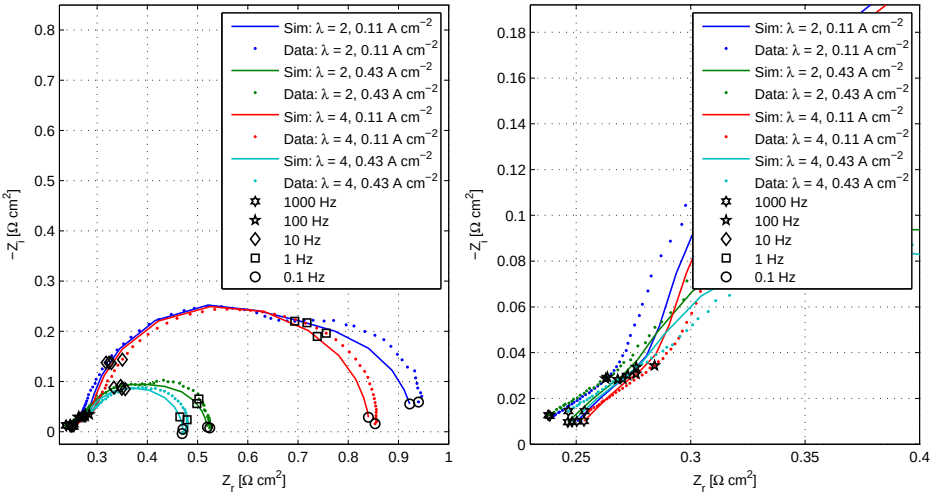

Figure 5.17 – Fitted impedance spectra for case 7 compared to the data. Left: All the spectra. Right: Zoom of the high frequency region of the spectra.

ations than any of the previous cases. No spectrum has RMS deviation above 2.13%. As shown in figure 5.17, the agreement is best in the high-intermediate frequency region. Apart from the inability of the model to get the right distribution of the purely resistive contributions, the only significant deviation from the data is seen in the low frequency loop, which is too small.

The resistance ratios are under predicted by the model in this case as well. This agrees with the over predicted slope of the polarisation curve.

5.3.8 Case 8: γ_{O_2} and αn_{O_2} included in optimisation

In case 8, the reaction order and the transfer coefficient are set free to be tweaked by the fitting algorithm. Adding two extra degrees of freedom to the optimisation problem enables it to converge to a more optimal solution as should be expected. The objective function value converges to a value 58% lower than in case 1. The transfer coefficient converges to 0.80 and the reaction order is 1.48. The ESA converges to the upper limit of $100\,\mathrm{m^2\,g_{Pt}^{-1}}$. This is a result of the high reaction order, but the surface area is probably not realistic, since it is much higher than any of the literature values given in table 4.5 on page 61. The carbon surface area is close to the value for case 1, while the other parameters are within a few percent of the values from case 7.

The fit of the polarisation curve is better than in case 7, but still worse than for cases 1-4. As with case 7, the polarisation curve slope is too steep in the linear range. The voltage difference between the curves is larger than in case 7, due to the high reaction order. The development trend is similar to case 7.

The impedance spectra exhibit the best RMS fits of all the cases, except at $0.11\,\mathrm{A\,cm^{-2}}$ and $\lambda = 4$, which is second only to case 7. The intermediate frequency contributions are smaller compared to case 7 but the low frequency contributions are larger at $\lambda = 2$. The 1-0.1 Hz part agrees particularly well for $\lambda = 2$, $0.11\,\mathrm{A\,cm^{-2}}$.

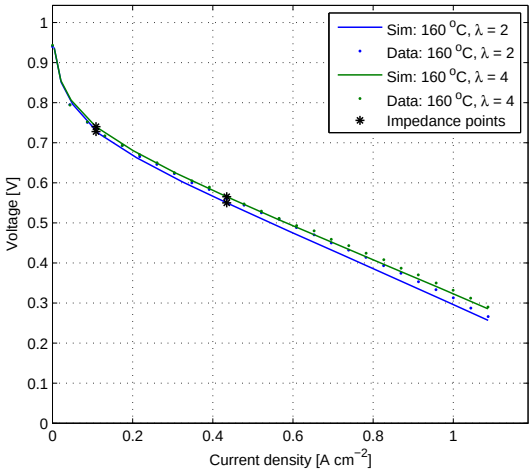

Figure 5.18 – Fitted polarisation curves for fitting case 8 compared to the data.

The distribution of the resistance ratios is similar to case 7, but all ratios are slightly larger. The agreement with the data values is still not satisfactory.

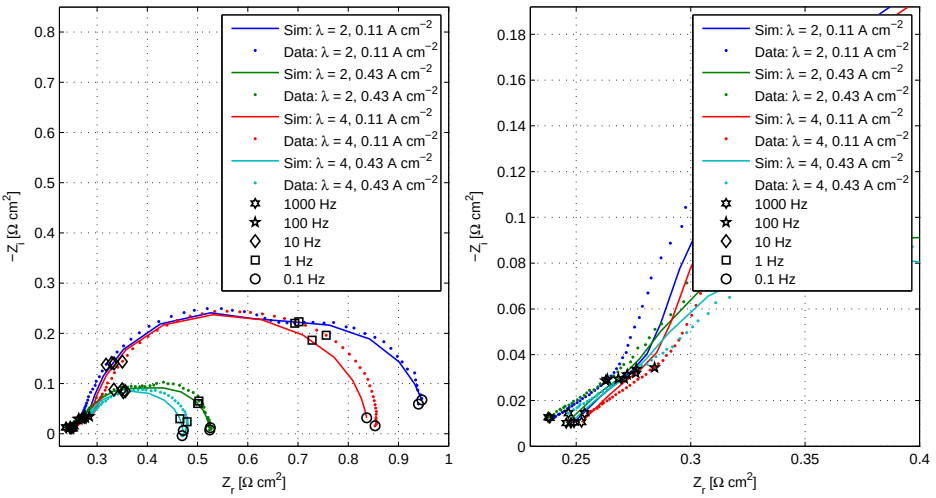

Figure 5.19 – Fitted impedance spectra for case 8 compared to the data. Left: All the spectra. Right: Zoom of the high frequency region of the spectra.

5.3.9 Case 9: 2-step model

In case 9, the reaction mechanism is changed. Now all the reactions are assumed to proceed in a two step reaction with H_2O_2 as the intermediate as described in section 4.3.3. The overall fit is 55% better than case 1, making it the second best fit so far.

The fitting parameter set is significantly different from previous results. The ESA is the 37% lower than in case 1. Except for case 3, where the activity was increased by lowering the reaction order, this is the lowest ESA obtained. The carbon surface area is increased by 74% and the PA loading is decreased by 60%. The PA loading is the lowest obtained.

The low objective function value is primarily derived form the polarisation curves, which have maximum RMS deviation of 0.77% at $\lambda = 4$. The impedance spectra are another story. With a maximum RMS deviation of 3.22% at $0.43\,\mathrm{A\,cm^{-2}}$ and $\lambda = 2$, the impedance fits are generally better than for cases 1-5. Even so, the spectra lack the distinction between the intermediate and low frequency loops. Also, the effect of stoichiometry small. In the low current spectra, there is only a small difference above 1 Hz and in the high current spectra, the case is similar above 10 Hz. The right plot in figure 5.21 shows comparison of the impedance spectra obtained using the 2-step model and the 1-step model with

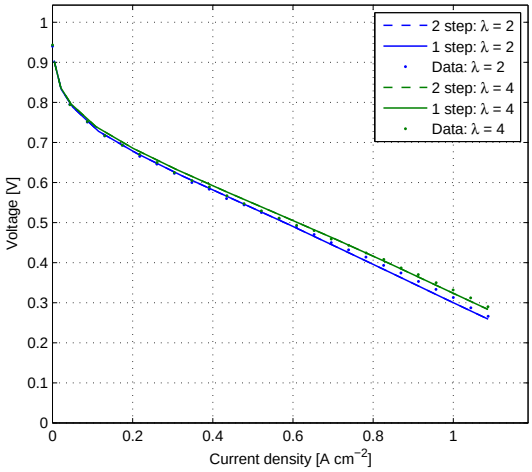

Figure 5.20 – Fitted polarisation curves for fitting case 9 compared to the data. Simulations are run for both 1- and 2-step model versions with the same parameters. The curves are coincident.

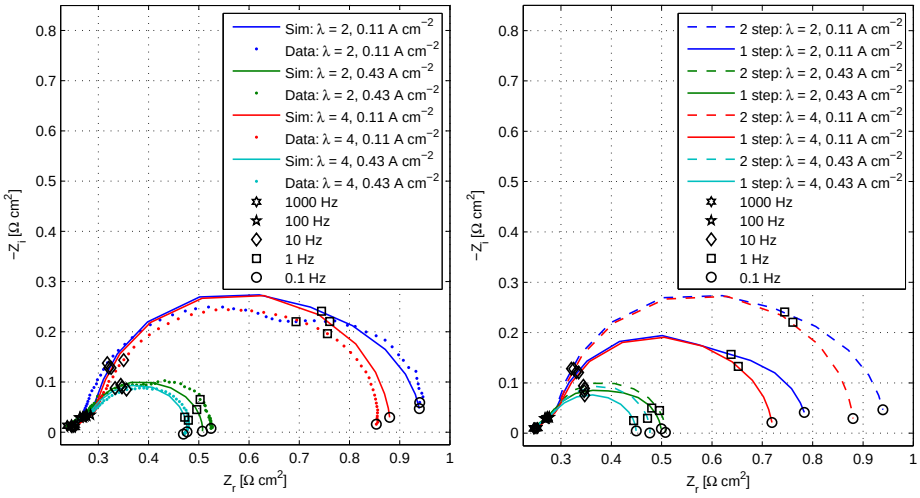

Figure 5.21 – Fitted impedance spectra for case 9 compared to the data. Left: Fitted spectra compared to the data. Right: Comparison of spectra generated using the 3-step and the 1-step models.

the case 9 parameters. As can be seen, the 2-step model inflates the intermediate frequency loop. The effect is most significant at low current. Also, there is no

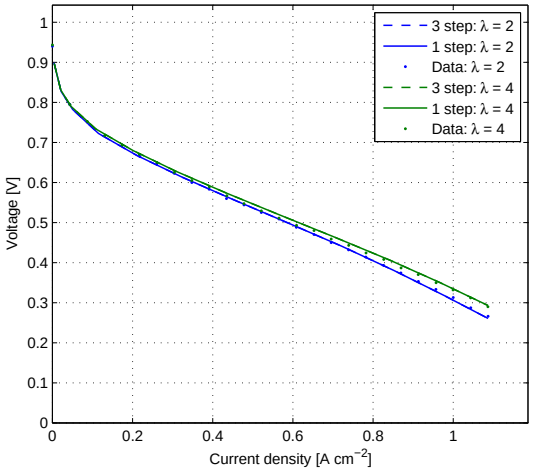

Figure 5.22 – Fitted polarisation curves for fitting case 10 compared to the data. Simulations are run for both 1- and 3-step model versions with the same parameters. The curves are coincident.

low frequency inductive effect of this multi step approach.

The effect at low current are reflected by the resistance ratios (figure 5.1). Here the low current ratios are both above 1.2 while the high current ratios are around 1.1. As in the spectra, the stoichiometry effect is very small. All in all, the results of this fitting case do not indicate, that the two step mechanism in question is a good model of the HTPEM reaction kinetics.

5.3.10 Case 10: 3-step model

For the final fitting case, an attempt is made to fit the model using the 3-step reaction mechanism (see (4.27) on page 58). The fitted curves are shown in figures 5.22 and 5.23. The overall fit is worse than for the 2-step model, but the polarisation curve fit is near-perfect, including the onset of concentration losses. The decoupling of the intermediate frequency loop in the impedance spectra is similar to the 2-step model but the reduction of the stoichiometry effect is even more significant. As with the 2-step model, there is no change in the polarisation curve when switching to the 1-step model using the same parameters. In the impedance spectra the difference between 1-step and 3-step is similar to that of case 9, only the effect of stoichiometry on the low frequency part of the spectra is less than half compared to the case with the effect when using the 1-step model. Also, the high current spectra are much smaller when using the 1-step model.

The resistance ratios are all much higher. The dependence on stoichiometry is the reverse of the other cases. Here the resistance ratios increase with the

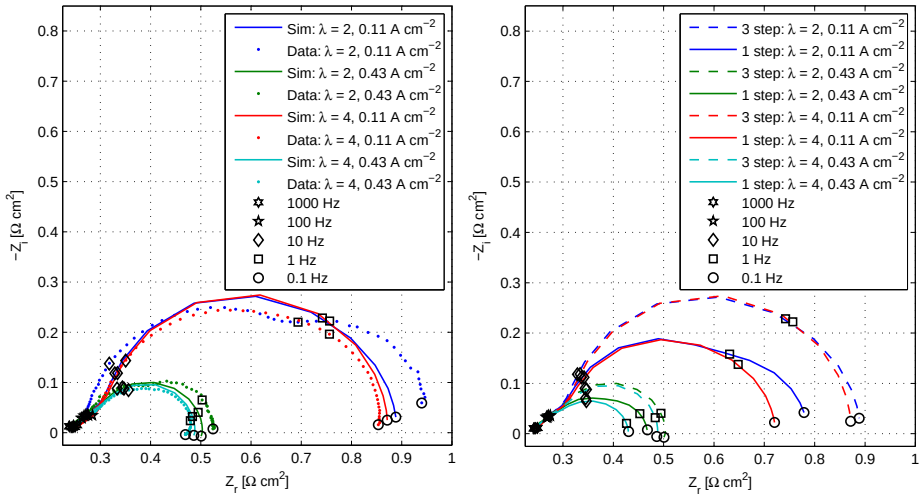

Figure 5.23 – Fitted impedance spectra for case 10 compared to the data. Left: Fitted spectra compared to the data. Right: Comparison of spectra generated using the 3-step and the 1-step models.

stoichiometry. As with the 2-step model, it must be concluded that modelling the electrode reactions as multi-step is not feasible, using the approach applied in this work.

5.3.11 Fitting conclusions

The main conclusion from trying to fit the model is that this task is far from trivial. While many of the fitting cases exhibit good correlation between the simulation results and part of the data, there seems to be some problems in all cases.

From the plotted current density and oxygen mole fraction contours, it seems that the gas phase diffusion resistance plays a prominent role in the simulated results. At high current densities, the reactions mainly take place close to the CL-GDL interface leaving much of the catalyst layer inactive. The catalyst surface area is in the range $40 - 50\,\mathrm{m^2\,g^{-1}}$ for most of the fitting cases. This number is in the high end of the range of values found in the literature. If this is indeed the true value of the catalyst ESA, it is a testament to the high diffusion losses, since the performance is not quite on par with the high catalyst loading.

The attempts made at modelling the oxygen reduction reaction as a multi step process turned out not to produce any improvement in the agreement between the model and the data. The introduction of the intermediate steps affects the intermediate frequency loop, but limits the impact of the stoichiometry on the

impedance spectra well below what can be observed in the recorded impedance spectra.

The polarisation curves generally exhibit two types of development, depending on the values of the fuel cell parameters. The first type is exhibited in cases 1-3 and 6. Here the activation region seems to span the whole current density range, since there is never any clear transition to a linear region or a concentration dominated region. This behaviour disagrees with what is observed in the measured polarisation curves, where all three regions can be distinguished. Also, this behaviour in the polarisation curve coincides with a relatively high PA content in the electrode and an under predicted high frequency contribution.

The other polarisation curve type exhibits at least both an activation region and a linear region with maybe a small concentration region. These curves can be seen in cases 4, 5 and 7-10. While this behaviour is better in line with what is observed in the data, there are still some issues with the results in these cases. Either the strict mathematical agreement between the simulated and recorded polarisation curves is worse than in cases 1-3 and 5, or the impedance spectra fit poorly. At any rate, this behaviour of the polarisation curve is more believable in these cases.

Another issue is that some cases converge to values for some of the parameters that may be unreasonable. This happens in case 5, where the carbon surface area converges to the lower limit of $100\,\mathrm{m^2\,g^{-1}}$, in case 6, where the carbon surface area becomes unreasonably high and in case 8, where the ESA lands at $100\,\mathrm{m^2\,g^{-1}}$, which is much higher than any literature value. In spite of cases 6 and 8 fitting the data well, the peculiar fitting parameter values indicate that they do not represent the actual fuel cell properly.

Considering the good agreement of the impedance spectra, the believable simulated polarisation curves, and the absence of any clearly unreasonable fitting parameters, case 7 is considered the most reasonable result.

5.4 Reactant concentration dynamics

This section is devoted to an investigation of the importance of the dynamics of the cathode gas composition in the impedance spectra. Figure 5.24 show simulated spectra for three different situations. One using the full dynamic model, one where the gas composition in the channel is fixed at the steady state value, and one where the gas composition in the entire electrode is fixed.

The importance of the gas channel dynamics is clearly shown in the plots. When fixing the gas channel composition, the whole of the low frequency loop disappears. This happens at both low and high current. This strongly indicates that the usual practice of modelling the low frequency loop using a bounded Warburg impedance is not physically sound, since the distinct low frequency loop derives from the channel dynamics.

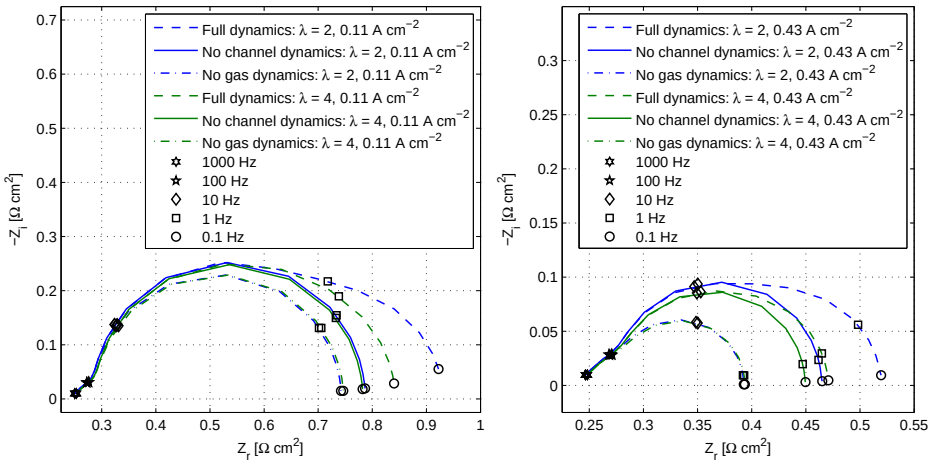

Figure 5.24 – Impedance spectra for case 7 illustrating the effects of the gas dynamics.

The diffusion inside the porous media does play a role in the impedance, however. The importance of the diffusive contribution is higher at higher current. At 0.11 A cm^{-2}, the spectra with constant channel composition are almost coincident, while at 0.43 A cm^{-2}, the impedance is significantly larger at low stoichiometry. When fixing the total gas composition, the spectra shrink once more compared to the case of constant channel composition only. This effect is most prominent at 0.43 A cm^{-2} and $\lambda = 2$. When the whole gas composition is fixed, the spectra are coincident both at low and high current. At high current, the top point of the intermediate frequency loop moves towards higher frequency, indicating that the time constants of diffusion are indeed slower than those of the electrode kinetics, but not enough for the resulting loops to be distinguishable in the impedance spectra.

5.5 Effect of EIS current on results

As the reader should no doubt now be aware, the impedance spectra used when fitting are recorded at 0.11 A cm^{-2} and 0.43 A cm^{-2}. Impedance spectra have also been recorded at 0.22 A cm^{-2} and 0.33 A cm^{-2}. In order to validated the model, the ability to reproduce these spectra must be assessed. The full range of the spectra is shown in figure 5.25. As shown, the agreement is less good at the two intermediate currents. The impedance is under predicted in the range below 10 Hz. The low frequency loop is not very pronounced at $\lambda = 2$ compared to the data. These issues are similar to those exhibited by the spectra which are fitted

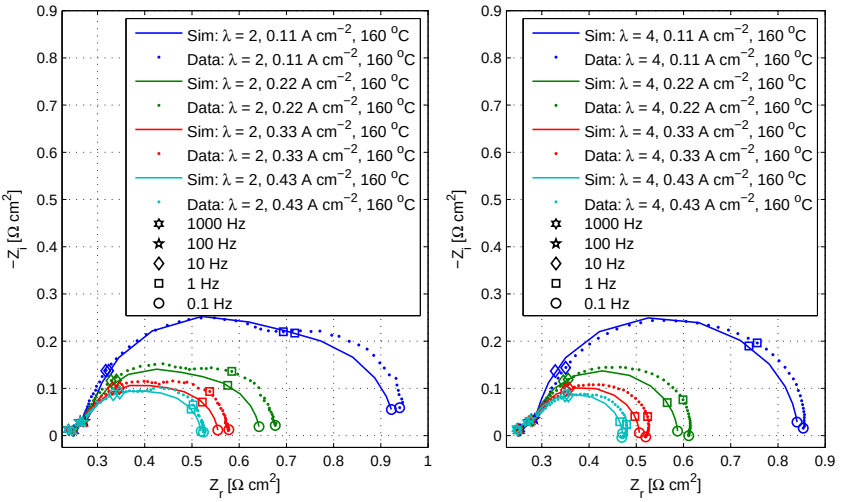

Figure 5.25 – Plots of the full range of impedance spectra recorded at 160 °C, compared to simulated spectra at the same conditions using the case 7 parameters.

directly, even if they are more pronounced. All in all, the trends when changing the current in the model agrees with what is exhibited by the data, in spite of the poorer fit of the individual spectra.

5.6 Effect of temperature on results

Since many aspects of the model take into account the operating temperature, an important part of the model validation is to investigate the effect of the operating temperature on the simulation results. Simulated polarisation curves and impedance spectra at 140°C, 160°C, and 180°C are shown in figures 5.26 and 5.27.

There are a number of problems with the ways the simulation results change when changing the temperature. The development of the polarisation curves is to some degree the opposite of what should be expected. When lowering the simulation temperature to 140°C, the change in voltage is larger than when increasing to 180°C. The trend in the measured curves is quite the opposite. Here, the change is much more prominent when increasing the temperature. This behaviour causes the model to under predict the voltage at both 140°C and 180°C.

The effect of temperature on the simulated impedances spectra is also not entirely in line with the evidence presented by the data. One effect can be observed in the ohmic contribution. Here, the recorded spectra shown in figure 5.27 have

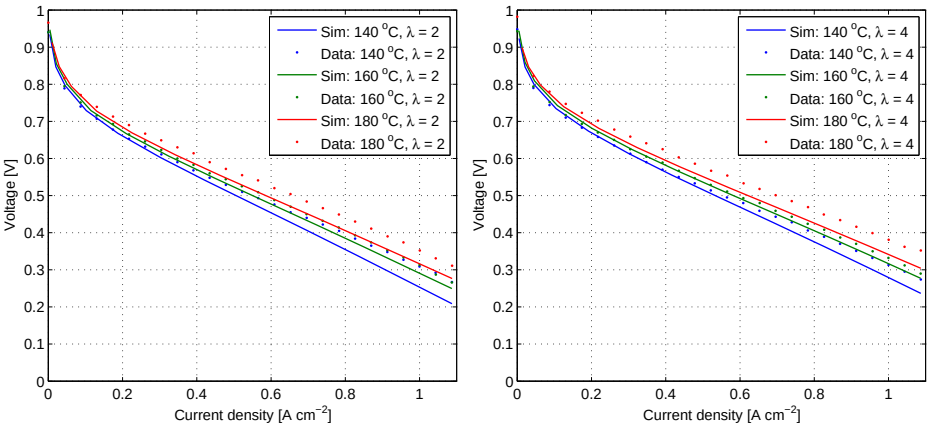

Figure 5.26 – Simulated and recorded polarisation curves illustrating the effect of operating temperature.

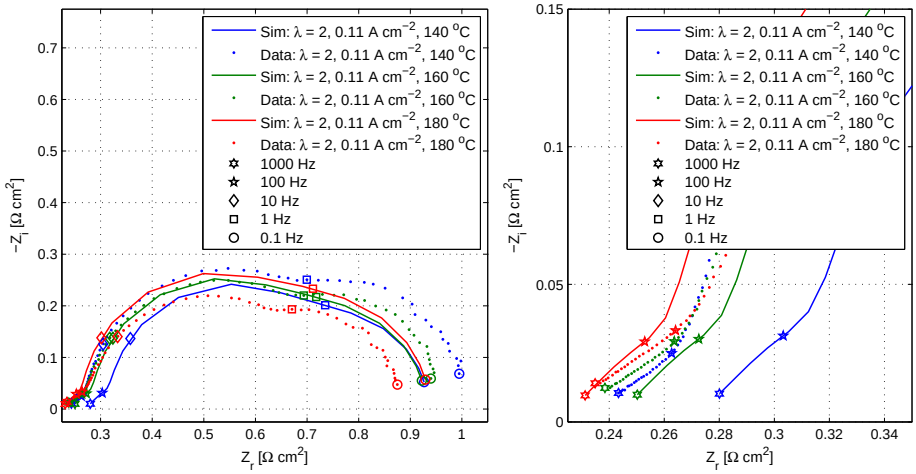

Figure 5.27 – Simulated and recorded impedance spectra illustrating the effect of operating temperature. Parameters from case 7 used.

impedance real part at 1 kHz of around $0.235\,\Omega\,\mathrm{cm}^2$ at 180 °C and $0.25\,\Omega\,\mathrm{cm}^2$ at 140 °C. In the simulated curves, the effect of temperature is much more pronounced. Here the resistance at 180 °C is $0.235\,\Omega\,\mathrm{cm}^2$, while at 140 °C it reaches $0.28\,\Omega\,\mathrm{cm}^2$. This clearly indicates, that the model has a shortcoming, when it comes to estimating the total ohmic resistance. When considering the effects seen, a constant value for the membrane resistance would have reproduced the

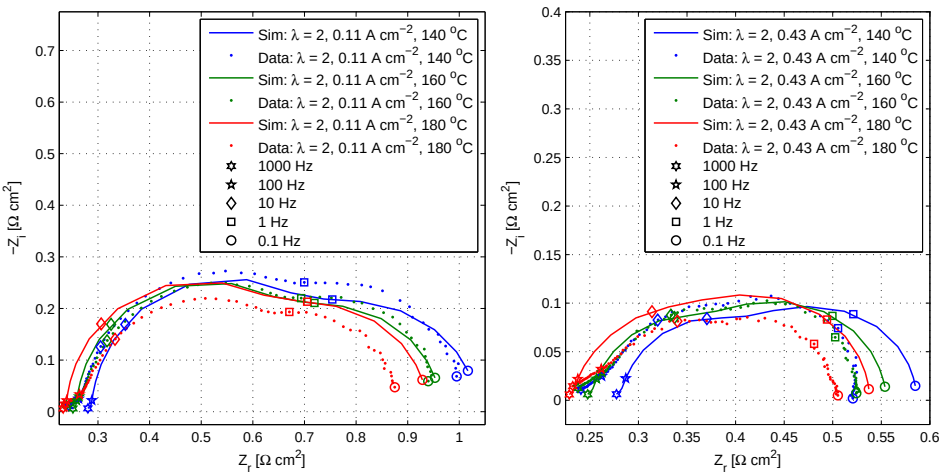

Figure 5.28 – Simulated and recorded impedance spectra illustrating the effect of operating temperature. Parameters from case 2.

high frequency region of the spectra better.

Another issue, which poses a more serious problem for the validity of the model, is the development of the size of the whole impedance spectrum. The recorded spectra shrink as temperature is increased as should be expected. In the simulated spectra, the trend is the opposite, however. In the simulations using the case 7 parameters (figure 5.27) the spectra clearly become larger as the temperature is increased. The trend is less pronounced using case 2 parameters (figure 5.28) and here the simulated spectrum at 140°C, 0.11 A cm^{-2}, and $\lambda = 2$ seems to be slightly larger than the spectra at higher temperature. This trend does not prevail at 0.43 A cm^{-2}, where the temperature dependence is again the opposite of what should be expected.

The reason for this unexpected trend is most likely related to the catalyst layer model. Assuming that the platinum is distributed on the surface of the carbon which is covered with a thin film of PA results in a very limited effect of the diffusion of oxygen in PA. Using the case 7 parameters, the resulting film thickness is around $4 \cdot 10^{-10}$ m, the diffusion coefficient is around 10^{-9} m^2 s^{-1} and the necessary flux through the film is very small. The coincident curves of the concentration at the surface of the acid film and at the Pt surface are plotted in figure 5.29. This basically means that the whole diffusion limitation derives from diffusion in the gas phase. This is probably not a good representation of the actual conditions in the cell.

Since the gas phase diffusion coefficient does not increase as rapidly as the PA phase diffusion coefficient and the solubility of O_2 in PA increases with temperature as well, the absence of PA phase diffusion losses may result in under

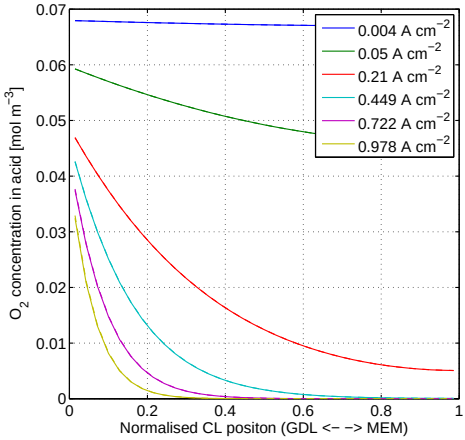

Figure 5.29 – Plot of the oxygen concentration at the PA-gas interface and at the Pt surface. The curves are coincident at each current density. Parameters from case 1. $T = 160°\text{C}$. $\lambda = 2$.

prediction of the temperature dependence of the diffusion losses.

Another issue may be the temperature dependence of the exchange current density relative to the temperature dependence of the exponential term in the Butler-Volmer equation. The decrease of $\frac{\partial i}{\partial \eta}$ with temperature tends to increase the impedance at higher temperatures. The temperature dependence of the exchange current density is not able to make up for this, resulting in increased impedance at higher temperatures. Assuming the exponential term to be independent of temperature or for α to increase with temperature as has been observed in the literature [114] could be options for improving the agreement with the data.

5.6.1 Fixing the membrane conductivity

The most straightforward problem to address is the exaggerated effect of temperature on the ohmic resistance. This is most easily done by fixing the temperature used when calculating the membrane conductivity. Since the model is fitted at 160 °C, this temperature is used. The resulting simulated curves are shown in figures 5.30 and 5.31. The polarisation curves are now very close together, indicating that the primary source of the performance difference in the simulations is the conductivity model. The polarisation curves at 140 °C now agree much better with the data, but the agreement at 180 °C is worse. This means that temperature dependence of the exchange current density or another phenomenon related to activity is under predicted. When considering the impedance spectra, the difference in ohmic resistance is now too small compared to the data, but

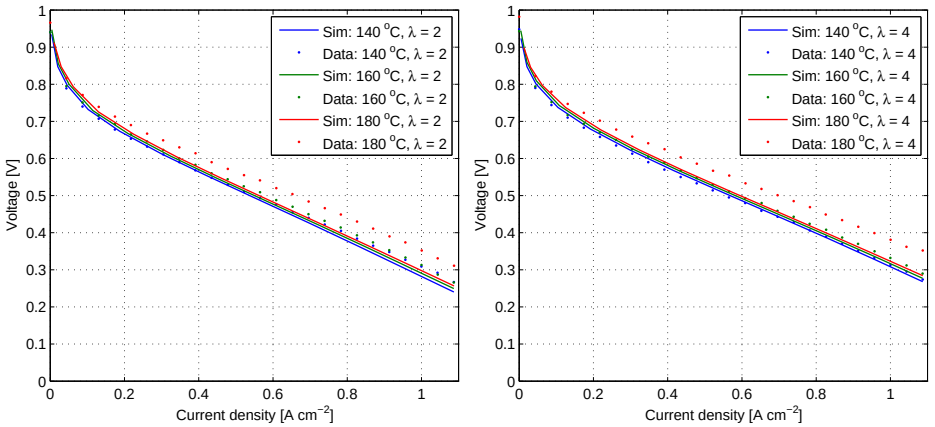

Figure 5.30 – Simulated and recorded polarisation curves illustrating the effect of operating temperature.

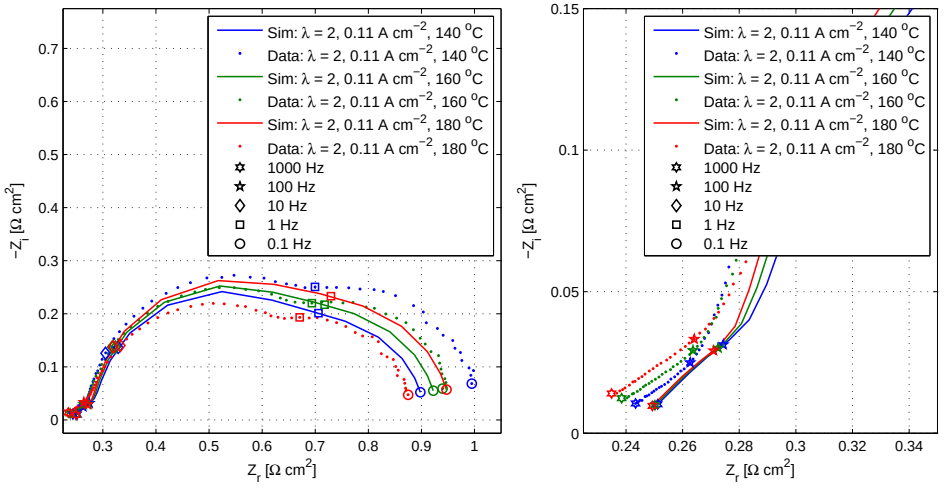

Figure 5.31 – Simulated and recorded impedance spectra illustrating the effect of operating temperature.

the agreement is much better than when not keeping the membrane resistance constant. The actual phenomena determining the the total ohmic resistance are most likely more involved than initially assumed.

A possible explanation for the observed discrepancy could be an interplay between the contact resistance, the conductivity of the electronically conductive components and the membrane conductivity. While the model assumes that only

the PA and the membrane resistance changes with temperature and humidity, the conductivity of the electronically conductive components goes down with temperature. This effect may be what causes the high frequency part to become more pronounced at high temperatures in the recorded spectra. Another parameter, which was not considered, is the volume expansion of the membrane. A wet PA doped PBI membrane is around twice as thick as a dry one [128]. At low temperature, where the acid can contain more water at the same absolute humidity [95], the membrane should swell compared to the case at high temperature. This may result in higher compression of the other cell components, reducing the contact resistance. A model taking these effects into account may be able to reproduce the temperature dependence of the total resistance more faithfully. This complex interaction may, however, be too hard to model, and so reducing the model complexity and just fitting a constant ohmic resistance, or making an empirical regression form the impedance spectra across the operating range may be a viable solution.

5.6.2 Balancing gas phase and acid phase diffusion resistance

The switch from diffusion losses in the gas phase to the acid phase could be achieved in different ways. The simplest way to increase the diffusion losses in the acid would be to change the way the diffusion coefficient and the film thickness is calculated. If the film is assumed to consist of the PBI binder as well as the PA, the result would be a thicker film. Since diffusion would now take place through a mix of PA and PBI, it would be appropriate to modify the oxygen diffusion coefficient using the Bruggeman correction. Both the modification would result in higher diffusion losses in the film. It might be necessary to make other oxygen transport related changes to the model, since the ratio of the product of the oxygen flux and the film thickness to the diffusion coefficient will have to be increased several orders of magnitude for the acid phase diffusion to become significant.

Another way would be to introduce an agglomerate model. This approach has been used in several HTPEM models in the literature [50, 53, 60]. The agglomerates would be modelled as a macro-homogeneous mix of the CL constituents. The diffusion path would be more tortuous than when considering a film of PA and PBI, increasing the diffusion losses. Assuming that the raw ESA of the catalyst used in the fuel cell is available, the fitting of the catalyst ESA could be eliminated, since the effective catalyst surface area available for the reactions would be determined by the agglomerate diffusion length and diffusion resistance inside the agglomerates. Also, the surface area inside the CL will be inversely proportional to the volume of the individual agglomerates at a given volume fraction of the solid phase. This means that in this case, the fitting the agglomerate radius removes the need for fitting the carbon surface area. In this way the Knudsen diffusion losses and the diffusion losses in the PA could be linked.

If it would be necessary to further reduce the gas phase diffusion resistance, the current tortuosity correction model for the GDL could be replaced by the Bruggeman correction. This would decrease the diffusion resistance in the GDL, allowing a wider window for adjusting the diffusion in the CL.

Whether these changes are able change the wrong temperature dependence of the impedance spectra will have to be investigated in future work.

5.7 Sub-conclusions

The investigations carried out in this chapter has demonstrated that making a mechanistic fuel cell model reproduce impedance spectra and polarisation curves simultaneously is far from a trivial task. Parametric fitting of the model has been performed for ten different fitting cases with small changes in the fixed parameters between each. Some cases produce significantly better fits than others, but some of the best fits have other issues with unreasonable values of some of the fitting parameters or polarisation curves shaped differently from those of the data. The fit, which seems most credible is the one produced with the 1-step reaction mechanism, first order reaction with respect to oxygen and a transfer coefficient of 0.75.

Considering the high catalyst loading and the rather high specific ESA in the range of $40\,\mathrm{m^2\,g^{-1}}$, the effectiveness of the catalyst is low. This seems to be the result of large diffusion losses. If this result is to be trusted, the performance of the Dapozol® 77 MEA might be improved significantly, if it was possible to increase the porosity of the catalyst layer. Alternatively, the catalyst loading could be decreased. This would save on manufacturing costs, but given the low reaction depth at high current density, it would not compromise the performance significantly.

The predictive capabilities of the model outside the operating range for which the parameters are fitted are not sufficiently good to validate the model. The dependence of the impedance on the DC current density is reproduced acceptably even though the simulated spectra that have not been fitted directly exhibit poorer agreement with the data. The problems with the model are mainly related to the operating temperature. The temperature dependence of the polarisation curve is different from what is seen in the data. In the data, the voltage is reduced modestly when decreasing the temperature from 160 °C and increased significantly, when increasing the temperature. The simulated curves exhibit a large decrease in voltage when lowering the temperature and a modest increase when increasing the temperature. This dependence derives from an exaggerated temperature effect on the ohmic resistance of the cell, which only varies with membrane conductivity. The temperature effects on the other losses are too small, especially when increasing the temperature. The impedance spectra have two problems with the temperature dependence. One is with the ohmic resistance as mentioned. The other is the tendency of the impedance spectra to shrink when lowering the tem-

perature. This is in direct disagreement with what is exhibited by the data. This behaviour is attributed to the fact that the diffusion losses in the model originate from gas phase diffusion only. A way to remedy this shortcoming of the model could be to change the catalyst model to make acid phase diffusion more of a limiting factor. An agglomerate model would accomplish this by increasing the length and tortuosity of the diffusion path in the acid phase

To sum up, the model is capable of fitting the behaviour of the of the polarisation curves and the impedance spectra at one temperature, giving a seemingly reasonable estimate of the parameters governing the performance. This capability could potentially be applied in analysing cells that have been subjected to degradation testing. By comparing the model fit to a data set recorded at the beginning of the test and one recorded at the end of the test, it would be possible to quantify what kind of degradation the cell has experienced. By making changes in the fixed parameters, the model might also be able suggest a path for improving the MEA performance by altering the catalyst layer composition or similar. The sub-par performance of the model in terms of temperature dependence will, however, have to be improved before such investigations can be performed with sufficient credibility. This will be the subject of future work.

Chapter 6

Conclusions

This chapter summarises the conclusion of the work performed through this Ph.D. project and suggests a path to applying the results in future work.

6.1 Conclusions

The investigations conducted in this work have explored different tracks to improve the understanding of HTPEM fuel cells and their workings using electrochemical impedance spectroscopy. The work can roughly be divided into two parts. The first part is the mainly experimental approach where EIS has been employed together with equivalent circuit models to analyse the effects of anode feed CO content and changes happening in the cell during break-in. The second part of the investigation describes the development of a mechanistic model of the steady state and impedance characteristics of HTPEM fuel cells and the evaluation of the ability of the model to fit and predict experimental polarisation and impedance data.

In the first experimental investigation, the influence of CO content in the fuel stream of an HTPEM fuel cell using a commercial Celtec®-P2100 MEA was investigated using EIS and polarisation curves. The addition of CO was shown to have an effect on the whole impedance spectrum, challenging the common conception of rigid division of the impedance spectrum into distinct contributions. The effects on the spectra were explained by different mechanisms. An increase in the ohmic resistance of the cell was assumed to derive from deactivation of the catalyst closest to the membrane. Lower active area and increased diffusion losses on the anode side due to deactivation of readily available catalyst were assumed to contribute to the capacitive loops in the impedance spectra.

The investigation into the galvanostatic break-in process of Celtec®-P sol-gel and Dapozol® 77 post-doped HTPEM MEAs revealed significant differences in the development of voltage and impedance spectra during the break-in period.

Comparison of the break-in of sol-gel and post-doped MEAs has not previously been published. The changes in the impedance was quantified using an equivalent circuit model. Three different models were tested, and the most simple model was chosen, since it produced the most consistent fitted values. The sol-gel MEAs exhibited the most significant changes in both voltage and impedance. For both types of MEAs, the rate of change was most pronounced in the initial stage of the break-in after which the rates would stabilise. The change rates stabilised within the first few hours for the post-doped MEAs, while the sol-gel took around 30-40 hours. In both cases, the results indicate that break-in times significantly shorter than the 100 hours recommended for Celtec®-P MEAs are feasible.

A common conclusion from the work involving equivalent circuit models relate to the models themselves. Particularly the test of three different models for the break-in study illustrated the ambiguity of equivalent circuit models. This leads to the suggestion of an equivalent circuit model with a minimum of degrees of freedom which should be able to account for all major contributions in an HTPEM fuel cell impedance spectrum.

The mechanistic modelling part of the project has, through a number of byways, resulted in a 1+1D finite volume based model, considering only the cathode side. The emphasis of the model is the interaction between the local phosphoric acid concentration in the catalyst layer and the electrode kinetics and transport phenomena. The dependence of oxygen solubility, diffusivity, and the cathode exchange current density on acid concentration is modelled in more detail than is usually employed in HTPEM models.

The model was fitted to a set of polarisation curves and impedance spectra assuming different combinations of fixed parameters. Different values of the reaction order and the transfer coefficient were tested. Changing the catalyst layer conductivity model was also investigated as well as the influence of the reaction mechanism. The results of fitting the individual cases reveals the complexity of the task of making an advanced fuel cell model fit impedance spectra and polarisation curves simultaneously. It also illustrates the issues with determining criteria for a good fit, since some of the fits that are best in terms of the value of the objective function, has issues with either the behaviour of the simulated curves or with fitting parameters converging to seemingly unreasonable values. The investigation underlines the strength of combining impedance spectra and polarisation curves, since the parameter combination that provides the best fit to the polarisation curves, provides a comparably worse fit to the impedance spectra. This indicates that this parameter combination is not, after all, representative of the actual state of affairs. The fitted model is used to investigate the effects of the flow dynamics of the cathode gas on the impedance spectrum. The low frequency part of the impedance spectrum can be attributed to this phenomenon.

The model is reasonably capable of reproducing the effect of the DC current on the impedance spectra. The temperature dependence is, however, not satisfactorily reproduced by the model. The power of combining the two types of

curves allows easy diagnosis of part of the problem. The temperature dependence of the cell resistances is too great. Another problem is assumed to be the balancing between diffusion losses in the gas phase and the acid phase. These are dominated by gas phase losses due to the choice of catalyst layer model. Alternative catalyst layer models must be investigated to enable the model to reliably extract cell parameters. While the initial aim of the project has thus not been fully achieved, significant insight into the power of this modelling approach has been gained, paving the way for future studies.

6.2 Future work

As is the nature of scientific work, the conclusions drawn from the investigations presented in this thesis have spawned a number of new questions which could be interesting to investigate.

With respect to the experimental work, the indications that shortening break-in times is possible without reducing the life time, should be investigated further. This would require a number of identical MEAs to be broken in for different lengths of time and subsequently subjecting them to a load cycle mimicking realistic operating conditions for an extended period of time. The observed differences in performance before and after break-in, as well as after the load cycling, would serve to identify the minimum allowable break-in time. This could potentially save time and money in the deployment of HTPEM fuel cell systems.

The future work regarding the mechanistic impedance model initially concerns the improvement of the agreement of the model with the temperature dependence of the data. A first step would be to introduce an agglomerate model to get a more realistic division between the diffusion losses in the gas phase and the acid phase. This should increase the temperature dependence of the diffusion losses. Another mechanism, which could be interesting to model, is the temperature dependence of the contact resistances in the cell. Such a model would need to take into account the interplay of thermal expansion of the different cell components and could potentially explain the observed discrepancy between the temperature dependence of the electrolyte conductivity and the actual cell resistance.

Assuming that these improvements to the model are capable of correcting the inadequate performance, the model should be applied to the analysis of experimental data. The investigation regarding the effect of break-in time could possibly benefit from the application of the improved model to analyse the changes happening within the catalyst layer during break-in. If the model should also be applied to analyse the effects of degradation in the individual MEAs, it might be necessary to include an anode model to account for the effects of carbon corrosion at this electrode.

Bibliography

[1] J. S. Wainright, J. T. Wang, D. Weng, R. F. Savinell, and M. Litt. Acid-Doped Polybenzimidazoles: A New Polymer Electrolyte. *Journal of The Electrochemical Society*, 142(7):L121–L123, July 1995. ISSN 00134651. doi: 10.1149/1.2044337.

[2] IPCC. Summary for Policy Makers. In *Climate Change 2014: Climate Change Mitigation. Contribution of Working Group III to the Fifth Assessment Report of the Intergovernmental Panel on Climate Change*, pages 1–33. 2014.

[3] The Danish Government. The Danish Climate Policy Plan Towards a low carbon society. Technical report, The Ministry of Climate, Energy and Building, Copenhagen, 2013.

[4] W. R. Grove. On the Gas Voltaic Battery. Experiments Made with a View of Ascertaining the Rationale of Its Action and Its Application to Eudiometry. *Philosophical Transactions of the Royal Society of London*, 133:91–112, 1843.

[5] E. Chen. History. In G. Hoogers, editor, *Fuel cell technology handbook*, chapter 2, pages 18–57. CRC Press, 2003.

[6] O. Z. Sharaf and M. F. Orhan. An overview of fuel cell technology: Fundamentals and applications. *Renewable and Sustainable Energy Reviews*, 32: 810–853, April 2014. ISSN 13640321. doi: 10.1016/j.rser.2014.01.012.

[7] R. P. O'Hayre, S.-W. Cha, W. G. Colella, and F. B. Prinz. *Fuel Cell Fundamentals*. John Wiley & Sons, Inc., 2nd edition, 2008. ISBN 978-0-470-25843-9.

[8] S. Mekhilef, R. Saidur, and A. Safari. Comparative study of different fuel cell technologies. *Renewable and Sustainable Energy Reviews*, 16(1):981–989, January 2012. ISSN 13640321. doi: 10.1016/j.rser.2011.09.020.

[9] A. L. Dicks. Molten carbonate fuel cells. *Current Opinion in Solid State and Materials Science*, 8(5):379–383, October 2004. ISSN 13590286. doi: 10.1016/j.cossms.2004.12.005.

[10] R. Carapellucci, R. Saia, and L. Giordano. Study of Gas-steam Combined Cycle Power Plants Integrated with MCFC for Carbon Dioxide Capture. *Energy Procedia*, 45:1155–1164, 2014. ISSN 18766102. doi: 10.1016/j.egypro.2014.01.121.

[11] S. Lee, T. Lim, R. Song, D. Shin, and S. Dong. Development of a 700W anode-supported micro-tubular SOFC stack for APU applications. *International Journal of Hydrogen Energy*, 33(9):2330–2336, May 2008. ISSN 03603199. doi: 10.1016/j.ijhydene.2008.02.034.

[12] G. Merle, M. Wessling, and K. Nijmeijer. Anion exchange membranes for alkaline fuel cells: A review. *Journal of Membrane Science*, 377(1-2):1–35, July 2011. ISSN 03767388. doi: 10.1016/j.memsci.2011.04.043.

[13] K. Kasahara, M. Morioka, H. Yoshida, and H. Shingai. PAFC operating performance verified by Japanese gas utilities. *Journal of Power Sources*, 86(1-2):298–301, March 2000. ISSN 03787753. doi: 10.1016/S0378-7753(99)00409-7.

[14] Z. Wan, H. Chang, S. Shu, Y. Wang, and H. Tang. A Review on Cold Start of Proton Exchange Membrane Fuel Cells. *Energies*, 7(5):3179–3203, May 2014. ISSN 1996-1073. doi: 10.3390/en7053179.

[15] S. M. M. Ehteshami and S. H. Chan. A review of electrocatalysts with enhanced CO tolerance and stability for polymer electrolyte membarane fuel cells. *Electrochimica Acta*, 93:334–345, March 2013. ISSN 00134686. doi: 10.1016/j.electacta.2013.01.086.

[16] V. P. McConnell. Fuel cells in forklifts extend commercial reach. *Fuel Cells Bulletin*, 2010(9):12–19, September 2010. ISSN 14642859. doi: 10.1016/S1464-2859(10)70296-0.

[17] K. Fosberg. Fuel cell systems provide backup power in telecom applications. *Fuel Cells Bulletin*, 2010(12):12–14, December 2010. ISSN 14642859. doi: 10.1016/S1464-2859(10)70361-8.

[18] J. B. Hansen, A. S. Petersen, I. Loncarevic, C. Torbensen, P. S. Koustrup, A. Korsgaard, S. Lykkemark, M. Mogensen, A. H. Pedersen, M. W. Hansen, J. Bonde, A. Mortensgaard, J. Lebæk, and H. O. Hansen. GreenSynFuels. Technical Report March, Danish Technological Institute, 2011.

[19] J. Hales, C. Kallesøe, T. Lund-Olesen, A.-C. Johansson, H. Fanøe, Y. Yu, P. Lund, A. Vig, O. Tynelius, and L. Christensen. Micro fuel cells power the

hearing aids of the future. *Fuel Cells Bulletin*, 2012(12):12–16, December 2012. ISSN 14642859. doi: 10.1016/S1464-2859(12)70367-X.

[20] A. Chandan, M. Hattenberger, A. El-kharouf, S. Du, A. Dhir, V. Self, B. G. Pollet, A. Ingram, and W. Bujalski. High temperature (HT) polymer electrolyte membrane fuel cells (PEMFC) - A review. *Journal of Power Sources*, 231:264–278, June 2013. ISSN 03787753. doi: 10.1016/j.jpowsour.2012.11.126.

[21] A. D. Modestov, M. R. Tarasevich, V. Y. Filimonov, and E. S. Davydova. CO tolerance and CO oxidation at Pt and Pt-Ru anode catalysts in fuel cell with polybenzimidazole-H3PO4 membrane. *Electrochimica Acta*, 55(20):6073–6080, August 2010. ISSN 00134686. doi: 10.1016/j.electacta.2010.05.068.

[22] S. K. Das, A. Reis, and K. J. Berry. Experimental evaluation of CO poisoning on the performance of a high temperature proton exchange membrane fuel cell. *Journal of Power Sources*, 193(2):691–698, September 2009. ISSN 03787753. doi: 10.1016/j.jpowsour.2009.04.021.

[23] P. Krishnan, J.-S. Park, and C.-S. Kim. Performance of a poly(2,5-benzimidazole) membrane based high temperature PEM fuel cell in the presence of carbon monoxide. *Journal of Power Sources*, 159(2):817–823, 2006. ISSN 0378-7753. doi: 10.1016/j.jpowsour.2005.11.071.

[24] P. Moçotéguy, B. Ludwig, J. Scholta, Y. Nedellec, D. J. Jones, and J. Rozière. Long-Term Testing in Dynamic Mode of HT-PEMFC H 3 PO 4 /PBI Celtec-P Based Membrane Electrode Assemblies for Micro-CHP Applications. *Fuel Cells*, 10(2):299–311, April 2010. ISSN 16156846. doi: 10.1002/fuce.200900153.

[25] Y.-L. Ma, J. S. Wainright, M. H. Litt, and R. F. Savinell. Conductivity of PBI Membranes for High-Temperature Polymer Electrolyte Fuel Cells. *Journal of The Electrochemical Society*, 151(1):A8–A16, 2004. doi: 10.1149/1.1630037.

[26] S. J. Andreasen, L. Ashworth, S. Sahlin, H.-C. Becker Jensen, and S. K. Kær. Test of hybrid power system for electrical vehicles using a lithium-ion battery pack and a reformed methanol fuel cell range extender. *International Journal of Hydrogen Energy*, 39(4):1856–1863, January 2014. ISSN 03603199. doi: 10.1016/j.ijhydene.2013.11.068.

[27] G. Avgouropoulos, J. Papavasiliou, M. K. Daletou, J. K. Kallitsis, T. Ioannides, and S. Neophytides. Reforming methanol to electricity in a high temperature PEM fuel cell. *Applied Catalysis B: Environmental*, 90(3-4): 628–632, August 2009. ISSN 09263373. doi: 10.1016/j.apcatb.2009.04.025.

[28] G. Avgouropoulos and S. G. Neophytides. Performance of internal reforming methanol fuel cell under various methanol/water concentrations. *Journal of Applied Electrochemistry*, 42(9):719–726, July 2012. ISSN 0021-891X. doi: 10.1007/s10800-012-0453-x.

[29] G. Avgouropoulos, A. Paxinou, and S. Neophytides. In situ hydrogen utilization in an internal reforming methanol fuel cell. *International Journal of Hydrogen Energy*, 39(31):18103–18108, October 2014. ISSN 03603199. doi: 10.1016/j.ijhydene.2014.03.101.

[30] S. J. Andreasen, S. K. Kær, and S. Sahlin. Control and experimental characterization of a methanol reformer for a 350 W high temperature polymer electrolyte membrane fuel cell system. *International Journal of Hydrogen Energy*, 38(3):1676–1684, February 2013. ISSN 03603199. doi: 10.1016/j.ijhydene.2012.09.032.

[31] K. K. Justesen, S. J. Andreasen, H. R. Shaker, M. P. Ehmsen, and J. Andersen. Gas composition modeling in a reformed Methanol Fuel Cell system using adaptive Neuro-Fuzzy Inference Systems. *International Journal of Hydrogen Energy*, 38(25):10577–10584, August 2013. ISSN 03603199. doi: 10.1016/j.ijhydene.2013.06.013.

[32] S. Araya, S. Andreasen, and S. Kær. Experimental Characterization of the Poisoning Effects of Methanol-Based Reformate Impurities on a PBI-Based High Temperature PEM Fuel Cell. *Energies*, 5(12):4251–4267, October 2012. ISSN 1996-1073. doi: 10.3390/en5114251.

[33] S. Simon Araya, S. J. Andreasen, H. V. Nielsen, and S. K. Kær. Investigating the effects of methanol-water vapor mixture on a PBI-based high temperature PEM fuel cell. *International Journal of Hydrogen Energy*, 37(23):18231–18242, December 2012. ISSN 03603199. doi: 10.1016/j.ijhydene.2012.09.009.

[34] F. Weng, C.-K. Cheng, and K.-C. Chen. Hydrogen production of two-stage temperature steam reformer integrated with PBI membrane fuel cells to optimize thermal management. *International Journal of Hydrogen Energy*, 38(14):6059–6064, May 2013. ISSN 03603199. doi: 10.1016/j.ijhydene.2013.01.090.

[35] C. Pan, R. He, Q. Li, J. O. Jensen, N. J. Bjerrum, H. A. Hjulmand, and A. B. Jensen. Integration of high temperature PEM fuel cells with a methanol reformer. *Journal of Power Sources*, 145(2):392–398, August 2005. ISSN 0378-7753. doi: 10.1016/j.jpowsour.2005.02.056.

[36] Serenergy web site. URL `http://serenergy.com/`. Accessed 2014-10-10.

[37] S. Galbiati, A. Baricci, A. Casalegno, and R. Marchesi. Degradation in phosphoric acid doped polymer fuel cells: A 6000Â h parametric investigation. *International Journal of Hydrogen Energy*, 38(15):6469–6480, 2013.

[38] T. J. Schmidt and J. Baurmeister. Durability and Reliability in High-Temperature Reformed Hydrogen PEFCs. *ECS Transactions*, 3(1):861–869, October 2006. ISSN 1938-5862. doi: 10.1149/1.2356204.

[39] T. J. Schmidt and J. Baurmeister. Properties of high-temperature PEFC Celtec-P 1000 MEAs in start/stop operation mode. *Journal of Power Sources*, 176(2):428–434, February 2008. ISSN 03787753. doi: 10.1016/j.jpowsour.2007.08.055.

[40] Y. Oono, A. Sounai, and M. Hori. Long-term cell degradation mechanism in high-temperature proton exchange membrane fuel cells. *Journal of Power Sources*, 210:366–373, July 2012. ISSN 03787753. doi: 10.1016/j.jpowsour.2012.02.098.

[41] P. Moçotéguy, B. Ludwig, J. Scholta, R. Barrera, and S. Ginocchio. Long Term Testing in Continuous Mode of HT-PEMFC Based H3PO4 /PBI Celtec-P MEAs for μ-CHP Applications. *Fuel Cells*, 9(4):325–348, August 2009. ISSN 16156846. doi: 10.1002/fuce.200800134.

[42] P. L. Rasmussen. *Investigation of Lifetime Issues in HTPEM Fuel Cell Based CHP Systems: Stack Level Degradation.* PhD thesis, Aalborg University, 2008.

[43] A. R. Korsgaard, R. Refshauge, M. P. Nielsen, M. Bang, and S. K. Kær. Experimental characterization and modeling of commercial polybenzimidazole-based MEA performance. *Journal of Power Sources*, 162(1):239–245, November 2006. ISSN 03787753. doi: 10.1016/j.jpowsour.2006.06.099.

[44] A. R. Korsgaard, M. P. Nielsen, M. Bang, and S. K. Kær. Modeling of CO influence in PBI electrolyte PEM fuel cells. In *Proceedings of the 4th International ASME Conference on Fuel Cell Science, Engineering and Technology.* ASME Press, 2006.

[45] A. R. Korsgaard, M. P. Nielsen, and S. K. Kær. Part one: A novel model of HTPEM-based micro-combined heat and power fuel cell system. *International Journal of Hydrogen Energy*, 33(7):1909–1920, April 2008. ISSN 03603199. doi: 10.1016/j.ijhydene.2008.01.009.

[46] A. R. Korsgaard, M. P. Nielsen, and S. K. Kær. Part two: Control of a novel HTPEM-based micro combined heat and power fuel cell system. *International Journal of Hydrogen Energy*, 33(7):1921–1931, April 2008. ISSN 0360-3199. doi: 10.1016/j.ijhydene.2008.01.008.

[47] D. Cheddie and N. Munroe. Parametric model of an intermediate temperature PEMFC. *Journal of Power Sources*, 156(2):414–423, June 2006. ISSN 03787753. doi: 10.1016/j.jpowsour.2005.06.010.

[48] K. Scott, S. Pilditch, and M. Mamlouk. Modelling and experimental validation of a high temperature polymer electrolyte fuel cell. *Journal of Applied Electrochemistry*, 37(11):1245–1259, September 2007. ISSN 0021891X. doi: 10.1007/s10800-007-9414-1.

[49] O. Shamardina, A. Chertovich, A. A. Kulikovsky, and A. R. Khokhlov. A simple model of a high temperature PEM fuel cell. *International Journal of Hydrogen Energy*, 35(18):9954–9962, September 2010. ISSN 0360-3199. doi: 10.1016/j.ijhydene.2009.11.012.

[50] T. Sousa, M. Mamlouk, and K. Scott. An isothermal model of a laboratory intermediate temperature fuel cell using PBI doped phosphoric acid membranes. *Chemical Engineering Science*, 65(8):2513–2530, 2010. ISSN 0009-2509. doi: 10.1016/j.ces.2009.12.038.

[51] T. J. Kazdal, S. Lang, F. Kühl, and M. J. Hampe. Modelling of the vapour-liquid equilibrium of water and the in situ concentration of H3PO4 in a high temperature proton exchange membrane fuel cell. *Journal of Power Sources*, 249:446–456, March 2014. ISSN 03787753. doi: 10.1016/j.jpowsour.2013.10.098.

[52] J. Hu, H. Zhang, and L. Gang. Diffusion-convection/electrochemical model studies on polybenzimidazole (PBI) fuel cell based on AC impedance technique. *Energy Conversion and Management*, 49(5):1019–1027, 2008. ISSN 0196-8904. doi: 10.1016/j.enconman.2007.10.002.

[53] T. Sousa, M. Mamlouk, and K. Scott. A dynamic non-isothermal model of a laboratory intermediate temperature fuel cell using PBI doped phosphoric acid membranes. *International Journal of Hydrogen Energy*, 35(8):2513–2530, November 2010. ISSN 0360-3199. doi: 10.1016/j.ijhydene.2010.08.057.

[54] D. F. Cheddie and N. D. H. Munroe. Three dimensional modeling of high temperature PEM fuel cells. *Journal of Power Sources*, 160(1):215–223, 2006. ISSN 0378-7753. doi: 10.1016/j.jpowsour.2006.01.035.

[55] D. F. Cheddie and N. D. H. Munroe. A two-phase model of an intermediate temperature PEM fuel cell. *International Journal of Hydrogen Energy*, 32 (7):832–841, 2007. ISSN 0360-3199. doi: 10.1016/j.ijhydene.2006.10.061.

[56] J. Peng and S. J. Lee. Numerical simulation of proton exchange membrane fuel cells at high operating temperature. *Journal of Power Sources*, 162(2):1182–1191, November 2006. ISSN 0378-7753. doi: 10.1016/j.jpowsour.2006.08.001.

[57] J. Peng, J. Y. Shin, T. W. Song, and E. Ubong. Transient response of high temperature PEM fuel cell. *Journal of Power Sources*, 179(1):220–231, April 2008. ISSN 0378-7753. doi: 10.1016/j.jpowsour.2007.12.042.

[58] K. Jiao and X. Li. A Three-Dimensional Non-isothermal Model of High Temperature Proton Exchange Membrane Fuel Cells with Phosphoric Acid Doped Polybenzimidazole Membranes. *Fuel Cells*, 10(3):351–362, June 2010. ISSN 16156846. doi: 10.1002/fuce.200900059.

[59] K. Jiao, I. E. Alaefour, and X. Li. Three-dimensional non-isothermal modeling of carbon monoxide poisoning in high temperature proton exchange membrane fuel cells with phosphoric acid doped polybenzimidazole membranes. *Fuel*, 90(2):568–582, February 2011. ISSN 00162361. doi: 10.1016/j.fuel.2010.10.018.

[60] C. Siegel, G. Bandlamudi, and A. Heinzel. Systematic characterization of a PBI/H3PO4 sol-gel membrane - Modeling and simulation. *Journal of Power Sources*, 196(5):2735–2749, 2011. ISSN 0378-7753. doi: 10.1016/j.jpowsour.2010.11.028.

[61] P. Chippar and H. Ju. Three-dimensional non-isothermal modeling of a phosphoric acid-doped polybenzimidazole (PBI) membrane fuel cell. *Solid State Ionics*, 225:30–39, October 2012. ISSN 01672738. doi: 10.1016/j.ssi.2012.02.031.

[62] P. Chippar and H. Ju. Numerical modeling and investigation of gas crossover effects in high temperature proton exchange membrane (PEM) fuel cells. *International Journal of Hydrogen Energy*, 38(18):7704–7714, June 2013. ISSN 03603199. doi: 10.1016/j.ijhydene.2012.07.123.

[63] P. Chippar, K. Kang, Y.-D. Lim, W.-G. Kim, and H. Ju. Effects of inlet relative humidity (RH) on the performance of a high temperature-proton exchange membrane fuel cell (HT-PEMFC). *International Journal of Hydrogen Energy*, 39(6):2767–2775, June 2014. ISSN 03603199. doi: 10.1016/j.ijhydene.2013.05.115.

[64] J. Wu, X. Z. Yuan, H. Wang, M. Blanco, J. J. Martin, and J. Zhang. Diagnostic tools in PEM fuel cell research: Part I Electrochemical techniques. *International Journal of Hydrogen Energy*, 33(6):1735–1746, March 2008. ISSN 0360-3199. doi: 10.1016/j.ijhydene.2008.01.013.

[65] J. Wu, X. Z. Yuan, H. Wang, M. Blanco, J. J. Martin, and J. Zhang. Diagnostic tools in PEM fuel cell research: Part II: Physical/chemical methods. *International Journal of Hydrogen Energy*, 33(6):1747–1757, March 2008. ISSN 03603199. doi: 10.1016/j.ijhydene.2008.01.020.

[66] J. Lobato, P. Cañizares, M. Rodrigo, J. Linares, and G. Manjavacas. Synthesis and characterisation of poly[2,2-(m-phenylene)-5,5-bibenzimidazole] as polymer electrolyte membrane for high temperature PEMFCs. *Journal of Membrane Science*, 280(1-2):351–362, September 2006. ISSN 0376-7388. doi: 10.1016/j.memsci.2006.01.049.

[67] J. L. Jespersen, E. Schaltz, and S. K. Kær. Electrochemical characterization of a polybenzimidazole-based high temperature proton exchange membrane unit cell. *Journal of Power Sources*, 191(2):289–296, June 2009. ISSN 03787753. doi: 10.1016/j.jpowsour.2009.02.025.

[68] M. Mamlouk and K. Scott. Analysis of high temperature polymer electrolyte membrane fuel cell electrodes using electrochemical impedance spectroscopy. *Electrochimica Acta*, 56(16):5493–5512, June 2011. ISSN 0013-4686. doi: 10.1016/j.electacta.2011.03.056.

[69] S. J. Andreasen, J. L. Jespersen, E. Schaltz, and S. K. Kær. Characterisation and Modelling of a High Temperature PEM Fuel Cell Stack using Electrochemical Impedance Spectroscopy. *Fuel Cells*, 9(4):463–473, August 2009. ISSN 16156846. doi: 10.1002/fuce.200800137.

[70] J. Hu, H. Zhang, Y. Zhai, G. Liu, and B. Yi. 500 h continuous aging life test on PBI/H3PO4 high-temperature PEMFC. *International Journal of Hydrogen Energy*, 31(13):1855–1862, October 2006. ISSN 0360-3199. doi: 10.1016/j.ijhydene.2006.05.001.

[71] A. D. Modestov, M. R. Tarasevich, V. Filimonov, and N. M. Zagudaeva. Degradation of high temperature MEA with PBI-H3PO4 membrane in a life test. *Electrochimica Acta*, 54(27):7121–7127, November 2009. ISSN 0013-4686. doi: 10.1016/j.electacta.2009.07.031.

[72] S. Galbiati, A. Baricci, A. Casalegno, G. Carcassola, and R. Marchesi. On the activation of polybenzimidazole-based membrane electrode assemblies doped with phosphoric acid. *International Journal of Hydrogen Energy*, 37(19):14475–14481, October 2012. ISSN 03603199. doi: 10.1016/j.ijhydene.2012.07.032.

[73] M. Boaventura and A. Mendes. Activation procedures characterization of MEA based on phosphoric acid doped PBI membranes. *International Journal of Hydrogen Energy*, 35(20):11649–11660, October 2010. ISSN 03603199. doi: 10.1016/j.ijhydene.2010.03.137.

[74] J. Lobato, P. Cañizares, M. A. Rodrigo, and J. J. Linares. PBI-based polymer electrolyte membranes fuel cells: Temperature effects on cell performance and catalyst stability. *Electrochimica acta*, 52(12):3910–3920, March 2007. ISSN 00134686. doi: 10.1016/j.electacta.2006.11.014.

[75] J. Lobato, P. Cañizares, M. A. Rodrigo, J. J. Linares, and F. J. Pinar. Study of the influence of the amount of PBI-H3PO4 in the catalytic layer of a high temperature PEMFC. *International Journal of Hydrogen Energy*, 35(3):1347–1355, February 2010. ISSN 0360-3199. doi: 10.1016/j.ijhydene.2009.11.091.

[76] T. E. Springer, T. A. Zawodzinski, M. S. Wilson, and S. Gottesfeld. Characterization of Polymer Electrolyte Fuel Cells Using AC Impedance Spectroscopy. *Journal of The Electrochemical Society*, 143(2):587–599, 1996. doi: 10.1149/1.1836485.

[77] Y. Bultel, L. Géniès, O. Antoine, P. Ozil, and R. Durand. Modeling impedance diagrams of active layers in gas diffusion electrodes: diffusion, ohmic drop effects and multistep reactions. *Journal of Electroanalytical Chemistry*, 527:143–155, 2002.

[78] A. A. Kulikovsky and M. Eikerling. Analytical solutions for impedance of the cathode catalyst layer in PEM fuel cell: Layer parameters from impedance spectrum without fitting. *Journal of Electroanalytical Chemistry*, 691:13–17, February 2013. ISSN 15726657. doi: 10.1016/j.jelechem.2012.12.002.

[79] G. Maranzana, J. Mainka, O. Lottin, J. Dillet, A. Lamibrac, A. Thomas, and S. Didierjean. A proton exchange membrane fuel cell impedance model taking into account convection along the air channel: On the bias between the low frequency limit of the impedance and the slope of the polarization curve. *Electrochimica Acta*, 83:13–27, 2012.

[80] S. K. Roy, M. E. Orazem, and B. Tribollet. Interpretation of Low-Frequency Inductive Loops in PEM Fuel Cells. *Journal of The Electrochemical Society*, 154(12):B1378–B1388, 2007. doi: 10.1149/1.2789377.

[81] F. Jaouen and G. Lindbergh. Transient Techniques for Investigating Mass-Transport Limitations in Gas Diffusion Electrodes I. Modeling the PEFC Cathode. *Journal of The Electrochemical Society*, 150(12):A1699–A1710, 2003. ISSN 00134651. doi: 10.1149/1.1624294.

[82] F. Jaouen, G. Lindbergh, and K. Wiezell. Transient Techniques for Investigating Mass-Transport Limitations in Gas Diffusion Electrodes II. Experimental Characterization of the PEFC Cathode. *Journal of The Electrochemical Society*, 150:A1711–A1717, 2003. ISSN 00134651. doi: 10.1149/1.1624295.

[83] M. Boaventura, J. M. Sousa, and A. Mendes. A dynamic model for high temperature polymer electrolyte membrane fuel cells. *International Journal of Hydrogen Energy*, 36(16):9842–9854, 2011. ISSN 0360-3199. doi: 10.1016/j.ijhydene.2011.04.218.

[84] Y. Shi, H. Wang, and N. Cai. Direct two-dimensional electrochemical impedance spectra simulation for solid oxide fuel cell. *Journal of Power Sources*, 208:24–34, June 2012. ISSN 03787753. doi: 10.1016/j.jpowsour.2012.02.012.

[85] O. Shamardina, M. Kondratenko, A. Chertovich, and A. Kulikovsky. A simple transient model for a high temperature PEM fuel cell impedance. *International Journal of Hydrogen Energy*, 39(5):2224–2235, February 2014. ISSN 03603199. doi: 10.1016/j.ijhydene.2013.11.058.

[86] X. Yuan, H. Wang, J. C. Sun, and J. Zhang. AC impedance technique in PEM fuel cell diagnosis - A review. *International Journal of Hydrogen Energy*, 32(17):4365–4380, 2007. ISSN 0360-3199. doi: 10.1016/j.ijhydene.2007.05.036.

[87] C.-Y. Chen and W.-H. Lai. Effects of temperature and humidity on the cell performance and resistance of a phosphoric acid doped polybenzimidazole fuel cell. *Journal of Power Sources*, 195(21):7152–7159, November 2010. ISSN 03787753. doi: 10.1016/j.jpowsour.2010.05.057.

[88] I. A. Schneider, S. A. Freunberger, D. Kramer, A. Wokaun, and G. G. Scherer. Oscillations in gas channels Part I. The forgotten player in impedance spectroscopy in PEFCs. *Journal of the Electrochemical Society*, 154(4):B383–B388, 2007. ISSN 00134651. doi: 10.1149/1.2435706.

[89] I. A. Schneider, D. Kramer, A. Wokaun, and G. G. Scherer. Oscillations in gas channels II. Unraveling the characteristics of the low frequency loop in air-fed PEFC impedance spectra. *Journal of The Electrochemical Society*, 154(8):B770, 2007. ISSN 00134651. doi: 10.1149/1.2742291.

[90] J. Mainka, G. Maranzana, J. Dillet, S. Didierjean, and O. Lottin. Effect of Oxygen Depletion Along the Air Channel of a PEMFC on the Warburg Diffusion Impedance. *Journal of The Electrochemical Society*, 157 (11):B1561–B1568, 2010. ISSN 00134651. doi: 10.1149/1.3481560.

[91] S. K. Roy, H. Hagelin-Weaver, and M. E. Orazem. Application of complementary analytical tools to support interpretation of polymer-electrolyte-membrane fuel cell impedance data. *Journal of Power Sources*, 196(8): 3736–3742, 2011.

[92] J. E. B. Randles. Kinetics of rapid electrode reactions. *Discussions of the Faraday Society*, 1:11, January 1947. ISSN 0366-9033. doi: 10.1039/df9470100011.

[93] T. Tingelöf and J. K. Ihonen. A rapid break-in procedure for PBI fuel cells. *International Journal of Hydrogen Energy*, 34(15):6452–6456, August 2009. ISSN 03603199. doi: 10.1016/j.ijhydene.2009.05.003.

[94] K. Kwon, T. Y. Kim, D. Y. Yoo, S.-G. Hong, and J. O. Park. Maximization of high-temperature proton exchange membrane fuel cell performance with the optimum distribution of phosphoric acid. *Journal of Power Sources*, 188(2):463–467, March 2009. ISSN 03787753. doi: 10.1016/j.jpowsour.2008.11.104.

[95] T. Gu, S. Shimpalee, J. Van Zee, C.-Y. Chen, and C.-W. Lin. A study of water adsorption and desorption by a PBI-H3PO4 membrane electrode assembly. *Journal of Power Sources*, 195(24):8194–8197, December 2010. ISSN 03787753. doi: 10.1016/j.jpowsour.2010.06.063.

[96] Freudenberg FCCT SE & CO. KG. FREUDENBERG Gas Diffusion Layers for PEMFC and DMFC, 2013. URL `http://www.freudenbergfcct.com/`.

[97] Y. A. Cengel. *Heat And Mass Transfer - A Practical Approach*. McGraw-Hill, third edition, 2006.

[98] W. M. Haynes, editor. *CRC Handbook of Chemistry and Physics*.

[99] H. K. Versteeg and W. Malalasekera. *An Introduction to Computational Fluid Dynamics: The Finite Volume Method*. Number 978-0-13-127498-3. Prentice Hall, 2nd edition, 2007.

[100] D. MacDonald and J. Boyack. Density, electrical conductivity, and vapor pressure of concentrated phosphoric acid. *Journal of Chemical and Engineering Data*, 14(3):380–384, 1969. ISSN 00219568.

[101] K. Klinedinst, J. A. S. Bett, J. Macdonald, and P. Stonehart. Oxygen solubility and diffusivity in hot concentrated H3PO4. *Electroanalytical Chemistry and Interfacial Electrochemistry*, 57(3):281–289, 1974. ISSN 03681874.

[102] K. E. Gubbins and R. D. Walker. Solubility and diffusivity of hydrocarbons and oxygen in fuel cell electrolytes. Technical Report X, University of Florida, Gainesville, Florida, 1965.

[103] A. Essalik, O. Savagodo, and F. Ajersch. Chemical and Electrochemical Parameters for Oxygen Reduction on Pt-H2WO4/Carbon Electrodes in 99% H3PO4. *Journal of The Electrochemical Society*, 142(5):1368, 1995. ISSN 00134651. doi: 10.1149/1.2048584.

[104] B. R. Scharifker, P. Zelenay, and J. O. M. Bockris. The Kinetics of Oxygen Reduction in Molten Phosphoric Acid at High Temperatures. *Journal of The Electrochemical Society*, 134(11):2714–2725, November 1987. ISSN 00134651. doi: 10.1149/1.2100276.

[105] A. L. Magalhães, P. F. Lito, F. A. Da Silva, and C. M. Silva. Simple and accurate correlations for diffusion coefficients of solutes in liquids and supercritical fluids over wide ranges of temperature and density. *The Journal of Supercritical Fluids*, 76:94–114, 2013.

[106] D.-T. Chin and H. Chang. On the conductivity of phosphoric acid electrolyte. *Journal of applied electrochemistry*, 19:95–99, 1989.

[107] D. Tromans. Temperature and pressure dependent solubility of oxygen in water: a thermodynamic analysis. *Hydrometallurgy*, 48(3):327–342, 1998.

[108] O. Antoine, Y. Bultel, and R. Durand. Oxygen reduction reaction kinetics and mechanism on platinum nanoparticles inside Nafion. *Journal of Electroanalytical Chemistry*, 499(1):85–94, February 2001. ISSN 15726657. doi: 10.1016/S0022-0728(00)00492-7.

[109] A. Damjanovic and V. Brusic. Electrode kinetics of oxygen reduction on oxide-free platinum electrodes. *Electrochimica Acta*, 12(August):615–628, 1967.

[110] A. McClellan and H. Harnsberger. Cross-sectional areas of molecules adsorbed on solid surfaces. *Journal of Colloid and Interface Science*, 23(4): 577–599, April 1967. ISSN 00219797. doi: 10.1016/0021-9797(67)90204-4.

[111] H. R. Kunz and G. A. Gruver. The Catalytic Activity of Platinum Supported on Carbon for Electrochemical Oxygen Reduction in Phosphoric Acid. *Journal of The Electrochemical Society*, 122(10):1279–1287, 1975. doi: 10.1149/1.2134000.

[112] H. R. Kunz and G. A. Gruver. The effect of electrolyte concentration on the catalytic activity of platinum for electrochemical oxygen reduction in phosphoric acid. *Electrochimica Acta*, 23(3):219–222, 1978. ISSN 0013-4686. doi: 10.1016/0013-4686(78)85049-X.

[113] Z. Liu, J. S. Wainright, M. H. Litt, and R. F. Savinell. Study of the oxygen reduction reaction (ORR) at Pt interfaced with phosphoric acid doped polybenzimidazole at elevated temperature and low relative humidity. *Electrochimica Acta*, 51(19):3914–3923, 2006. ISSN 0013-4686. doi: 10.1016/j.electacta.2005.11.019.

[114] A. Appleby. Evolution and reduction of oxygen on oxidized platinum in 85% orthophosphoric acid. *Journal of Electroanalytical Chemistry and Interfacial Electrochemistry*, 24(1):97–117, January 1970. ISSN 00220728. doi: 10.1016/S0022-0728(70)80011-0.

[115] M. Mamlouk and K. Scott. A study of oxygen reduction on carbon-supported platinum fuel cell electrocatalysts in polybenzimidazole/phosphoric acid. *Proceedings of the Institution of Mechanical Engineers, Part A: Journal of Power and Energy*, 225(2):161–174, March 2011. ISSN 0957-6509. doi: 10.1177/0957650910397103.

[116] M. Mamlouk. *Investigation of High Temperature Polymer Electrolyte Membrane Fuel Cells*. PhD thesis, University of Newcastle upon Tyne, 2008.

[117] Y. Zhai, H. Zhang, D. Xing, and Z.-G. Shao. The stability of Pt/C catalyst in H3PO4/PBI PEMFC during high temperature life test. *Journal of Power Sources*, 164(1):126–133, January 2007. ISSN 0378-7753. doi: 10.1016/j.jpowsour.2006.09.069.

[118] K. Kwon, J. O. Park, D. Y. Yoo, and J. S. Yi. Phosphoric acid distribution in the membrane electrode assembly of high temperature proton exchange membrane fuel cells. *Electrochimica Acta*, 54(26):6570–6575, November 2009. ISSN 00134686. doi: 10.1016/j.electacta.2009.06.031.

[119] J. T. Glass, J. George L. Cahen, and G. E. Stoner. The Effect of Phosphoric Acid Concentration on Electrocatalysis. *Journal of The Electrochemical Society*, 136(3):656–660, 1989. doi: 10.1149/1.2096705.

[120] Q. Li, R. He, J. O. Jensen, and N. J. Bjerrum. PBI-Based Polymer Membranes for High Temperature Fuel Cells - Preparation, Characterization and Fuel Cell Demonstration. *Fuel Cells*, 4(3):147–159, August 2004. ISSN 1615-6854. doi: 10.1002/fuce.200400020.

[121] Q. Li, J. O. Jensen, R. F. Savinell, and N. J. Bjerrum. High temperature proton exchange membranes based on polybenzimidazoles for fuel cells. *Progress in Polymer Science*, 34(5):449–477, May 2009. ISSN 0079-6700. doi: 10.1016/j.progpolymsci.2008.12.003.

[122] Y. Ma. *The Fundamental Studies of Polybenzimidazole/Phosphoric Acid Polymer Electrolyte For Fuel Cells*. PhD thesis, Case Western Reserve University, 2004.

[123] N. Zamel, X. Li, and J. Shen. Numerical estimation of the effective electrical conductivity in carbon paper diffusion media. *Applied Energy*, 93:39–44, May 2012. ISSN 03062619. doi: 10.1016/j.apenergy.2011.08.037.

[124] M. Bang. *Modeling of Diffusive Convective and Electrochemical Processes in PEM fuel cells*. PhD thesis, Aalborg University, 2004.

[125] R. B. Bird, W. E. Steward, and E. N. Lightfoot. *Transport Phenomena*. Number 978-0-470-11539-8. John Wiley & Sons, Inc., revised 2n edition, 2007.

[126] N. Zamel, X. Li, and J. Shen. Correlation for the effective gas diffusion coefficient in carbon paper diffusion media. *Energy and Fuels*, 23(12):6070–6078, 2009.

[127] ISO. Paper and Board - Determination of air permeance (medium range) - Part 5: Gurley method, 2013.

[128] H.-S. Lee, A. Roy, O. Lane, and J. E. McGrath. Synthesis and characterization of poly(arylene ether sulfone)-b-polybenzimidazole copolymers for high temperature low humidity proton exchange membrane fuel cells. *Polymer*, 49(25):5387–5396, November 2008. ISSN 00323861. doi: 10.1016/j.polymer.2008.09.019.

Appendix A

Paper 1

Andreasen SJ, Vang JR, Kær SK. High temperature PEM fuel cell performance characterisation with CO and CO2 using electrochemical impedance spectroscopy. Int J Hydrogen Energy. Elsevier Ltd; 2011;36(16):9815–30.

This paper has been removed from the publicly available version due to possible copyright issues.

Appendix B

Paper 2

Vang JR, Andreasen SJ, Kær SK. A Transient Fuel Cell Model to Simulate HT-PEM Fuel Cell Impedance Spectra. J Fuel Cell Sci Technol. 2012;9(2):021005–1 – 021005–9.

This paper has been removed from the publicly available version due to possible copyright issues.

Appendix C

Paper 3

Vang JR, Andreasen SK, Simon Araya S, Kær SK. Comparative study of the break in process of post doped and sol-gel high temperature proton exchange membrane fuel cells. Int J Hydrogen Energy. Elsevier Ltd; 2014.

This paper has been removed from the publicly available version due to possible copyright issues.

Appendix D

Poster 1

Vang JR, Mamlouk M, Scott K, Kær SK. Determining HTPEM electrode parameters using a mechanistic impedance model. CARISMA 2012, 2012.

AALBORG UNIVERSITY

CARISMA 2012

Determining HTPEM electrode parameters using a mechanistic impedance model

J.R. Vang*†, M. Mamlouk‡, K. Scott‡ and S. K. Kær†

†Department of Energy Technology, Aalborg University, Pontoppidanstræde 101, 9220 Aalborg East, Denmark

‡School of Chemical Engineering and Advanced Materials, Merz Court, Newcastle University, Newcastle upon Tyne, NE1 7RU, United Kingdom

Introduction

The purpose of this work is to enable extraction of unknown MEA parameters from EIS and polarisation curve data. This is attempted by fitting a model to polarisation curve and impedance data simultaneously. The aim is to reduce the risk of obtaining a good fit with non-realistic parameters.

Model

The fuel cell model is implemented using a 2D finite volume approach, taking into account variations across the membrane and along the channel. The model solves a system of 1542 nonlinear equations. The model can be solved in steady state to generate polarisation curves and in dynamic mode to generate impedance spectra. The model is written using Matlab®. Table 1 lists the equations taken into account by the model and the subdomains in which they are solved.

Experimental

The MEA was prepared and tested at the School of Chemical Engineering and Advanced Materials, Newcastle University. The membrane was PBI doped with 5.6 H_3PO_4 PRU. The catalyst layers were made with Pt/C catalyst mixed with PTFE and doped with H_3PO_4. The anode used 20% Pt/C catalyst and a loading of 0.2 mg Pt/cm^2. The cathode used 40% Pt/C catalyst with a loading of 0.4 mg Pt/cm^2. The cell active area was 9 cm^2. Reactant flow rates were 0.45 L/min for air and 0.2 L/min fro H_2. Cell temperature was 150°C

Results

The model is fitted to a data set consisting of one polarisation curve and three impedance spectra. Plots of the fitted curves and the data can be seen on the right. Tables 2 and 3 give the fitted parameter values and the achieved fit quality.

Discussion

The fit to the polarisation curve is quite good in most of the points. At low current density performance is overestimated. This is presumably because the model does not account for H_2 cross-over. At high current density the mass transport losses seem overestimated. This suggests that the acid film thickness is too large.

The impedance spectra fits have a number of problems. While the polarisation curve fit is good around 0.32 A/cm^2, the impedance fit is quite poor at this point. This indicates that there are important phenomena influencing the impedance that the model does not account for. One possible explanation could be that the assumption of single step electrode kinetics is not sufficient to account for the dynamic response of the fuel cell. Introducing a multi step reaction mechanism might increase the impedance in the low frequency region, where the fit is poorest.

At high frequency the shapes of the simulated spectra deviate significantly from the data. Since the shape at high frequency is influence by the CL conductivity, the fitted value of the CL conductivity may be too high.

In all cases the high frequency intercept occurs at a higher value of the impedance real part in the simulation than in the data. This indicates that the ohmic losses are exaggerated. This is more pronounced at higher current density.

The model assumes constant CL and membrane conductivity. Calculating the conductivity as a function of water content may improve the correlation at high current density. This may also give a more realistic value of the catalyst layer conductivity.

Equations solved	Model subdomains								
	Anode				Membrane	Cathode			
	Channel	GDL	MPL	CL		CL	MPL	GDL	Channel
Continuity	x	x	x	x		x	x	x	x
Momentum	x	x	x	x		x	x	x	x
O2 transport						x	x	x	x
H2O transport	x	x	x	x	x	x	x	x	x
Reaction kinetics				x		x			
Reactant diffusion in electrolyte film				x		x			
Ionic potential				x	x	x			

Table 1: Model equations and subdomains

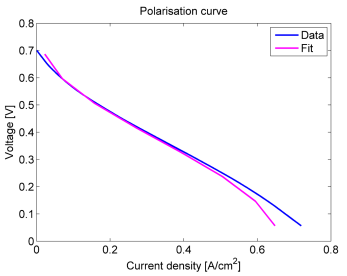

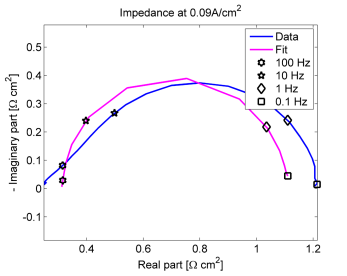

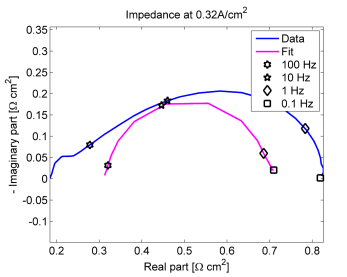

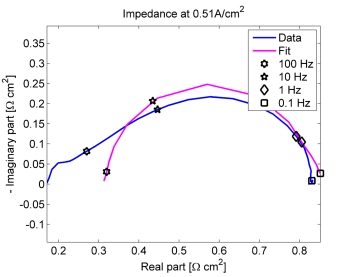

Fitted parameters					
Anode catalyst area	49.6 m^2/m^2	Membrane Conductivity	1.31 S/m	GDL porosity	0.847
Cathode catalyst area	223 m^2/m^2	CL conductivity	9.48 S/m	Cathode charge transfer coefficient	0.627
Anode Capacitance	9.80e5 F/m^3	CL porosity	0.353	CL acid film Thickness	887 nm
Cathode Capacitance	4.40e6 F/m^3	MPL porosity	0.677	Membrane water diffusion coefficient	1.81e-10 m/s^2

Table 2: Fitted parameter values

Fit quality (Normalised RMS deviation):	
Total	18.8 %
Polarisation curve	4.12 %
Mean EIS	18.3 %
EIS at 0.09 A/cm^2	12.5 %
EIS at 0.32 A/cm^2	23.9 %
EIS at 0.51 A/cm^2	16.7%

Table 3: Fit quality

Conclusions

- A 2D finite volume based HTPEM fuel cell model capable of simulating impedance spectra and polarisation curves has been developed.
- The model was fitted to one polarisation curve and three impedance spectra simultaneously.
- An acceptable fit to the polarisation curve has been achieved but a good fit to the impedance spectra could not be achieved simultaneously.
- The main reason for the poor fit is assumed to be the assumption of single step reaction kinetics.
- Future work includes the introduction of a multi step electrode model and calculation of conductivity based on electrolyte water content.

*jrv@et.aau.dk